

AD-A021 631

LASER RADAR SIGNATURES OF RV MODELS OF INTEREST IN
BALLISTIC MISSILE DEFENSE

James H. Michels, et al

Rome Air Development Center

Prepared for:

Army Advanced Ballistic Missile Defense Agency

February 1976

DISTRIBUTED BY:

NTIS

National Technical Information Service
U. S. DEPARTMENT OF COMMERCE

072123

WADC-TR-75-319
In-house Report
February 1976



DA021631

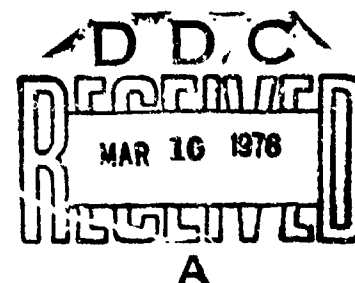
**LASER RADAR SIGNATURES OF RV MODELS OF INTEREST
IN BALLISTIC MISSILE DEFENSE**

James H. Michels
Eugene E. Bromley
Fred J. Demme

Approved for Public Release.
Distribution Unlimited.

**Rome Air Development Center
Air Force Systems Command
Griffiss Air Force Base, New York 13441**

Reproduced by
**NATIONAL TECHNICAL
INFORMATION SERVICE**
U.S. Department of Commerce
Springfield, VA. 22151



PREFACE

This effort was accomplished under Job Order Number R1790001 as an RADC in-house study and investigation funded by both the Air Force and the Army Advanced Ballistic Missile Defense Agency.

The authors acknowledge helpful discussions with Mr. Robert F. Ogradnik. They also wish to acknowledge the technical assistance of Messrs John S. Wilkinson and Richard J. Wood.

The pattern measurement charts which begin on page 46 are of the best quality available. Their intrinsic value makes their inclusion essential.

This report has been reviewed by the RADC Information Office and is releasable to the National Technical Information Service (NTIS). At NTIS it will be releasable to the general public including foreign nations.

This report has been reviewed and is approved for publication.

APPROVED:

Bobbie J. Landers

BOBBIE J. LANDERS, Lt Col, USAF
Chief, Techniques Branch
Surveillance Division

APPROVED:

Moses A. Diab

MOSES A. DIAB
Chief, Space Surveillance & Instrumentation Branch/OC

FOR THE COMMANDER:

John P. Hiss

JOHN P. HISS
Acting Chief
Plans Office

ADMISSION NO.	
WTE	WFO Section <input checked="" type="checkbox"/>
DOS	Dof Section <input type="checkbox"/>
UNANNOUNCED	
JUSTIFICATION	
BY	
DISTRIBUTION/AVAILABILITY CODES	
Dist.	AVAIL. AND/OR SPECIAL

UNCLASSIFIED

SECURITY CLASSIFICATION OF THIS PAGE (When Data Entered)

REPORT DOCUMENTATION PAGE		READ INSTRUCTIONS BEFORE COMPLETING FORM
1. REPORT NUMBER RADC-TR-75-319	2. GOVT ACCESSION NO.	3. RECIPIENT'S CATALOG NUMBER
4. TITLE (and Subtitle) LASER RADAR SIGNATURES OF RV MODELS OF INTEREST IN BALLISTIC MISSILE DEFENSE		5. TYPE OF REPORT & PERIOD COVERED In-house Technical Report - Phase
7. AUTHOR(s) James H. Michels Eugene E. Bromley Fred J. Demma		6. PERFORMING ORG. REPORT NUMBER N/A
8. PERFORMING ORGANIZATION NAME AND ADDRESS Rome Air Development Center (OCTM) Griffiss Air Force Base, NY 13441		6. CONTRACT OR GRANT NUMBER(s) N/A
9. CONTROLLING OFFICE NAME AND ADDRESS N/A		10. PROGRAM ELEMENT, PROJECT, TASK AREA & WORK UNIT NUMBERS PEC: NA JON: R1790001
11. MONITORING AGENCY NAME & ADDRESS (if different from Controlling Office) N/A		12. REPORT DATE February 1976
		13. NUMBER OF PAGES 117
		14. SECURITY CLASS. (of this report) UNCLASSIFIED
		15a. DECLASSIFICATION/DOWNGRADING SCHEDULE N/A
16. DISTRIBUTION STATEMENT (of this Report) Approved for Public Release. Distribution Unlimited.		
17. DISTRIBUTION STATEMENT (of the abstract entered in Block 20, if different from Report) Same		
18. SUPPLEMENTARY NOTES James H. Michels RADC/OCTM AC 315 330-4306		
19. KEY WORDS (Continue on reverse side if necessary and identify by block number) Laser Backscatter Reentry Vehicle Ballistic Missile Defense		
20. ABSTRACT (Continue on reverse side if necessary and identify by block number) A series of measurements were conducted on laser backscatter characteristics from modeled RV and decoy targets of interest to Ballistic Missile Defense (BMD). Bidirectional reflectance measurements were made on the various surface materials. The experimental results were compared with an in-house analytical model (BKSCAT) which predicts backscatter levels based upon flat plate bidirectional reflectance measurements. The agreement between the experimental and analytical results ranges from excellent to poor. Good agreement was obtained for targets		

DD FORM 1 JAN 73 1473 EDITION OF 1 NOV 65 IS OBSOLETE

UNCLASSIFIED

SECURITY CLASSIFICATION OF THIS PAGE (When Data Entered)

UNCLASSIFIED

SECURITY CLASSIFICATION OF THIS PAGE(When Data Entered)

20.

from which representative flat plate reflectance data can be obtained.

UNCLASSIFIED

SECURITY CLASSIFICATION OF THIS PAGE(When Data Entered)

TABLE OF CONTENTS

	<u>PAGE</u>
PREFACE	1
TABLE OF CONTENTS	11
LIST OF TABLES	111
LIST OF FIGURES	1v
I. INTRODUCTION	1
II. DESCRIPTION OF MODELS	2
III. SPECKLE ANALYSIS	4
IV. EXPERIMENTAL ARRANGEMENT	7
V. EXPERIMENTAL PROCEDURE	9
VI. EXPERIMENTAL CALIBRATION	10
VII. EXPERIMENTAL RESULTS	11
VIII. ANALYTICAL BACKSCATTER ESTIMATES	23
A. INTRODUCTION	23
B. TARGET BACKSCATTER CALCULATIONS	24
C. FLAT PLATE REFLECTION DISTRIBUTION FUNCTION	25
D. ANALYTICAL COMPARISON WITH EXPERIMENTAL DATA	26
IX. CONCLUSIONS	29
REFERENCES	32

LIST OF TABLES

<u>TABLE NR.</u>		<u>PAGE</u>
1	LASER RADAR CROSS SECTION CORRECTION FACTORS FOR UNIFORM ILLUMINATION	33
2	REFLECTION DISTRIBUTION FUNCTIONS	34

LIST OF FIGURES

<u>FIGURE</u>		<u>PAGE</u>
II-1	DRAWINGS OF MICON MODELS	40
II-2	DRAWINGS OF ADDITIONAL MODELS	41
IV-1	TARGET BACKSCATTER MEASUREMENT APPARATUS	42
IV-2	BEAM PROFILE MEASUREMENT APPARATUS	43
IV-3	FLAT PLATE BACKSCATTER ARRANGEMENT	44
VI-1	INCIDENT BEAM PROFILE	45
VI-2	CALIBRATION LEVELS	46
VII-1	MODEL 1, UNCROSSED POLARIZATION	47
VII-2	MODEL 1, CROSSED POLARIZATION	48
VII-3	MODEL 1, UNCROSSED POLARIZATION, SMALL RECEIVER	49
VII-4	MODEL 2, UNCROSSED POLARIZATION (WITH LENS)	50
VII-5	MODEL 2, CROSSED POLARIZATION (WITH LENS)	51
VII-6	MODEL 2, UNCROSSED POLARIZATION (NO LENS)	52
VII-7	MODEL 2, FLAT PLATE, NO POLARIZATION	53
VII-8	MODEL 2, FLAT PLATE, UNCROSSED POLARIZATION	54
VII-9	MODEL 2, FLAT PLATE, CROSSED POLARIZATION	55
VII-10	MODEL 2, "PSEUDO" FLAT PLATE, NO POLARIZATION	56
VII-11	MODEL 3, UNCROSSED POLARIZATION (WITH LENS)	57
VII-12	MODEL 3, CROSSED POLARIZATION (WITH LENS)	58
VII-13	MODEL 3, UNCROSSED POLARIZATION (NO LENS)	59

FIGURE		PAGE
VII-14	MODEL 3, FLAT PLATE, UNCROSSED POLARIZATION (WITH LENS)	60
VII-15	MODEL 3, FLAT PLATE, CROSSED POLARIZATION (WITH LENS)	61
VII-16	MODEL 3, FLAT PLATE, UNCROSSED POLARIZATION (NO LENS)	62
VII-17	MODEL 4, UNCROSSED POLARIZATION	63
VII-18	MODEL 4, CROSSED POLARIZATION	64
VII-19	MODEL 5, UNCROSSED POLARIZATION	65
VII-20	MODEL 5, CROSSED POLARIZATION	66
VII-21	MODEL 5, FLAT PLATE, UNCROSSED POLARIZATION (WITH LENS)	67
VII-22	MODEL 5, FLAT PLATE, UNCROSSED POLARIZATION (NO LENS)	68
VII-23	MODEL 5, FLAT PLATE, CROSSED POLARIZATION (WITH LENS)	69
VII-24	MODEL 6, UNCROSSED POLARIZATION	70
VII-25	MODEL 6, CROSSED POLARIZATION	71
VII-26	MODEL 7, UNCROSSED POLARIZATION	72
VII-27	MODEL 7, CROSSED POLARIZATION (WITH LENS)	73
VII-28	MODEL 7, FLAT PLATE, UNCROSSED POLARIZATION	74
VII-29	MODEL 7, FLAT PLATE, CROSSED POLARIZATION (WITH LENS)	75
VII-30	MODEL 8, UNCROSSED POLARIZATION	76
VII-31	MODEL 8, CROSSED POLARIZATION	77

<u>FIGURE</u>		<u>PAGE</u>
VIII-1	REFLECTION DISTRIBUTION FUNCTIONS, NO POLARIZATION	78
VIII-2	REFLECTION DISTRIBUTION FUNCTIONS, NO POLARIZATION	79
VIII-3	REFLECTION DISTRIBUTION FUNCTIONS, UNCROSSED POLARIZATION	80
VIII-4	REFLECTION DISTRIBUTION FUNCTIONS, UNCROSSED POLARIZATION	81
VIII-5	REFLECTION DISTRIBUTION FUNCTIONS, CROSSED POLARIZATION	82
VIII-6	REFLECTION DISTRIBUTION FUNCTIONS, CROSSED POLARIZATION	83
VIII-7	MODEL 2, NO POLARIZATION	84
VIII-8	MODEL 2, UNCROSSED POLARIZATION	85
VIII-9	MODEL 2, CROSSED POLARIZATION	86
VIII-10	MODEL 3, NO POLARIZATION	87
VIII-11	MODEL 3, UNCROSSED POLARIZATION	88
VIII-12	MODEL 3, CROSSED POLARIZATION	89
VIII-13	MODEL 5, NO POLARIZATION	90
VIII-14	MODEL 5, UNCROSSED POLARIZATION	91
VIII-15	MODEL 5, CROSSED POLARIZATION	92
VIII-16	MODEL 7, NO POLARIZATION, 0° to $+180^\circ$ ASPECT ANGLE	93
VIII-17	MODEL 7, NO POLARIZATION, 0° to -180° ASPECT ANGLE	94

<u>FIGURE</u>		<u>PAGE</u>
VIII-18	MODEL 7, UNCROSSED POLARIZATION	95
VIII-19	MODEL 7, CROSSED POLARIZATION	96
VIII-20	MODEL X-1, NO POLARIZATION	97
VIII-21	MODEL X-1, UNCROSSED POLARIZATION	98
VIII-22	MODEL X-1, CROSSED POLARIZATION	99
VIII-23	MODEL Z, NO POLARIZATION	100
VIII-24	MODEL Z, UNCROSSED POLARIZATION	101
VIII-25	MODEL Z, UNCROSSED POLARIZATION USING "PSEUDO" FLAT PLATE DATA	102
VIII-26	MODEL Z, CROSSED POLARIZATION	103
VIII-27	MODEL DECOY, NO POLARIZATION	104
VIII-28	MODEL DECOY, UNCROSSED POLARIZATION	105
VIII-29	MODEL DECOY, CROSSED POLARIZATION	106

1. INTRODUCTION

This experimental investigation was undertaken in order to obtain characteristic scattering data at 10.6μ on model targets of interest to ABMDA/MICOM. The investigation primarily considered the measurement of the Laser Radar Cross Sections (LRCS) of the models as a function of aspect angle, polarization and surface characteristics. In addition, reflectance data were obtained on the various flat plate surfaces of each target in order to predict the backscattered intensity distributions using the RADC analytical model entitled BKSCAT. The ultimate objective is the capability of identifying unknown targets or discriminating between targets based upon the properties of the laser radar return.

The detection system used in this investigation recorded the intensity (power density) of the backscattered return from the various models. Each of the models differed in size, shape, surface coating and surface roughness. The radar cross section levels for each model were measured experimentally by comparing the scattered intensity levels with a known calibration level. In addition, two orthogonal polarization components of the scattered radiation were measured in order to determine which surfaces would retain or depolarize the incident polarization.

II. DESCRIPTION OF MODELS

Diagrams of the models used in this investigation appear in Figures II-1 and II-2.

MODEL 1

This model is a 6.35 cm diameter sphere made of beryllium. The surface was polished to about a 0.25 micron RMS surface height. This target was rotated about the center of the sphere.

MODEL 2

Model 2 is a teflon right circular cone with a 7.17 cm height and a 5 cm base. The target was rotated about an axis normal to the symmetry axis and located 4.8 cm from the tip of the nose.

MODEL 3

Model 3 is a spherical cap-truncated cone combination made of asbestos phenolic. The surface was smoothed using No. 180 grit sandpaper to about a 0.5 micron RMS surface height. The length of the target is 7.3 cm and the diameter of the base is 5.0 cm. The center of rotation is located 4.9 cm from the nose.

MODEL 4

Model 4 is a cone shaped target made of quartz. A heat shield material was then bonded to the surface. Finally a thin layer of sealant was applied. The length of the target is 13.2 cm and the center of rotation is 6.4 cm from the front tip.

MODEL 5

This cone-cylinder-flare combination was coated with .25 mm of a diffuse material on aluminum. The length of the target is 12.5 cm and the center of rotation is 8.5 cm from the front tip.

MODEL 6

Model 6 is a 6.35 cm diameter aluminized balloon, coated with thermal barrier material and formed from two one-mil mylar hemispheres.

MODEL 7

Model 7 is a sphere-cone-cylinder-flare combination. This target was also coated with a 0.25 mm diffuse coating on aluminum. The total length of this model is 15.3 cm, and the center of rotation is 7.5 cm from the front nose.

MODEL 8

Model 8 is a cone shaped object with a sharp tip and two separate ablative material sections. The surface was smoothed using No. 180 grit sandpaper. The total length of the target is 15.2 cm and the axis of rotation is 11.3 cm from the front tip.

DECOY

This model has the same shape as Model 8, however, the surface has been covered with a diffuse material. The center of rotation was 11.3 cm from the tip of the nose.

MODEL X-1

Model X-1 is a spherical cap-truncated cone combination made of linen phenolic. The length of the target is 11.0 cm and the diameter of the base is 8.7 cm. The center of rotation was located at a distance of 6.8 cm from the tip of the nose.

MODEL Z

Model Z is also a spherical cap-truncated cone combination made of linen phenolic. The length of this target is 18.9 cm and the diameter of the base is 6.3 cm. The center of rotation was located 12.6 cm from the tip of the nose.

III. SPECKLE ANALYSIS

For the majority of the targets measured in this analysis, some insight into the scattering processes can be obtained by considering the effect of the "speckle" lobes on the profile measurements. The "speckle" structure results when a coherent illumination source is used on a diffusely scattering surface. The resulting scattered distribution is a random interference

pattern of the reflected radiation from various surface elements. As the diffuse target rotates, this interference pattern moves across the detector surface thus causing a statistical signal fluctuation which depends upon the number of "speckle" lobes, N , impinging on the detector element. This number can be approximated for a given target by considering the following discussion.

From diffraction theory, we can estimate the approximate width of a speckle lobe, d , as:

$$d = R\lambda/W \quad (1)$$

where R is the range, λ is the wavelength, and W is the effective target illumination width. The area of a speckle in the x and y dimension is therefore

$$A_s = d_x d_y = R^2 \lambda^2 / W_x W_y \quad (2)$$

The number of "speckle" cells on the detector surface is therefore

$$N = \frac{A_R}{A_s} = \frac{A_R W_x W_y}{R^2 \lambda^2} \quad (3)$$

where A_R is the receiver area. Goodman [1] has shown that the total energy incident on a receiver aperture obeys the probability density function

$$p(I) = \frac{a^N I^{N-1} \exp[-aI]}{\Gamma(N)} \quad I \geq 0 \quad (4)$$

$$= 0$$

ELSEWHERE

where I is the intensity incident on the receiver aperture and a is the reciprocal of the average intensity per correlation cell with

$$N/a = \langle I \rangle \quad (5)$$

and

$$\frac{N}{a^2} = \sigma_A^2 \quad (6)$$

where σ_A^2 is the variance of this distribution. Equations (3), (5) and (6) yield the result

$$\frac{\sigma_A}{\langle I \rangle} = \frac{1}{\sqrt{N}} \approx \frac{R\lambda}{\sqrt{A_R} W} \quad (7)$$

where $W = W_x \approx W_y$ is the effective scattering diameter (width of the brightness distribution) on the target. Solving Equation (7) for W

$$W \approx \frac{R\lambda}{\sqrt{A_R}} \left[\frac{\sigma_A}{\langle I \rangle} \right]^{-1} \quad (8)$$

Equation (8) indicates that the amplitude fluctuations (ratio of the standard deviation to the mean) resulting from the speckle modulation provide a means of measuring the approximate scattering width on the target. By using a polarization analyzer on the receiver, the effective scattering area of the target which scatters each polarization component can be determined. These measurements offered information regarding the size of the effective area of the regions on the target which preserved or randomly distributed the incident polarization. For example, on some of the curved metal surfaces, the surface roughness caused the depolarization of the back-scattered radiation and it also caused the width of the brightness distribution to increase for the crossed polarized case. As a consequence, the crossed polarization components often had a much smaller modulation amplitude than the uncrossed component.

IV. EXPERIMENTAL ARRANGEMENT

Figure IV-1 is a schematic of the experimental arrangement used in this analysis. The 10.6 μ polarized output from a CRL Model 42 CO₂ laser was expanded and collimated in order to

provide a 13 cm diameter incident beam with a uniform phase distribution over the surface of the models. The models were mounted and rotated on a Scientific Atlanta (SA) azimuth positioner. The backscattered intensity distribution was measured with a Raytheon Model IR-102 PbSnTe photovoltaic detector positioned at a range R from the center of rotation. The bistatic angle θ_B is shown in Figure IV-1 and was 4° for this arrangement.

The voltage output from the detector was measured with an SA pen recorder model 1525 which logarithmically plotted the backscattered intensity distribution as a function of the orientation of the target. A 1 KHz amplitude modulated signal was provided to the narrow band input of the SA recorder by chopping the incident light beam with a Princeton Applied Research model 191 variable speed light chopper.

Two orthogonal polarization components of the back-scattered radiation were analyzed by using a Perkin-Elmer wire grid polarizer in front of the detector. One polarization component was perpendicular to the plane of incidence while the other was parallel to this plane. The incident beam polarization was maintained in a direction perpendicular to the plane of incidence for all the measurements. The polarization extinction ratio of the polarizer was 23 db.

V. EXPERIMENTAL PROCEDURE

The entire receiver system was analyzed in order to calibrate the recorded levels on the pen recorder chart paper in terms of backscattered power. Convex mirrors with various radii of curvature were used in order to determine the linear dynamic range of the receiving system. The system was determined to be linear over the dynamic range used in this investigation. A 20 cm radius of curvature convex mirror was also used as a calibration standard to compare cross sectional levels.

The incident beam profile was obtained by mounting the detector on the azimuth positioner facing the incident beam at a distance of 100 cm from position 0 as shown in Figure IV-2. As the positioner was rotated, the detector scanned through the incident beam. The intensity distribution was then recorded with the pen recorder.

Each model was mounted on a supporting rod and rotated in azimuth about position 0 as shown in Figure IV-1. The background was measured by removing the target and noting the noise level from the holder.

Figure IV-3 shows the experimental arrangement used to measure the flat plate scattering distributions. The flat surfaces of the appropriate models were placed over the

center of rotation on the azimuth positioner and illuminated with a narrow incident beam. The bistatic angle, θ_B , for this arrangement was $2^\circ 50'$. The incident power level for this setup was also measured in order to calculate the values of the reflectance function, $G(\theta)$, described later.

VI. EXPERIMENTAL CALIBRATION

The intensity distribution of the incident beam used to measure the LRCS of each model is shown in Figure VI-1. The full width at the half power level is 7.6 cm and the truncated width is approximately 13 cm. The truncation of the beam is due to the restriction by the 5 inch diameter transmitter mirror, M_3 . The detector aperture diameter was 0.356 mm for this measurement. Figure VI-2 shows four intensity levels, measured on the pen recorder. Level A is a relative measurement of the incident intensity level whereas levels B through D are measurements of the backscattered intensity levels from a 20 cm radius of curvature convex mirror at ranges of 100 cm, 175 cm and 200 cm, respectively. Level A had 20 db more attenuation than levels B through D. These levels were then used to determine the capability of measuring the predicted backscatter from the spherical standard. The ratio of the power densities of the scattered to the incident beam is given as

$$P_s/P_i = \frac{\rho r^2}{(r + 2R)^2} \quad (9)$$

where r is the radius of curvature of the spherical mirror, ρ is the reflectivity of the mirror and R is the range from the surface of the sphere to the detector. Using 20 cm for r , 0.995 for ρ and 100 cm for R , a value of 0.0082 or a difference of

20.8 db is expected between the incident beam level and the return from the sphere. A difference of 20.7 db was measured between level A and level B thus yielding a 2.3% error. At a range of 175 cm, a 25.3 db difference is expected. Levels A and C indicate a 24.9 db difference yielding a 9.8% error. At 200 cm, a 26.4 db difference is expected and 26.5 db was measured between levels A and D, yielding a percentage error of 2.3%.

The far-field cross section σ of a specular spherical calibration standard is given by the expression

$$\sigma = \rho \pi r^2 \quad (10)$$

where r is the radius of curvature and ρ is the reflectivity; however, the near-field expression for σ must be used when the range R is comparable with r . In this case, the expression

$$\sigma = \rho \pi r^2 \left[\frac{2R}{r + 2R} \right]^2 \quad (11)$$

is used. The expression in the bracket approaches unity for $R \gg r$ so that Eq. (11) approaches Eq. (10) in the far-field. At a range of 100 cm, using 20 cm for r and 0.995 for ρ , the cross section of this standard is 1033.4 cm².

A 1 db insertion loss and a 23 db polarization ratio between the two orthogonal components of polarization were measured for the wire grid polarizer.

VII. EXPERIMENTAL RESULTS

The experimental results for each model are now presented. The LRCS measurements on targets with effective scattering dimensions greater than or equal to the width of the incident beam will be affected by the truncation of the beam profile. In order

to determine the LRCS of the targets illuminated with a uniform intensity distribution, the analytical model described in Section VIII was used for the additional purpose of determining factors which correct for the nonuniform illumination in some of the measurements. Table 1 shows these correction factors for four of the models used in this analysis at several target aspect angles. These factors represent the difference in the analytically predicted backscatter levels between the uniform and nonuniform illumination case at particular aspect angles.

In the discussions to follow, "uncrossed polarization" will be used to describe the condition in which both the transmitter and receiver polarization directions are normal to the plane of incidence and "crossed polarization" will describe the case in which the transmitter polarization is normal and the receiver polarizer is parallel to the plane of incidence.

MODEL 1

Figures VII-1 and VII-2 show the backscattered distribution of this metallic, 3.17 cm radius of curvature sphere for the uncrossed and crossed polarization components, respectively. The average level of the scattered distribution for the uncrossed polarization component was 16 db below that of the

20 cm radius of curvature mirror yielding a cross section of 26 cm^2 . A value of 31.6 cm^2 was calculated using the expression πr^2 where r is 3.17 cm. This indicates that the reflectivity is less than unity. Since the effective scattering area of this target is illuminated with a uniform portion of the incident beam, no correction has to be made to account for the Gaussian beam distribution versus a uniform distribution. The cross polarized component in Figure VII-2 was 17 db lower than the uncrossed polarized component. This measurement indicates that approximately 2% of the backscattered return is depolarized.

The amplitude modulation in Figures VII-1 and VII-2 shows the statistical fluctuations of the detected signal caused by the speckle lobes as they sweep across the detector aperture. Figure VII-1 indicates that the magnitude of the signal fluctuations are approximately 2 db. In Figure VII-2, however, the crossed polarized component has a 0.4 db amplitude fluctuation. Equation (8) indicates that the effective target diameter from which the crossed polarization component was scattered is larger than that for the uncrossed polarization component. This is consistent with the assumption that the uncrossed polarization component stems primarily from a small specular region while the depolarized radiation originates

from rough surface scattering over a much larger area.

In order to observe an increase in the speckle amplitude modulation, a 0.356 mm diameter aperture was used in front of the detector. The resulting pattern is shown in Figure VII-3.

MODEL 2

Figures VII-4 and VII-5 show the backscattered pattern for the teflon cone for the cases of uncrossed and crossed polarization. These patterns do not go beyond $\pm 100^\circ$ from the nose-on position due to the fact that the back of this model had been drilled and taped for mounting. Since the signal level for the crossed polarization component was too low to be measured with the 2 mm square detector element, these profiles were taken using a lens in front of the detector. Figure VII-6 is the pattern for the uncrossed polarization component using the 2 mm square detector element. The small peak near the nose-on region in Figure VII-4 was determined to be coming from the entire surface area on the sides of the cone. This was verified by probing the region immediately in front of the target with a material which diverted the incident radiation. It is suspected that the surface scratches due to the machining process caused this increase.

Figures VII-7 through VII-9 are the flat plate profiles using the lens in the receiver. These figures show the cases for no receiver polarization, uncrossed and crossed polarization, respectively. Figure VII-10 is the pattern for a "pseudo"¹ flat plate distribution using the side of the cone. No receiver polarizer was used for this case.

The broadside for this cone shaped model peaked at 74° from the nose-on position as expected. The return at broadside was 21.5 db below the return from the 20 cm radius of curvature mirror while that of the nose-on was 38 db below. Therefore, the cross section levels were measured to be 7.4 cm² and 0.165 cm², respectively. Using the correction factor in Table 1, the corresponding LRCS levels for a uniform incident beam are 9.3 cm² and 0.190 cm².

It was noted that 0.5 db of the 1 db amplitude modulation near nose-on in Figures VII-5 and VII-6 is the result of the system noise due to the low signal level. This noise level masked the speckle modulation. However, the 10 db difference between the received orthogonal polarization components in the

1. The term "pseudo" flat plate is used to describe the flat plate distributions obtained using a curved portion of the target. A narrow incident beam is used in order to ensure that the surface is essentially flat to the incident beam. The technique of using "pseudo" flat plate data has proven to be useful when modeling targets with surface roughness variations on the curved surface versus the flat surface.

nose-on region shown in Figures VII-5 and VII-6 indicate a significant amount of depolarization is occurring in this region. Again, the surface scratches are very likely the cause of this backscatter.

MODEL 3

The two orthogonal receiver polarization components for the scattering patterns from Model 3 are shown in Figures VII-11 and VII-12. These patterns were taken using the lens in the receiver system in order to increase the signal level. Figure VII-13 has the same polarization orientation as Figure VII-11, however, the 2 mm square detector element was used. The flat plate profiles for this model are shown in Figures VII-14 and VII-15. As shown in the profiles, there is a 23 db difference in the two polarization levels near normal incidence and approximately an 11 db difference at the 36° angular orientation. This indicates that for the specular backscatter component, the direction of the incident polarization has been retained while in the case of the diffuse component, it has been depolarized. Figure VII-16 is the flat plate distribution for the uncrossed polarization case using the 2 mm square detector element. Figures VII-11 and VII-13 indicate the appearance of large speckle amplitude fluctuations in the

nose-on region for the uncrossed polarization component while Figure VII-12 reveals a decrease in these fluctuations for the crossed polarization case. Again, the difference in the amplitude of the speckle fluctuations from the nose-on region between the crossed and the uncrossed polarization schemes may be due to the differences in the size of the effective scattering areas. The flat plate distribution in Figure VII-16 shows approximately 2 db fluctuations in the speckle modulation. The incident beam for this case was approximately 1 cm in diameter. The scattering from the nose of Model 3 in Figure VII-13 using the same receiver size as that used in Figure VII-16 has a 2.5 db amplitude fluctuation. Using Equation (8) and the observation made in Figure VII-16, this measurement indicates that the effective scattering width from the nose is slightly less than 1 cm. Since the spherically shaped front nose had a 2.7 cm diameter, this measurement indicates that the uncrossed polarization is coming from an area which is smaller than the total area of the spherical nose, yet larger than the equivalent flat plate diameter, 0.42 mm.

The broadside peak of Model 3 is approximately 19 db below that of the standard; that of the nose was 32 db lower, and the backend was 5 db lower. The LRCS levels are 12.6 cm^2 ,

0.67 cm² and 330 cm², respectively. Table 1 indicates that the corrected LRCS values for the uniform illumination case are 15.5 cm² for the broadside, 0.70 cm² for the nose, and 383 cm² for the backend.

MODEL 4

Figure VII-17 shows the backscattered pattern for Model 4 in the uncrossed polarization case. The axis of rotation was located at the midpoint of the length of the model and was perpendicular to the axis of symmetry.

This pattern reveals that backscatter characteristics were obtained from the front edges and broadsides of the side windows as well as from the nose and broadsides of the model itself.

The crossed polarized pattern shown in Figure VII-18 did not reveal much information since the signal level was too low to be measured. However, a large difference in the two polarization components for the scattering from the broadsides of the windows and the model itself was measured and it indicates that the scattering from these surfaces has retained its original polarization direction.

The backscattered return from the nose section for the uncrossed polarization case was 40.25 db below the standard,

thus yielding a cross section level of 0.098 cm^2 while the broadside level was measured to have a cross section level of 41.6 cm^2 . Finally, the return from the side window reached the 26 cm^2 level.

In the nose-on orientation, speckle amplitude fluctuations are again largely due to the small effective scattering area for this position of the target. These fluctuations decrease as the broadside is approached since the scattering area increases.

MODEL 5

Model 5 was mounted with the axis of rotation located 4.3 cm from the backend. The two orthogonal receiver polarization components for the scattering patterns from this model are shown in Figures VII-19 and VII-20. The pattern shown in Figure VII-19 was taken using the 2 mm square detector aperture while that shown in Figure VII-20 was taken using the one inch diameter lens in the receiver system. The peak near 72° from nose-on is due to the backscatter from both the broadside of the front nose cone and from the back flare section. The separation of the peaks from each of these two areas was calculated to be about 1.5° , but an attempt to resolve the scattering from each was unsuccessful because the reflected level from each section was approximately the same.

The return from the nose region was measured to be 41 db below the standard, the broadside measurement was 27 db lower and the backend was 23 db lower. The corresponding LRCS levels are 0.083 cm², 2.1 cm², and 5.2 cm². Table 1 shows that the LRCS levels for a uniform incident beam are 0.10 cm² for the nose, 3.1 cm² for the broadside and 6.2 cm² for the backend.

The flat plate profiles for this model are shown in Figures VII-21 through VII-23. Figures VII-21 and VII-22 are the profiles for the uncrossed polarization case using the one inch diameter lens and the 2 mm square aperture, respectively. A smaller incident beam width was also used in Figure VII-22. Figure VII-23 is the profile for the crossed polarization case using the lens in the receiver. Figures VII-21 and VII-22 reveal the noticeable difference in the "speckle" amplitude modulation due to the difference in the receiver and the incident beam size. However, the general shape of the distributions are the same.

MODEL 6

Model 6 was mounted with a support rod connected to the inflation valve and rotated about its center. Figures VII-24 and VII-25 show the two polarization components. Although the

balloon was inflated, the wrinkles in the surface were significant enough to cause a large amplitude modulation. The amplitude level of the pattern in Figure VII-25, taken with the crossed polarized receiver, indicates that the surface caused a noticeable amount of depolarization. In this case, the return is coming primarily from the region referred to as the "overlap" region.

Since this spherically shaped target has a 6.35 cm diameter, the radar cross section is approximately 31 cm^2 . The near-field cross section for the 20 cm radius of curvature standard is 1033 cm^2 so that the expected difference between this target and the standard is 15.2 db. In Figure VII-24 it is difficult to determine the average return from this target. However, it is approximately 17 db below the reference standard or 21 cm^2 in a cross section. The large difference is attributed to the gross surface irregularities.

MODEL 7

The two orthogonal receiver polarization components for the scattering patterns from Model 7 are shown in Figures VII-26 and VII-27. Since Model 7 is made of the same surface material as Model 5, the flat plate data from Model 5 was used to predict the scattering distribution for this model. The

back of Model 7, however, is made of a fiberglass material. The two orthogonal polarization components for the flat plate distributions on the fiberglass surface are shown in Figures VII-28 and VII-29. Figures VII-27 and VII-29 were taken using the lens in the receiver system.

The center of rotation for Model 7 was located at a distance of 7.2 cm from the nose along the symmetry axis of the body. Figure VII-26 indicates that the distinctive scattering regions on this model are the nose, the broadside of nose cone, the broadside of cylinder section, both flare sections, the flare on the base section, and the back end. The returns from the broadsides of the nose cone and the two flares were calculated to appear at 65° , 72° , and 82° from nose-on after correcting for the bistatic angle. Figure VII-26 shows that the returns from these regions merge to form a "shoulder" next to the return from the broadside of the cylinder section. The cross section of the nose was measured to be 0.21 cm^2 , the return from the broadside of the cylinder was 4.15 cm^2 and that from the back end was 16.5 cm^2 . The corrected LRCS values for the uniform illumination case are 0.25 cm^2 , 6.5 cm^2 and 17.4 cm^2 , respectively.

MODEL 8

The center of rotation for Model 8 was 11.3 cm from the nose along the line of symmetry. Figures VII-30 and VII-31 show the patterns for the two polarization components. These figures indicate a significant amount of depolarization from all sections of the model except the broadside. The crossed polarized return at the nose-on position, however, dropped below the sensitivity range of the recording system.

The return from the broadside of the cone was predicted to peak at 81° . The experimental result is in good agreement with this value. The amplitude fluctuations for the two orthogonal polarization cases did not change appreciably, indicating that each polarization component was coming from the same effective area size. Since a significant amount of depolarization was measured, it is suspected that the depolarization mechanism is a subsurface rather than a rough surface effect.

The cross section level from the nose was measured at 0.34 cm^2 while that from the broadside of the target was 10.6 cm^2 .

VIII. ANALYTICAL BACKSCATTER ESTIMATES

A. INTRODUCTION

In addition to measuring backscatter, we can predict it analytically. There are several possible approaches

to the problem. One method utilizes the surface roughness characteristics of a target material plus an approximate solution of the problem of the scattering of an electromagnetic wave from a rough surface. However, this method is very complex mathematically. We have used another technique which predicts target backscatter from measured flat plate scattering data. We tested this method by comparing predicted backscatter with measured backscatter from four of the MICOM targets plus three other laboratory targets.

B. TARGET BACKSCATTER CALCULATIONS

Target backscatter is calculated by approximating the geometry of an object as a composite of flat plates and summing the backscatter from each of the surface elements. Simple shapes such as cones, cylinders, spheres, and discs are used to form the gross structure of a target. Then these basic shapes are decomposed into the flat plates. The magnitude of the individual backscatter contributions is found from the flat plate data and the orientation of each sub-area with respect to the line-of-sight. The mathematical expression for the backscatter is found to be the following:

$$\text{Backscatter} = \sum_{i=1}^N G(\theta_i) \cos(\theta_i) A_i f_i P_0 \Omega_d$$

where

- Backscatter = Detector Response (watts)
- θ_i = The orientation of the i th sub-area; specifically the angle between the sub-area normal and the line-of-sight (degrees)
- $G(\theta_i)$ = Backscatter function for the i th sub-area oriented at angle θ_i (steradian⁻¹)
- f_i = Gaussian illumination factor; (no units)
- A_i = Physical size of the i th sub-element (m²)
- P_0 = Maximum incident power density (watts/m²)
- Ω_d = Solid angle of receiving aperture (steradian)

C. THE FLAT PLATE SCATTERING FUNCTION

The reflection distribution function $G(\theta)$ for a given material is determined experimentally by rotating a flat sample of the material in a beam and recording the backscatter as a function of aspect. Generally only monostatic data is measured although bistatic data can also be obtained by rotating the detector. The data are reduced via the following formula:

$$G(\theta) = \frac{\text{Power Received in Detector}}{(\text{Power Incident})(\text{Solid Angle of Detector})}$$

in units of steradians⁻¹

$G(\theta)$ is also a function of incident and received polarization. $G_{xy}(\theta)$ is the polarization vector notation for $G(\theta)$ where x and y describe the transmitter and receiver electric field directions respectively and 1 and 2 refer to the cases of perpendicular and parallel to the plane of incidence, respectively. The case $y = 0$ implies that no receiver polarizer is used.

The experimental data are sampled at 21 discrete angles to describe the scattering function. Linear interpolation is used to obtain values at arbitrary angles. Figures VIII-1 through VIII-6 illustrate the reduced scattering data which were measured during this study. The tabulated data also appear in Table 2. We have assumed that the scattered function drops to 0 at 90° .

The data are often difficult to obtain for large values of θ . The signal level is generally low and one must be sure that the return is not coming from the edge of the sample. As such, the reliability of the data is reduced for angles beyond 70 or 80° from normal. However, the problem is minimized by the fact that since the return from poorly oriented portions of a target is small the effect of any accompanying error in the flat plate data is likewise small.

D. ANALYTICAL COMPARISON WITH EXPERIMENTAL DATA

We have used the above method (along with a computer program) to calculate the backscatter from the laboratory

targets as a function of aspect angle for 3 receiver polarization cases. Figures VIII-7 through VIII-29 show the calculated versus experimental backscatter for each target. The targets shown are drawn to one-half the full size of the model and were modeled as fairly obvious combinations of cones, cylinders, spheres, discs, and one ogive.

The agreement between the experimental and analytical results ranges from excellent to poor. Generally the analytical method predicted the no polarization and uncrossed polarization backscatter more accurately than for the crossed polarized case. One of the key reasons for the discrepancies in all three cases is thought to be variation of surface roughness. We measure the backscatter properties of a flat sample of the surface material of the target. But the machining of finish on a given target may not be the same as that on the flat sample. Target Z illustrates the problem. Flat plate data from the back end of the target were used to predict the backscatter from the entire model. Figure VIII-24 shows the analytical estimates to be low for the conically shaped main body. But when pseudo-flat plate data taken from the broadside of the cone were used, the agreement was much better (Figure VIII-25). Figure VIII-3 shows the difference in the flat plate data taken on the seemingly uniform surface

of Model 2. The same problem occurs for Model 7. Figures VIII-16 and VIII-17 show a substantial difference between the experimental backscatter patterns for the two sides of the same target. To the eye, however, the target surface seems to be uniform. Another fundamental problem stems from machined edges, ridges, or other surface irregularities. We model targets as smooth cones and cylinders but sometimes this is not the case. For example, for Model 2 (Figure VIII-7) it is felt that the small peak in the backscatter pattern at nose-on aspect is due in part to ridges that run around the axis of the target. Another example is the decoy cone (Figures VIII-27 through VIII-29) - where the surface of the cloth makes for very difficult scattering predictions. Many real world targets, of course, have countless protrusions which are not included in the geometric modeling. The hope is that the basic structure of the target will allow the primary features of the backscatter to be calculated and that these will be sufficient for target discrimination.

It is difficult to explain the discrepancies between the calculated and experimental results for the cross polarization case. Since the crossed polarized flat plate data are generally flatter than the co-polarized case, the results are more sensitive to errors at large scattering angles. More likely,

however, the surface properties on the flat portions of the models from which the reflectance data was taken is not like that of the curved regions. It is also possible, however, that the backscatter mechanism by which the signal becomes cross-polarized may be too complex to be predicted accurately by decomposing a body into flat plates.

IX. CONCLUSIONS

The experimental results were compared to those predicted by the RADC analytical computer model, BKSCAT. Figures VIII-7 through VIII-29 illustrate the agreement obtainable between calculated and experimental backscatter. Very good agreement was obtained for targets from which representative flat plate reflectance data can be obtained. This can be accomplished if the entire surface of the model is the same as that of the flat plate sample. For targets which do not satisfy this criterion, more noticeable disagreement was obtained. This was especially noted on targets where the curved portions had a surface roughness unlike that of the flat plate. However, some success in the modeling was obtained for these targets using reflectance profiles from the curved portions of the surface in addition to those from the flat surfaces.

The difficulty experienced in modeling the crossed polarized backscatter cannot be easily explained at this point. It is possible that the mechanism causing this backscatter cannot be accounted for by this model. An example of such a mechanism would be the subsurface volumetric scattering which is presently being investigated [2].

During the experimental investigation it was noted that in general, the speckle amplitude modulation from the curved surfaces was larger for the uncrossed polarization case than for the crossed case. It is suspected that the difference in this modulation level may be the result of different effective scattering areas for each orthogonal polarization component. The uncrossed polarization component may stem primarily from a small specular region while the depolarized radiation originates from rough surface scattering over a much larger area.

The important question though, is whether or not the measurable differences in the backscatter between two targets are sufficient for real world discrimination. The figures show considerable variation in the backscatter patterns among the targets in the study. We must now investigate how much this information is degraded by the

errors and uncertainties in the real world. And eventually we will have even more powerful tools of discrimination such as doppler shift and RTI patterns at our disposal.

REFERENCES

1. Goodman, J. W., "Some Effects of Target-induced Scintillation on Optical Radar Performance, Proc. IEEE, Vol. 53, No 11, Nov 1965.
2. Leader, J.C., Dalton, W.A.J., "Bidirectional Scattering of Electromagnetic Waves from the Volume of Dielectric Materials", J. Appl. Phys., Vol. 43, No 7, July 1972.

	MODEL NUMBER	EXPERIMENTAL LRCS	CORRECTION	PREDICTED LRCS
NOSE	2	0.165 cm ²	1.15	0.190 cm ²
	3	0.670 cm ²	1.04	0.700 cm ²
	5	0.083 cm ²	1.22	0.101 cm ²
	7	0.210 cm ²	1.56	0.252 cm ²
BROADSIDE	2 at 74°	7.4 cm ²	1.26	9.3 cm ²
	3 at 79°	12.6 cm ²	1.23	15.5 cm ²
	5 at 90°	2.1 cm ²	1.46	3.1 cm ²
	7 at 90°	4.15 cm ²	1.56	6.5 cm ²
BACKEND	3	330 cm ²	1.16	383 cm ²
	5	5.2 cm ²	1.19	6.2 cm ²
	7	16.5 cm ²	1.05	17.4 cm ²

Table 1. Laser Radar Cross Section Correction Factors
for Uniform Illumination

FLAT PLATE SCATTERING DATA IN INVERSE STERADIANS

MONOSTATIC FLAT PLATE DATA KEY

		<u>XY+</u>
1	MICOM MODEL 2 -	10
2	MICOM MODEL 2 -	PSEUDO 10
3	MICOM MODEL 2 -	11
4	MICOM MODEL 2 -	12
5	MICOM MODEL 3 -	10
6	MICOM MODEL 3 -	11
7	MICOM MODEL 3 -	12
8	MICOM MODEL 5 -	10
9	MICOM MODEL 5 -	11
10	MICOM MODEL 5 -	12
11	MICOM MODEL 7 -	BACK END - 10
12	MICOM MODEL 7 -	BACK END - 11
13	MICOM MODEL 7 -	BACK END - 12
14	MODEL X -	10
15	MODEL X -	11
16	MODEL X -	12
17	MODEL Z -	10
18	MODEL Z -	11
19	MODEL Z -	PSEUDO - 11
20	MODEL Z -	12
21	MODEL DECOY -	10
22	MODEL DECOY -	11
23	MODEL DECOY -	12

+ XY ARE THE SUBSCRIPTS ON $G_{xy}(\theta)$ DEFINED IN THE TEXT.

Table 2

FLAT PLATE SCATTERING DATA IN INVERSE STERADIANS

1	MICOM MODEL 2 - 10
2	MICOM MODEL 2 - PSEUDO 10
3	MICOM MODEL 2 - 11
4	MICOM MODEL 2 - 11
5	MICOM MODEL 3 - 10

THETA (DEG)	1	2	3	4	5
0	8.9E-02	1.4E-01	6.6E-02	5.5E-04	3.5E-01
1	7.0E-02	5.2E-02	6.9E-02	4.4E-04	8.3E-01
2	5.6E-02	4.3E-02	5.5E-02	3.0E-04	5.8E-01
3	4.5E-02	3.8E-02	4.3E-02	2.3E-04	3.0E-01
4	3.7E-02	3.1E-02	3.4E-02	1.9E-04	2.0E-01
5	2.8E-02	2.4E-02	2.1E-02	1.8E-04	1.4E-01
6	2.3E-02	1.7E-02	1.6E-02	1.5E-04	1.1E-01
9	1.4E-02	1.4E-02	9.7E-03	1.4E-04	5.3E-02
12	1.0E-02	9.6E-03	5.7E-03	1.3E-04	3.5E-02
16	5.0E-03	6.2E-03	3.2E-03	1.3E-04	1.6E-02
24	2.8E-03	3.8E-03	1.8E-03	1.3E-04	9.4E-03
32	1.8E-03	2.7E-03	1.4E-03	1.3E-04	6.2E-03
36	1.3E-03	2.2E-03	7.4E-04	1.3E-04	4.0E-03
42	7.1E-04	1.7E-03	4.7E-04	1.3E-04	2.4E-03
48	6.3E-04	1.6E-03	4.4E-04	1.3E-04	1.9E-03
54	5.6E-04	1.2E-03	3.9E-04	1.3E-04	1.8E-03
60	5.0E-04	1.1E-03	3.5E-04	1.3E-04	1.8E-03
66	4.5E-04	9.5E-04	3.2E-04	1.3E-04	1.7E-03
72	4.2E-04	7.5E-04	2.9E-04	1.3E-04	1.6E-03
78	2.5E-04	4.8E-04	1.8E-04	1.3E-04	8.0E-04
90	.	0.	1.	0.	0.

TABLE 2 REFLECTION DISTRIBUTION FUNCTIONS

Copy available to DDC does not
permit fully legible reproduction

FLAT PLATE SCATTERING DATA IN INVERSE STERADIANS

6	MICOM MODEL 3 - 11
7	MICOM MODEL 3 - 12
8	MICOM MODEL 5 - 10
9	MICOM MODEL 5 - 11
10	MICOM MODEL 5 - 12

THETA (DEG)	6	7	8	9	10
0	3.5E-01	1.9E-01	3.7E-02	4.2E-02	2.4E-04
1	6.6E-01	5.8E-03	3.2E-02	3.4E-02	2.4E-04
2	3.3E-01	5.2E-03	3.0E-02	2.9E-02	2.4E-04
3	1.9E-01	4.2E-03	2.6E-02	2.4E-02	2.3E-04
4	1.3E-01	2.4E-03	2.2E-02	2.1E-02	2.3E-04
5	1.0E-01	2.3E-03	2.1E-02	2.0E-02	2.1E-04
6	9.3E-02	2.0E-03	1.7E-02	1.8E-02	2.1E-04
9	5.3E-02	1.4E-03	1.3E-02	1.4E-02	2.0E-04
12	3.3E-02	1.1E-03	9.8E-03	1.1E-02	1.9E-04
18	1.5E-02	7.2E-04	5.9E-03	7.1E-03	1.6E-04
24	9.3E-03	5.8E-04	3.8E-03	4.7E-03	1.5E-04
30	5.3E-03	4.9E-04	2.8E-03	3.2E-03	1.4E-04
36	3.3E-03	4.0E-04	1.9E-03	2.3E-03	1.4E-04
42	2.1E-03	3.7E-04	1.5E-03	1.6E-03	1.3E-04
48	1.6E-03	3.3E-04	1.1E-03	1.1E-03	1.2E-04
54	1.3E-03	2.9E-04	8.9E-04	8.8E-04	1.0E-04
60	1.0E-03	2.5E-04	7.1E-04	6.3E-04	8.3E-05
66	8.5E-04	2.4E-04	5.9E-04	5.0E-04	7.1E-05
72	8.6E-04	2.4E-04	4.2E-04	3.8E-04	5.7E-05
80	7.6E-04	2.0E-04	2.6E-04	2.5E-04	3.0E-05
90	0.	0.	0.	0.	0.

TABLE 2 REFLECTION DISTRIBUTION FUNCTIONS

FLAT PLATE SCATTERING DATA IN INVERSE STERADIANS

11	MICOM MODEL 7 - BACK END - 10
12	MICOM MODEL 7 - BACK END - 11
13	MICOM MODEL 7 - BACK END - 12
14	MODEL X - 10
15	MODEL X - 11

THETA (DEG)	11	12	13	14	15
0	4.2E-01	4.2E-01	3.0E-02	6.6E-02	5.2E-02
1	2.9E-01	2.9E-01	2.5E-02	6.0E-02	4.9E-02
2	1.7E-01	1.9E-01	1.6E-02	5.6E-02	4.7E-02
3	9.3E-02	9.7E-02	1.4E-02	5.2E-02	4.2E-02
4	5.9E-02	6.2E-02	9.5E-03	4.9E-02	3.7E-02
5	4.4E-02	4.7E-02	8.4E-03	4.6E-02	3.4E-02
6	2.9E-02	3.2E-02	7.6E-03	4.2E-02	3.0E-02
9	1.2E-02	1.5E-02	6.4E-03	3.3E-02	2.5E-02
12	6.6E-03	6.6E-03	5.7E-03	2.6E-02	2.0E-02
18	2.9E-03	3.3E-03	5.3E-03	1.9E-02	1.5E-02
24	1.7E-03	1.9E-03	5.0E-03	1.5E-02	1.0E-02
30	1.0E-03	1.2E-03	4.9E-03	1.2E-02	8.2E-03
36	8.2E-04	9.3E-04	4.6E-03	9.8E-03	7.1E-03
42	6.6E-04	6.6E-04	4.6E-03	8.9E-03	6.0E-03
48	5.2E-04	5.3E-04	4.7E-03	8.2E-03	5.5E-03
54	4.2E-04	4.0E-04	4.5E-03	7.4E-03	5.2E-03
60	3.3E-04	3.3E-04	4.5E-03	7.1E-03	4.9E-03
66	2.3E-04	2.4E-04	4.3E-03	6.9E-03	4.7E-03
72	2.1E-04	1.8E-04	4.3E-03	6.6E-03	4.7E-03
80	1.7E-04	1.4E-04	4.2E-03	6.6E-03	4.7E-03
90	0.	0.	0.	0.	0.

TABLE 2 REFLECTION DISTRIBUTION FUNCTIONS

Copy available to DDC does not
 permit fully legible reproduction

FLAT PLATE SCATTERING DATA IN INVERSE STERADIANS

16	MODEL X - 12
17	MODEL Z - 10
18	MODEL Z - 11
19	MODEL Z - PSEUDO - 11
20	MODEL Z - 12

THETA (DEG)	16	17	18	19	20
0	1.4E-03	5.2E-01	7.6E-01	1.4E-01	1.4E-03
1	1.4E-03	2.3E-01	3.5E-01	9.5E-02	1.1E-03
2	1.4E-03	1.3E-01	1.8E-01	7.4E-02	7.9E-04
3	1.4E-03	5.2E-02	1.1E-01	5.9E-02	5.0E-04
4	1.4E-03	4.6E-02	5.5E-02	4.8E-02	4.0E-04
5	1.4E-03	2.9E-02	3.5E-02	4.2E-02	3.5E-04
6	1.4E-03	1.8E-02	2.8E-02	3.5E-02	3.3E-04
9	1.4E-03	1.0E-02	1.4E-02	2.6E-02	3.0E-04
12	1.4E-03	6.6E-03	9.7E-03	1.9E-02	2.8E-04
18	1.4E-03	3.5E-03	4.9E-03	1.2E-02	2.5E-04
24	1.4E-03	2.3E-03	2.6E-03	7.4E-03	2.3E-04
30	1.4E-03	1.4E-03	1.9E-03	5.3E-03	2.1E-04
36	1.4E-03	1.3E-03	1.4E-03	4.2E-03	2.0E-04
42	1.4E-03	1.1E-03	1.1E-03	3.4E-03	1.8E-04
48	1.4E-03	9.0E-04	8.8E-04	2.6E-03	1.8E-04
54	1.3E-03	7.0E-04	7.6E-04	2.1E-03	1.6E-04
60	1.3E-03	6.0E-04	5.4E-04	1.8E-03	1.4E-04
66	1.3E-03	5.0E-04	5.1E-04	1.5E-03	1.3E-04
72	1.4E-03	4.0E-04	4.2E-04	1.2E-03	1.1E-04
84	1.5E-03	3.0E-04	3.5E-04	1.0E-03	6.9E-05
90	0.	0.	0.	0.	0.

TABLE 2 REFLECTION DISTRIBUTION FUNCTIONS

FLAT PLATE SCATTERING DATA IN INVERSE STERADIANS

21	MODEL DECOY - 10
22	MODEL DECOY - 11
23	MODEL DECOY - 12

THETA (DEG)	21	22	23
0	7.6E-02	6.9E-02	3.4E-03
1	7.6E-02	5.9E-02	3.4E-03
2	7.6E-02	6.9E-02	3.4E-03
3	7.6E-02	6.9E-02	3.4E-03
4	7.6E-02	6.9E-02	3.4E-03
5	7.6E-02	6.9E-02	3.4E-03
6	7.6E-02	6.9E-02	3.4E-03
9	7.6E-02	6.9E-02	3.4E-03
12	7.3E-02	6.7E-02	3.2E-03
16	5.6E-02	5.2E-02	2.1E-03
24	4.4E-02	3.0E-02	1.2E-03
30	3.9E-02	3.7E-02	1.1E-03
36	3.9E-02	3.5E-02	1.1E-03
42	3.7E-02	3.4E-02	1.1E-03
48	3.5E-02	3.3E-02	1.1E-03
54	3.4E-02	3.2E-02	1.1E-03
60	3.3E-02	3.0E-02	1.1E-03
65	3.1E-02	2.9E-02	1.0E-03
72	2.6E-02	2.4E-02	8.8E-04
80	6.5E-03	5.2E-03	2.3E-04
90	0.	0.	0.

TABLE 2 REFLECTION DISTRIBUTION FUNCTIONS

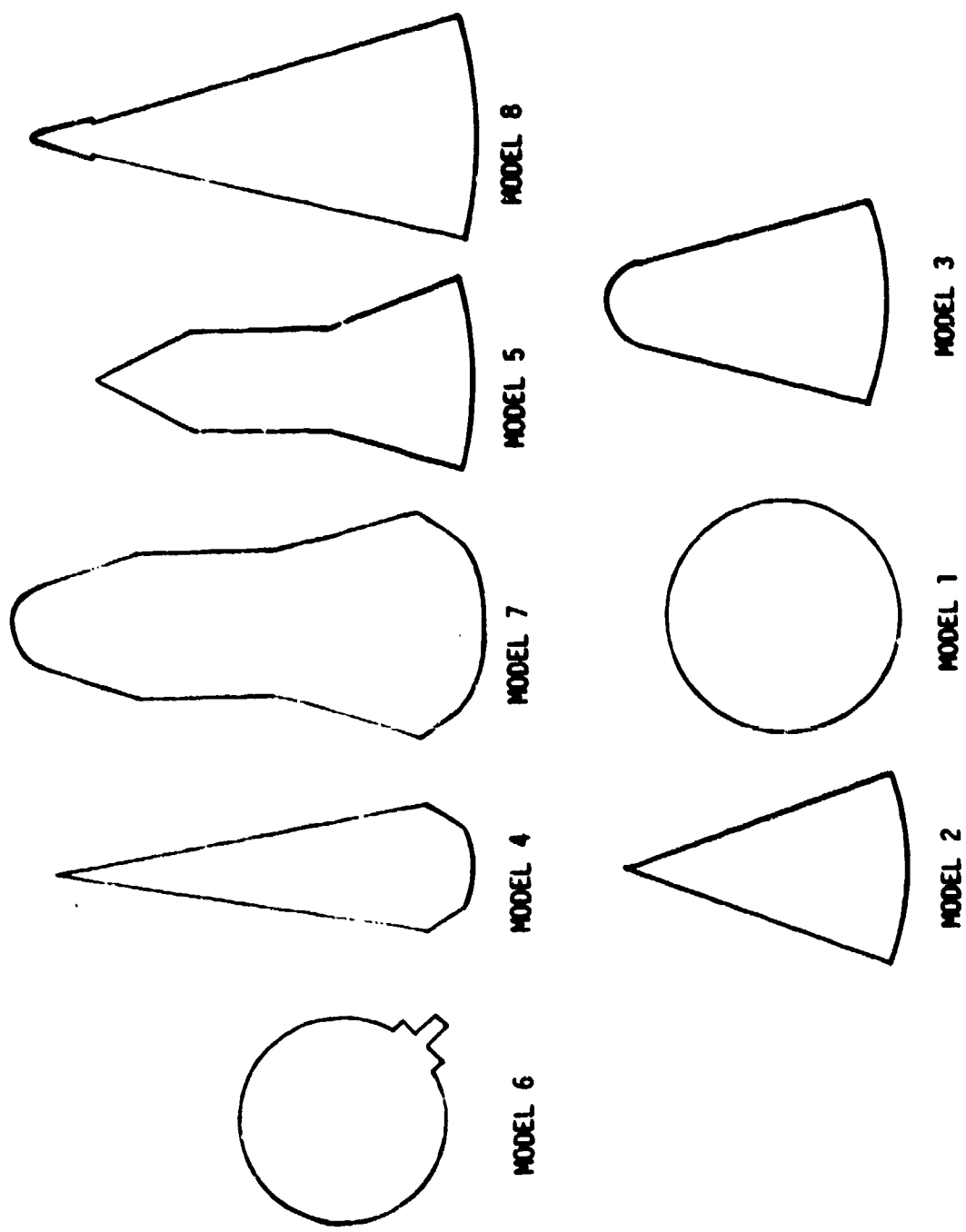
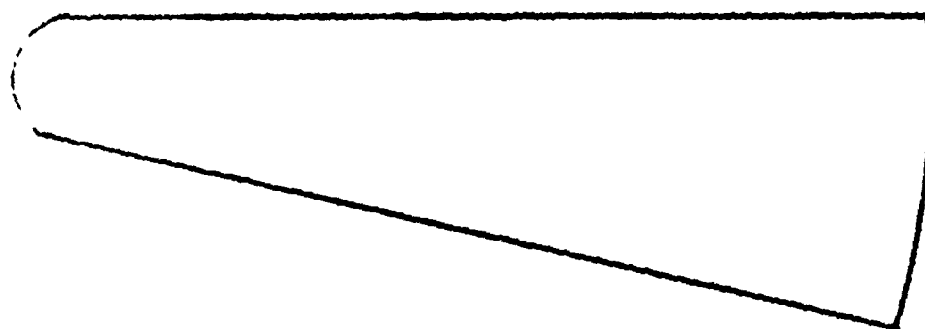
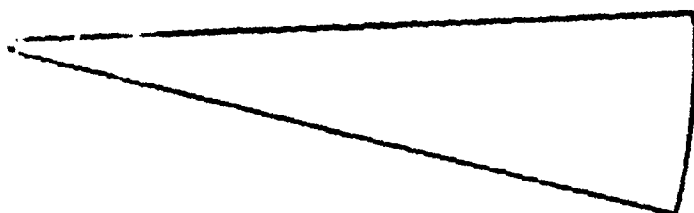


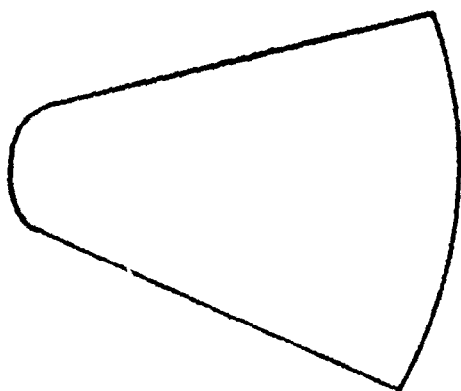
FIGURE 11-1 DRAWINGS OF MICOM MODELS



MODEL Z



MODEL DECOY



MODEL X-1

FIGURE 11-2 DRAWINGS OF ADDITIONAL MODELS

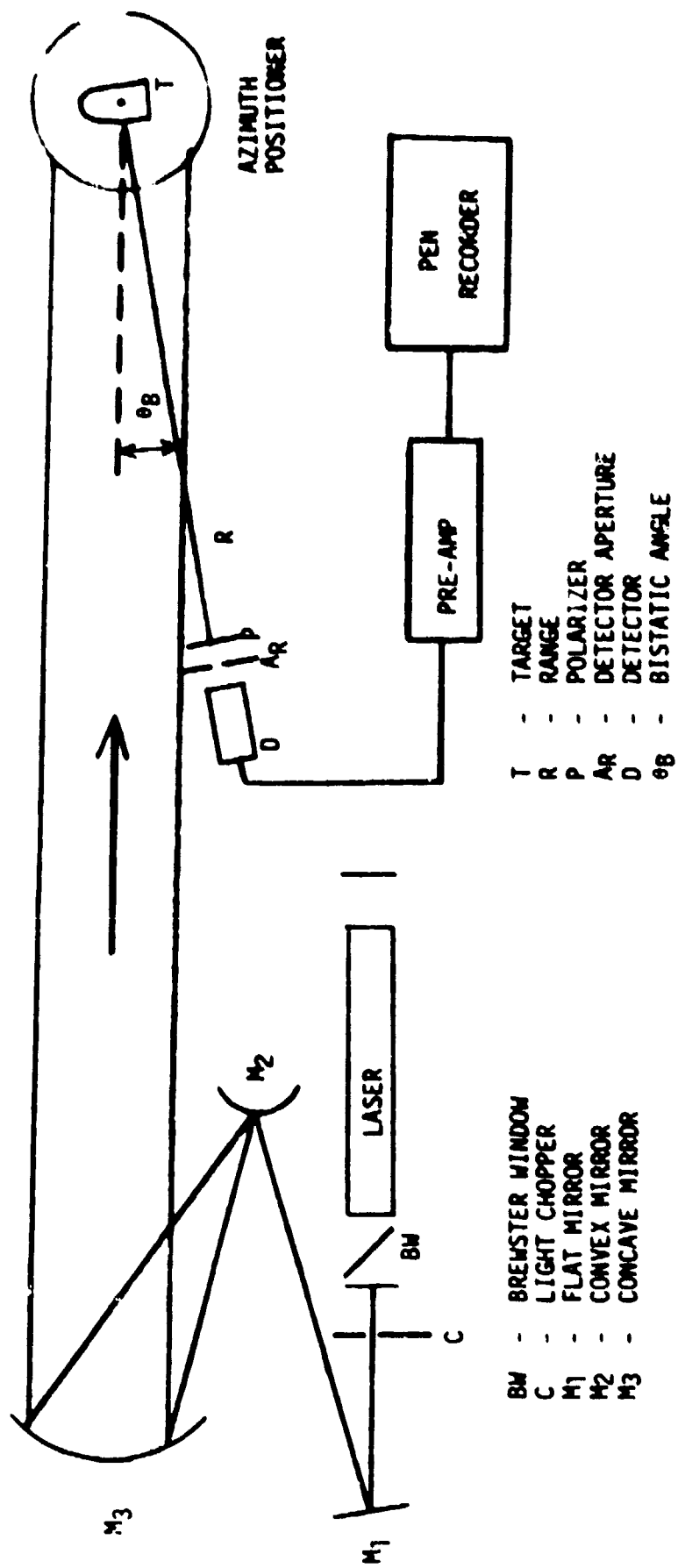
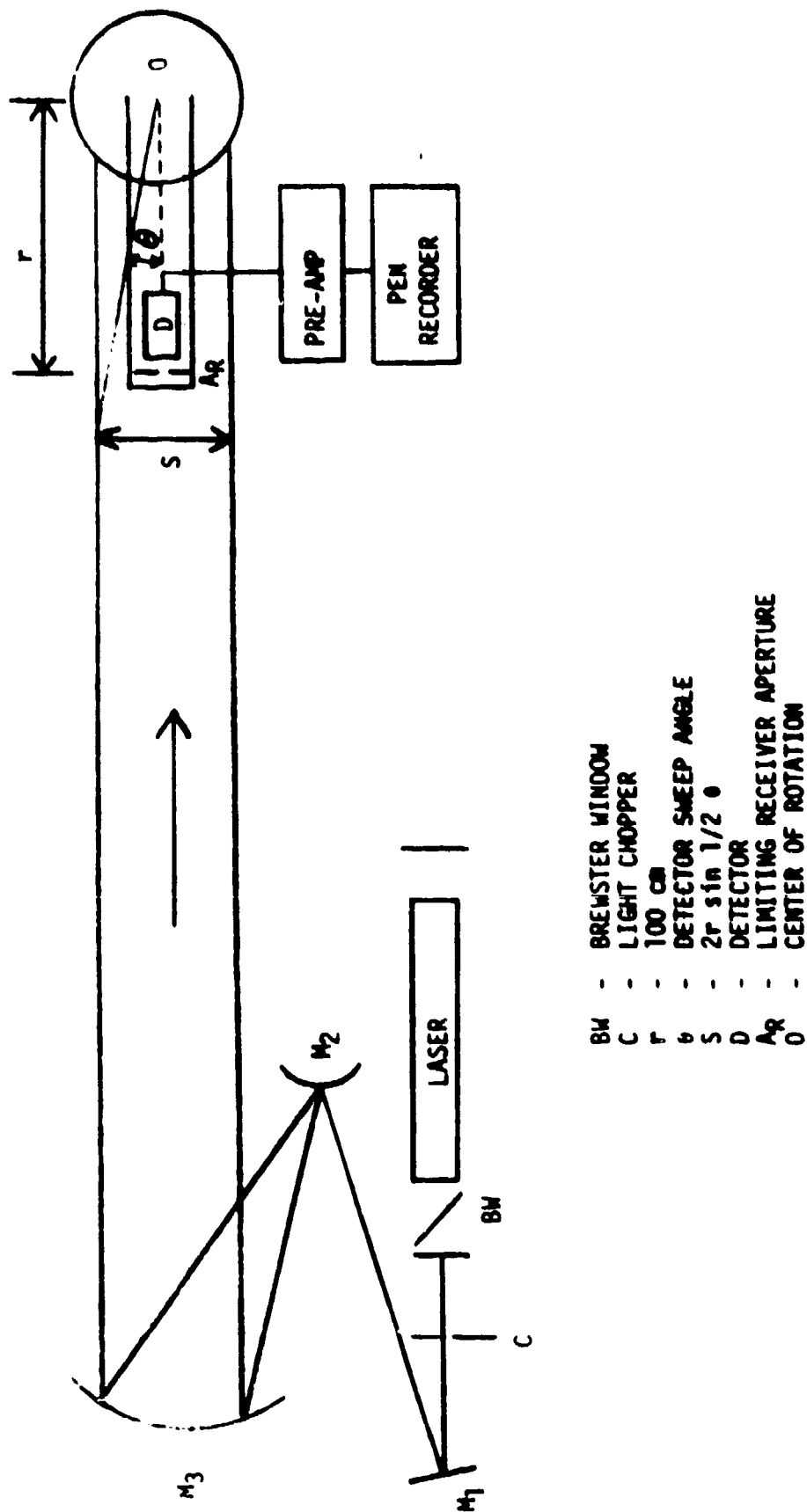


FIGURE IV-1 TARGET BACKSCATTER MEASUREMENT APPARATUS



BW - BREWSTER WINDOW
 C - LIGHT CHOPPER
 r - 100 CM
 θ - DETECTOR SWEEP ANGLE
 S - $2r \sin \frac{1}{2} \theta$
 D - DETECTOR
 A_R - LIMITING RECEIVER APERTURE
 O - CENTER OF ROTATION

FIGURE IV-2 BEAM PROFILE MEASUREMENT APPARATUS

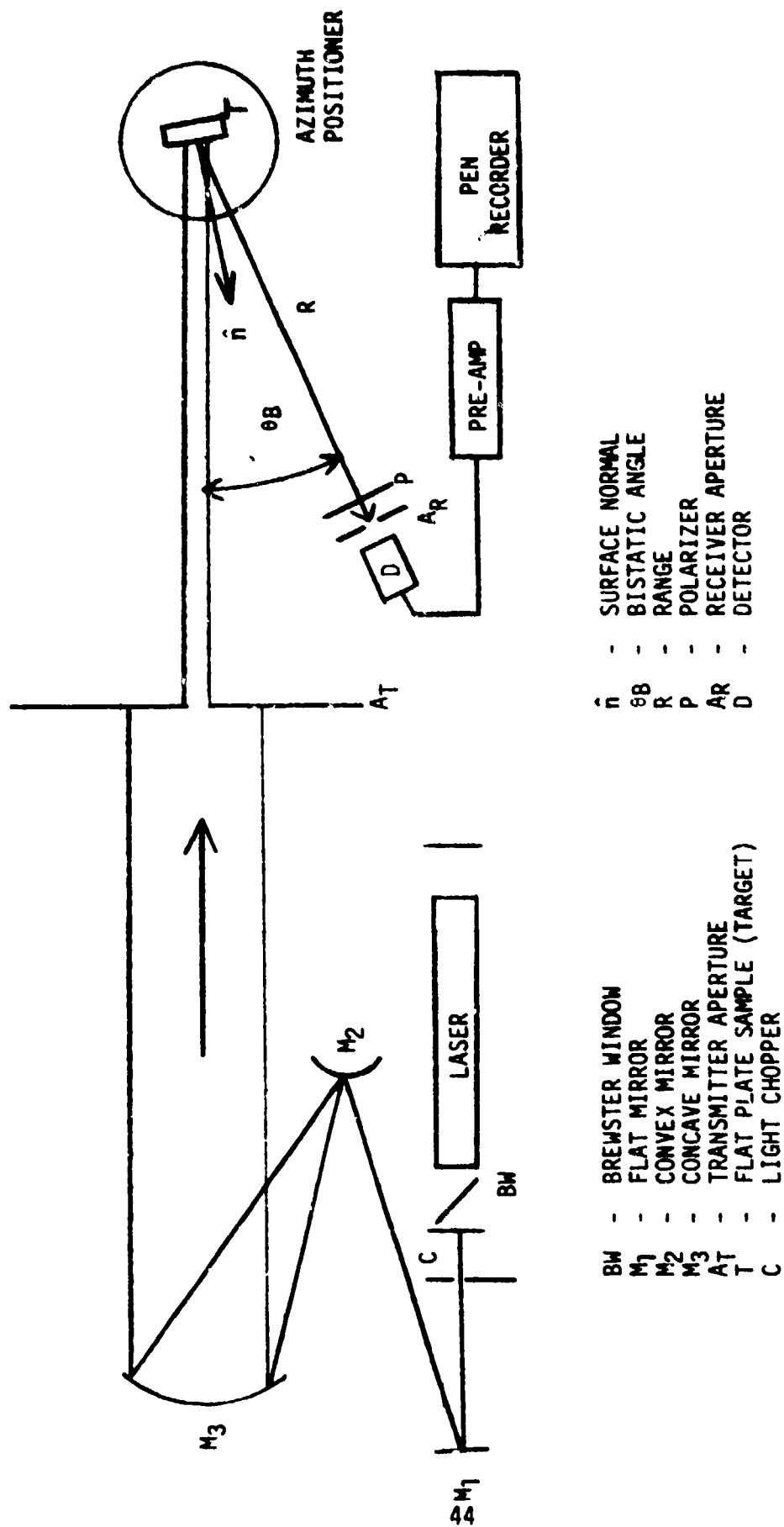


FIGURE IV-3 FLAT PLATE BACKSCATTER ARRANGEMENT

PATTERN NO. 4 11/5/74

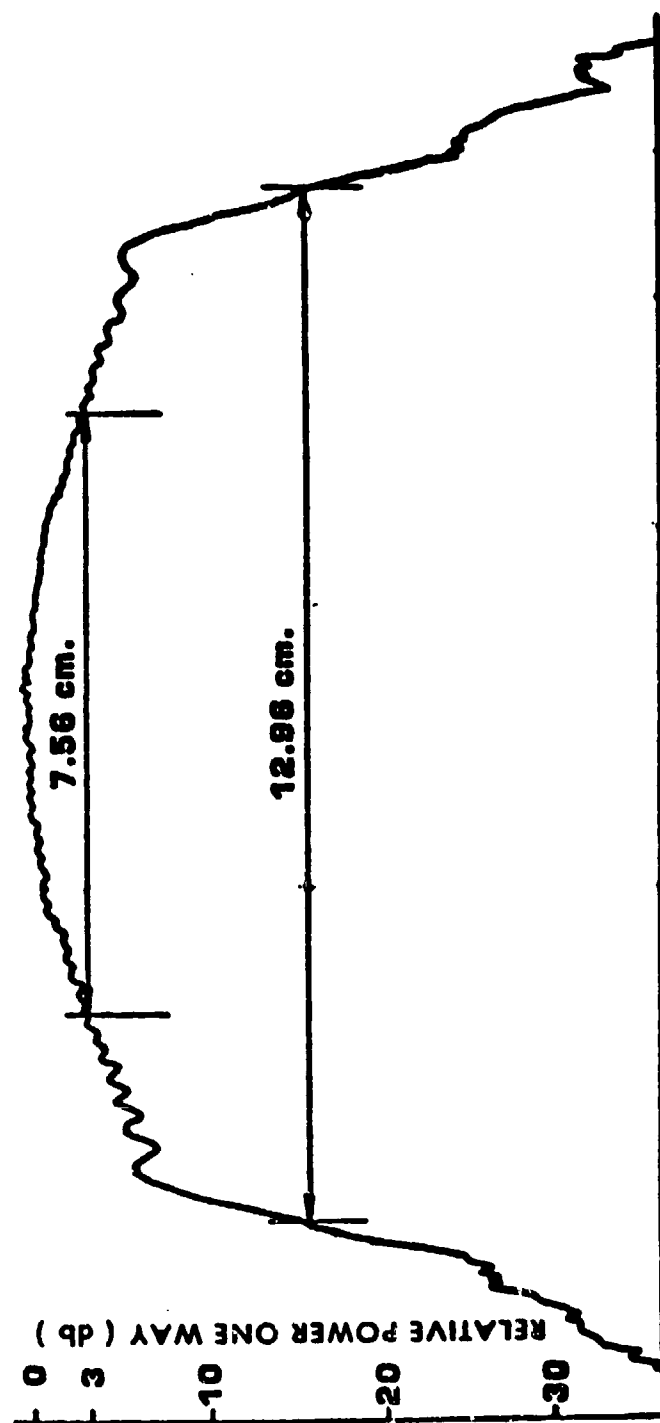
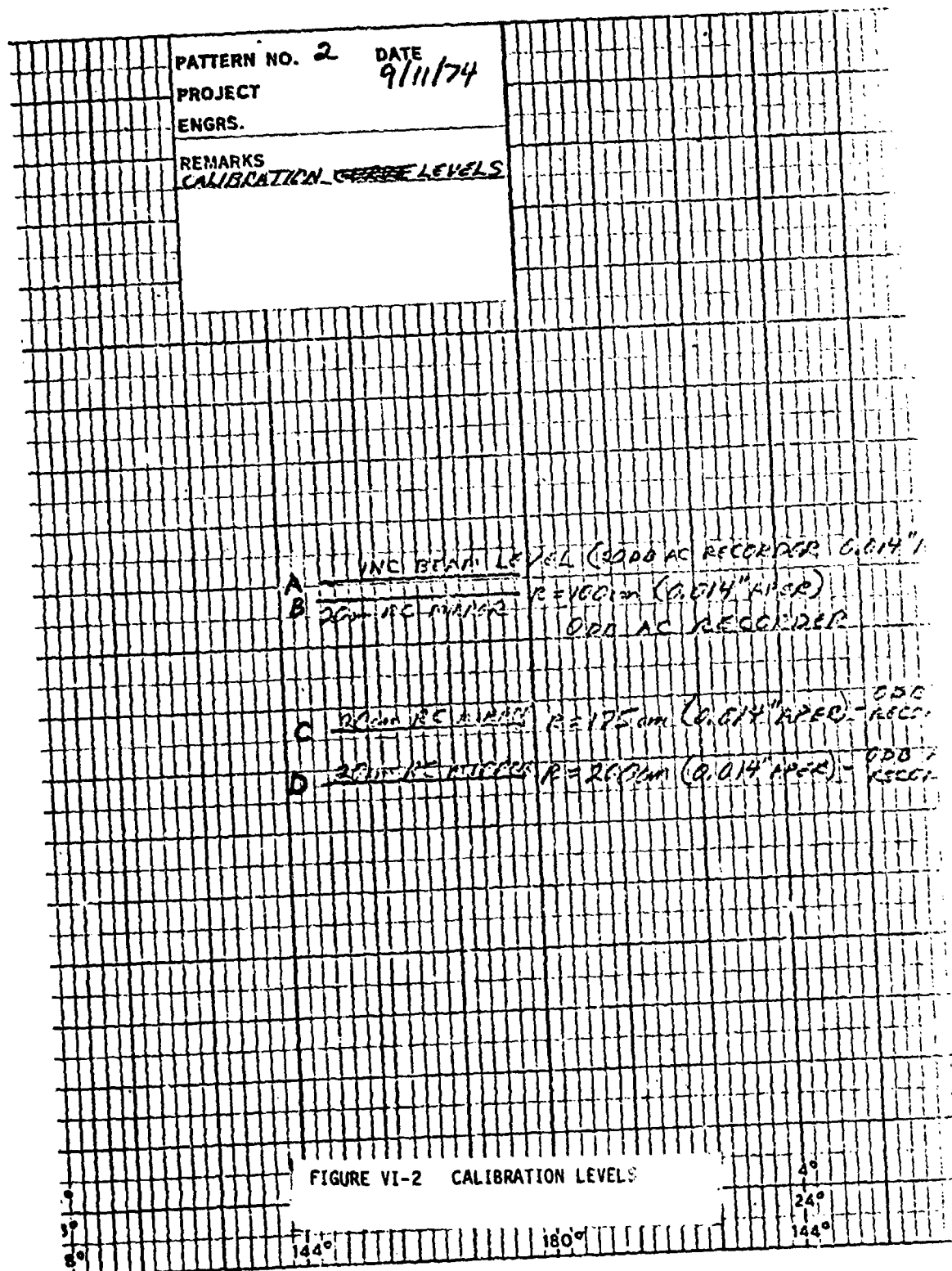


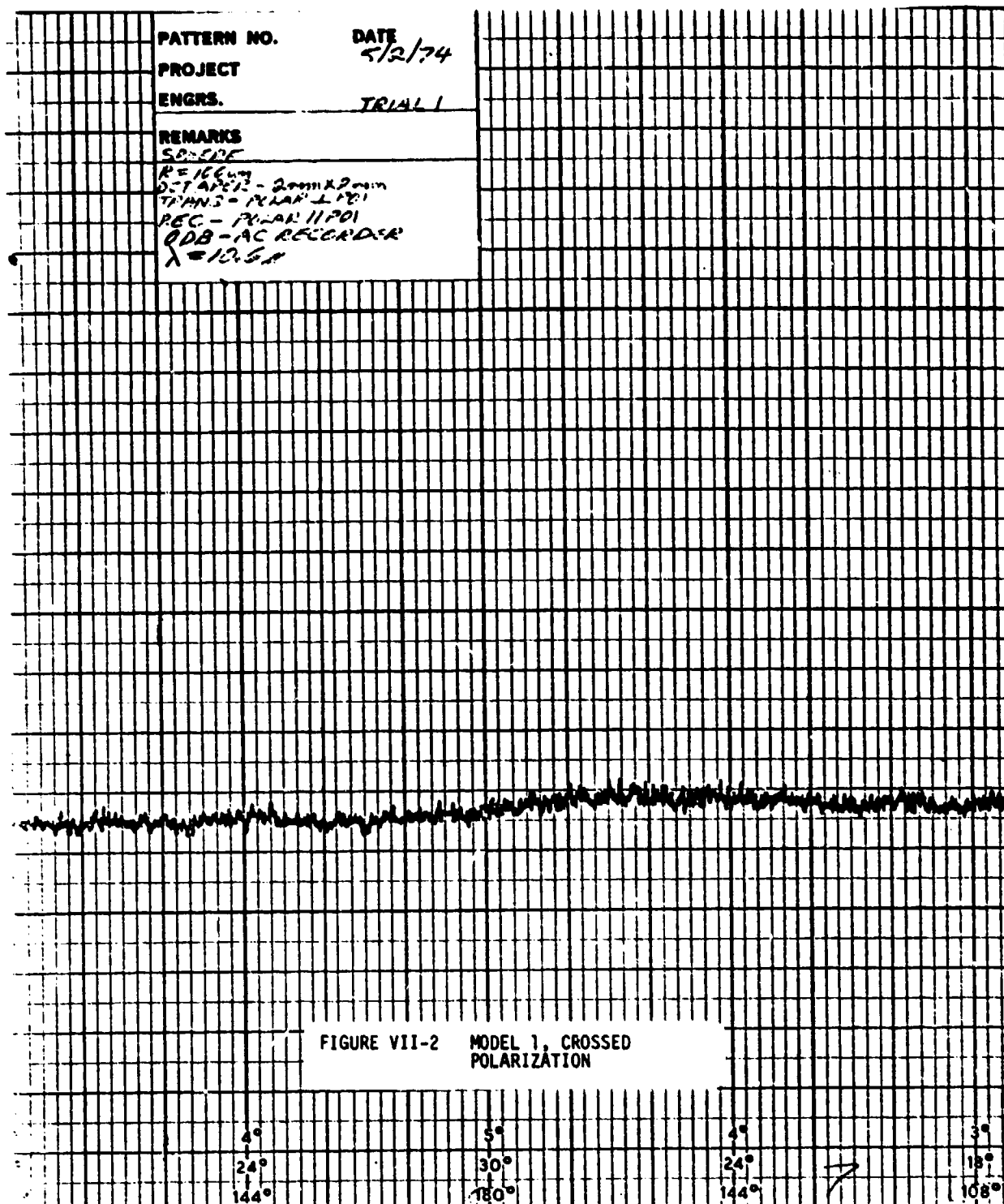
FIGURE VI-1 (U) INCIDENT BEAM PROFILE (U)



PATTERN NO. DATE
 PROJECT 5/21/74
 ENGRS. TRIAL 1
 REMARKS
 SUPER
 REF AREA = 2mm x 2mm
 TRANS - POLARIZER
 REF - POLARIZER
 REF - ANALYZER

FIGURE VII-1 MODEL 1, UNCROSSED POLARIZATION

3°	5°	4°	3°
24°	30°	24°	18°
144°	180°	144°	106°



PATTERN NO. DATE
 PROJECT 5/2/74
 ENGRS. TRIAL 2

REMARKS
 SENSE
 REF. 100
 NET A - 5.014" DIAM
 TRAN - POLAR 1 POI
 REC - POLAR 1 POI
 2-B-AC RECORDER
 X - 12.5"

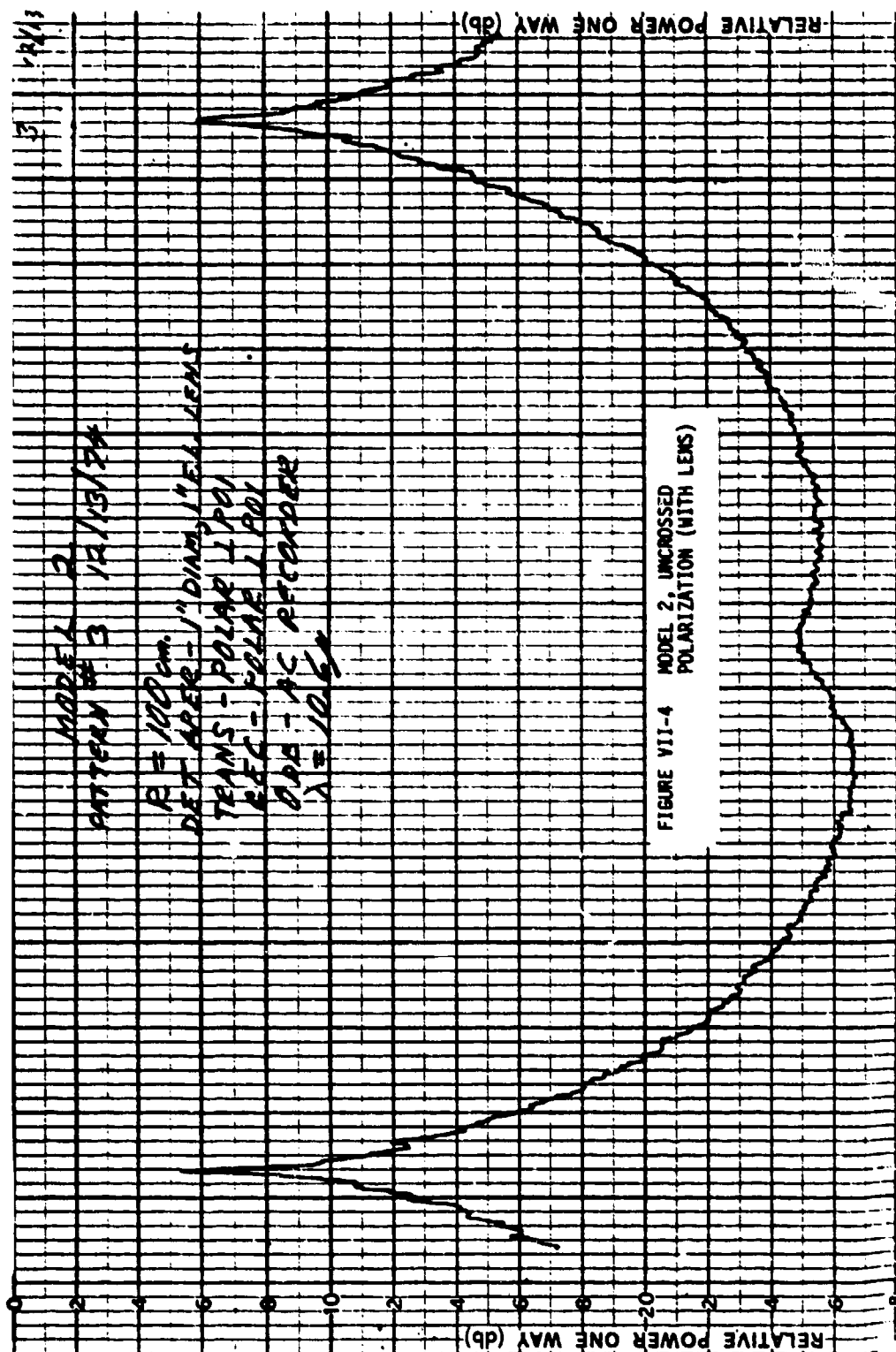
FIGURE VII-3 MODEL 1, UNCROSSED
 POLARIZATION, SMALL
 RECEIVER

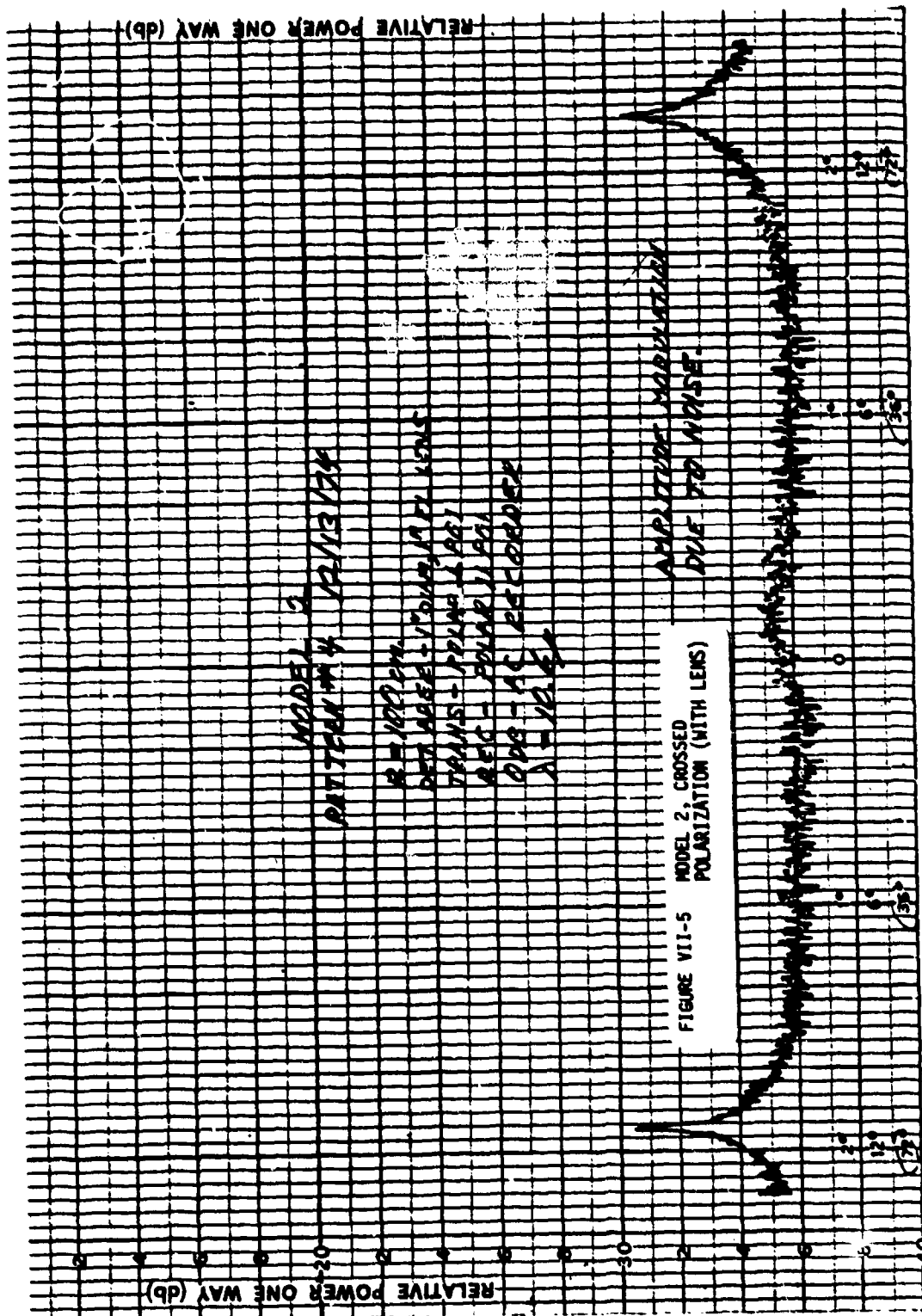
4°
 24°
 144°

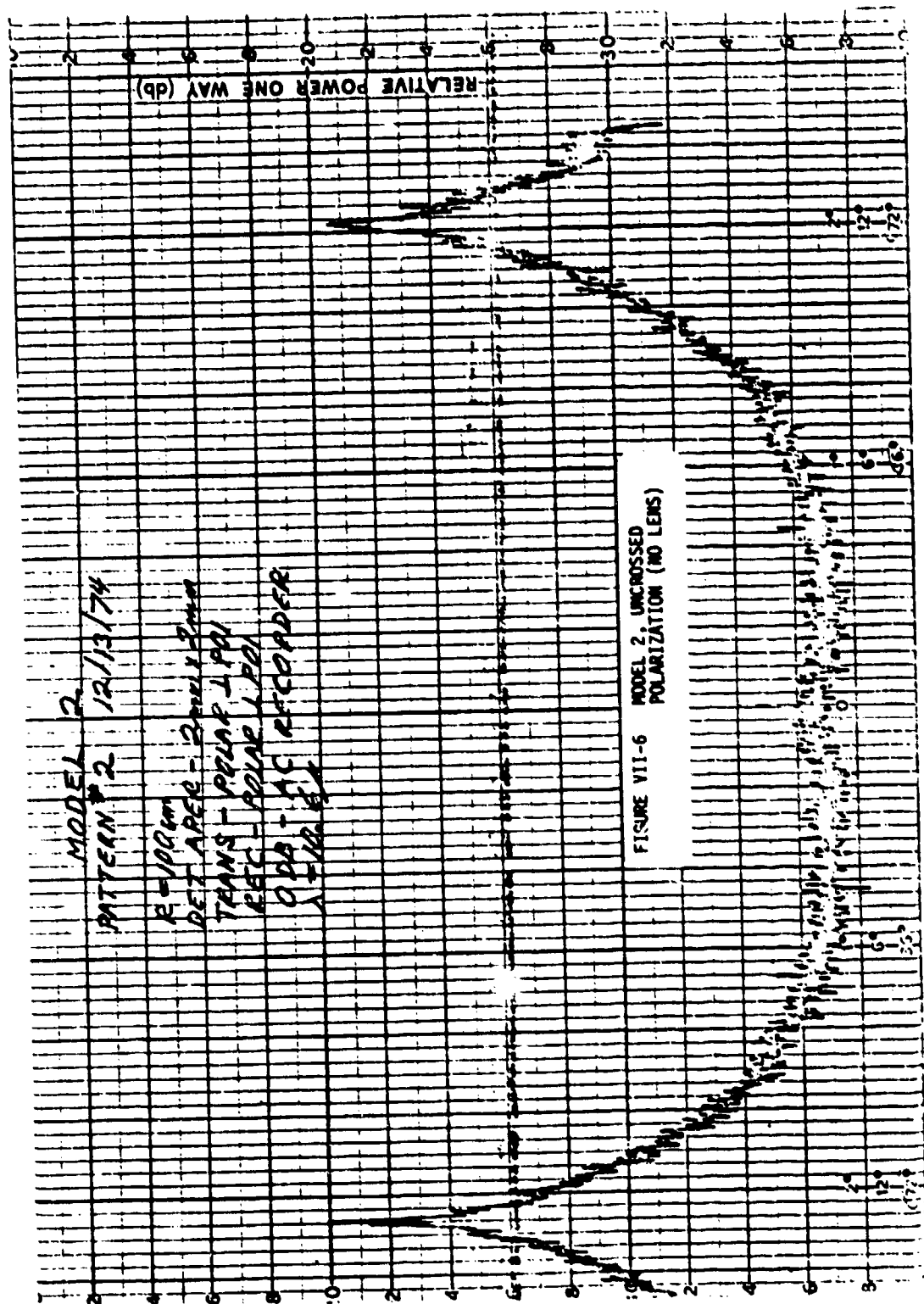
5°
 30°
 (180°)

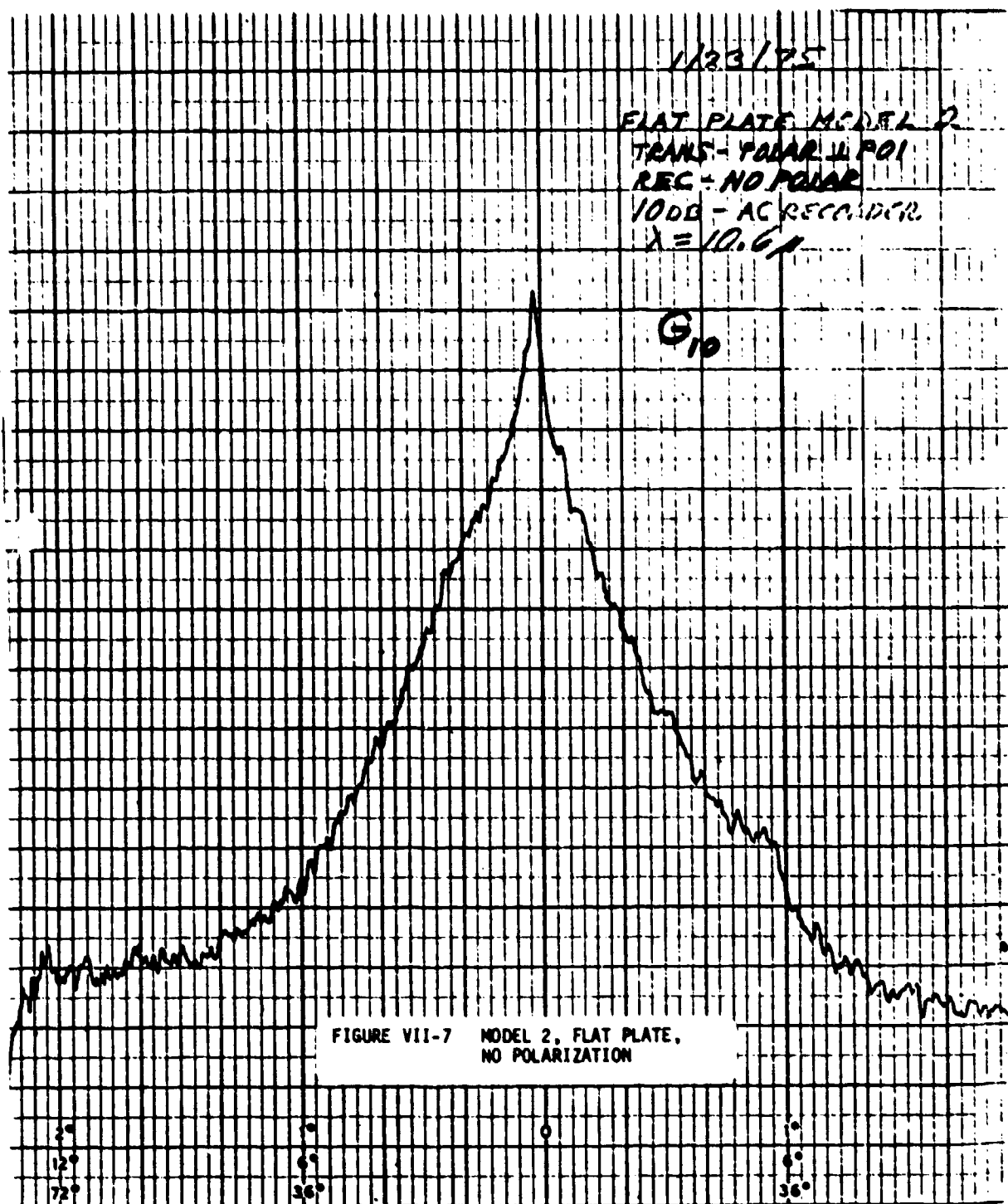
4°
 24°
 144°

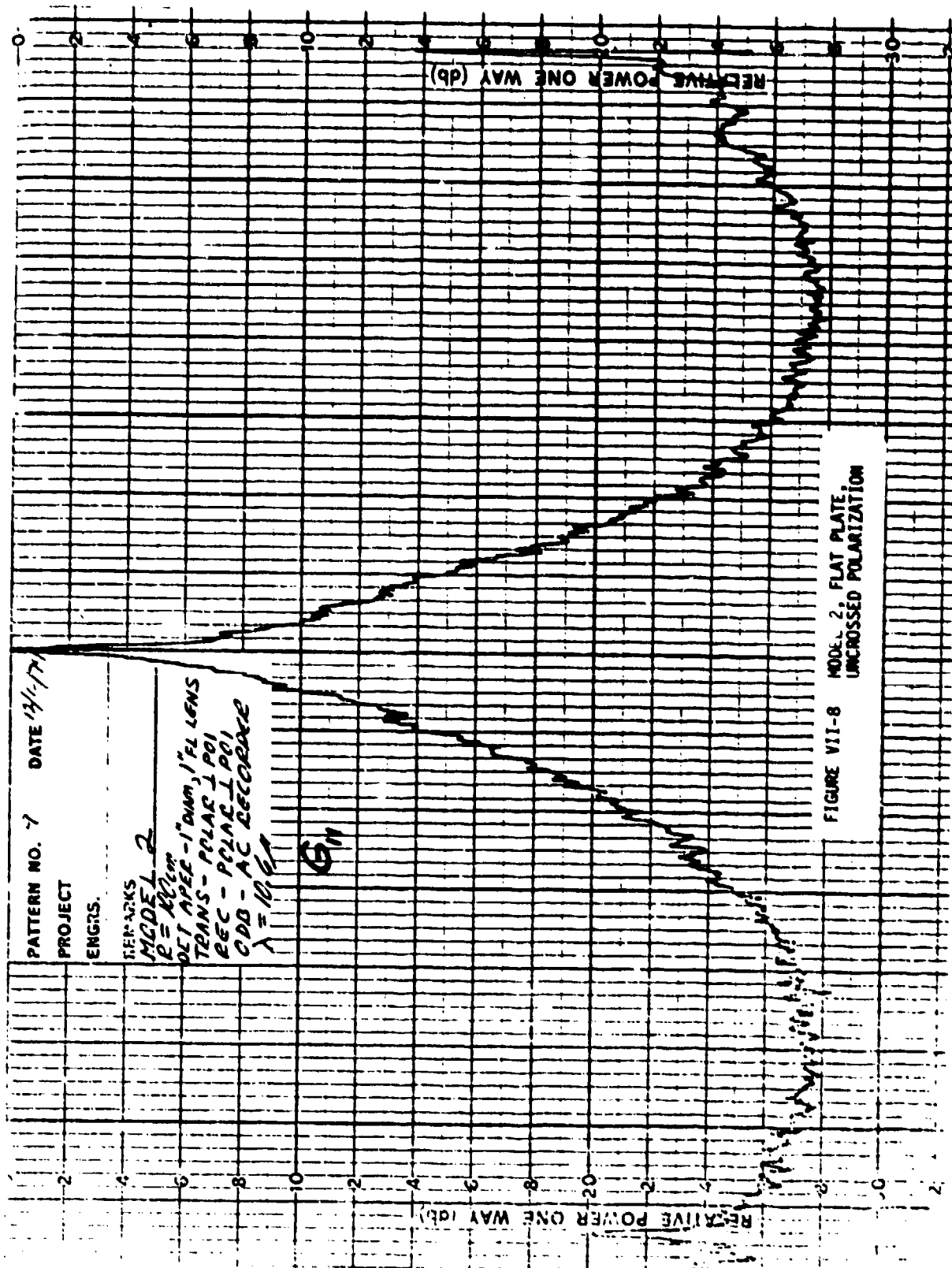
3°
 15°
 (108°)

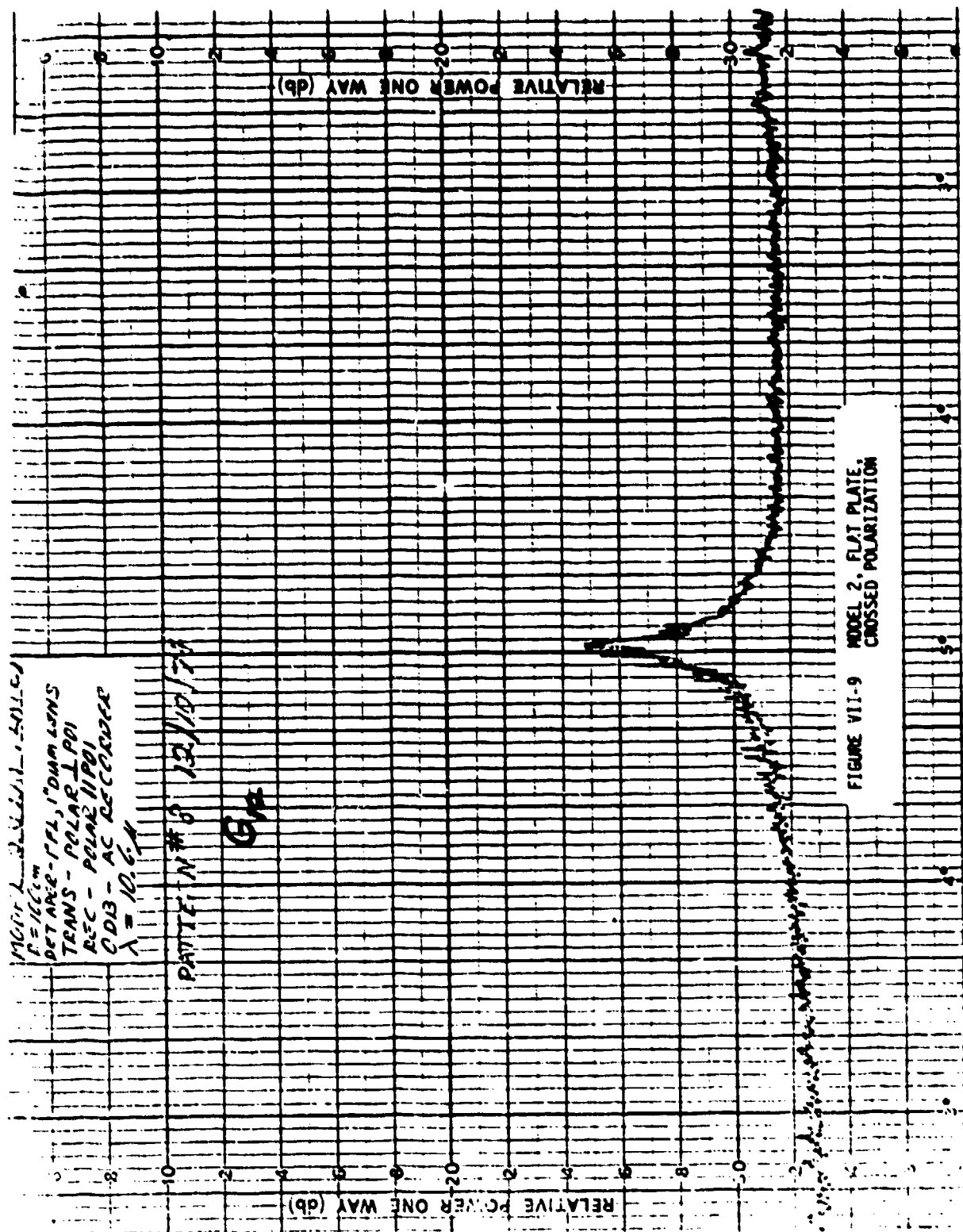


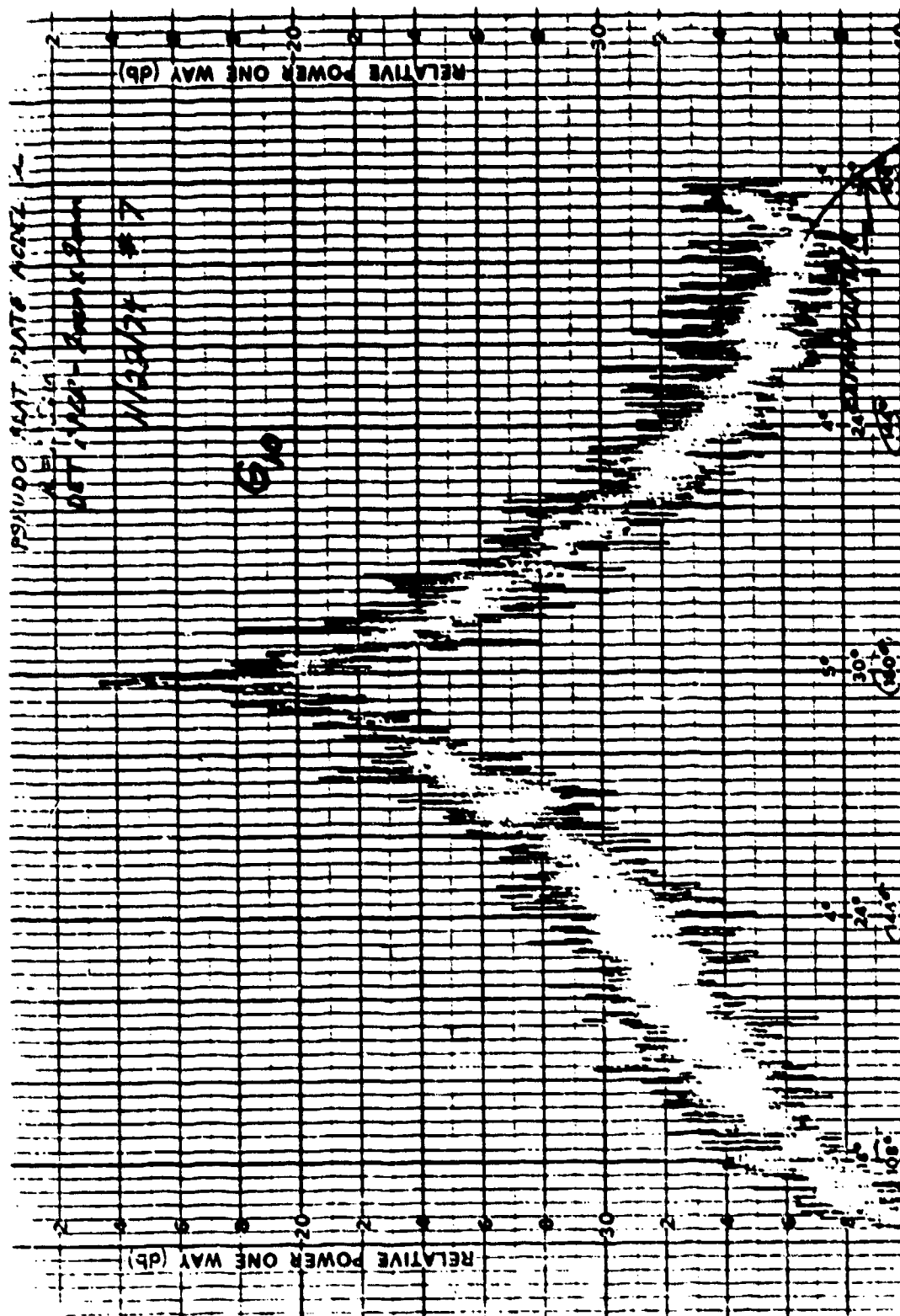












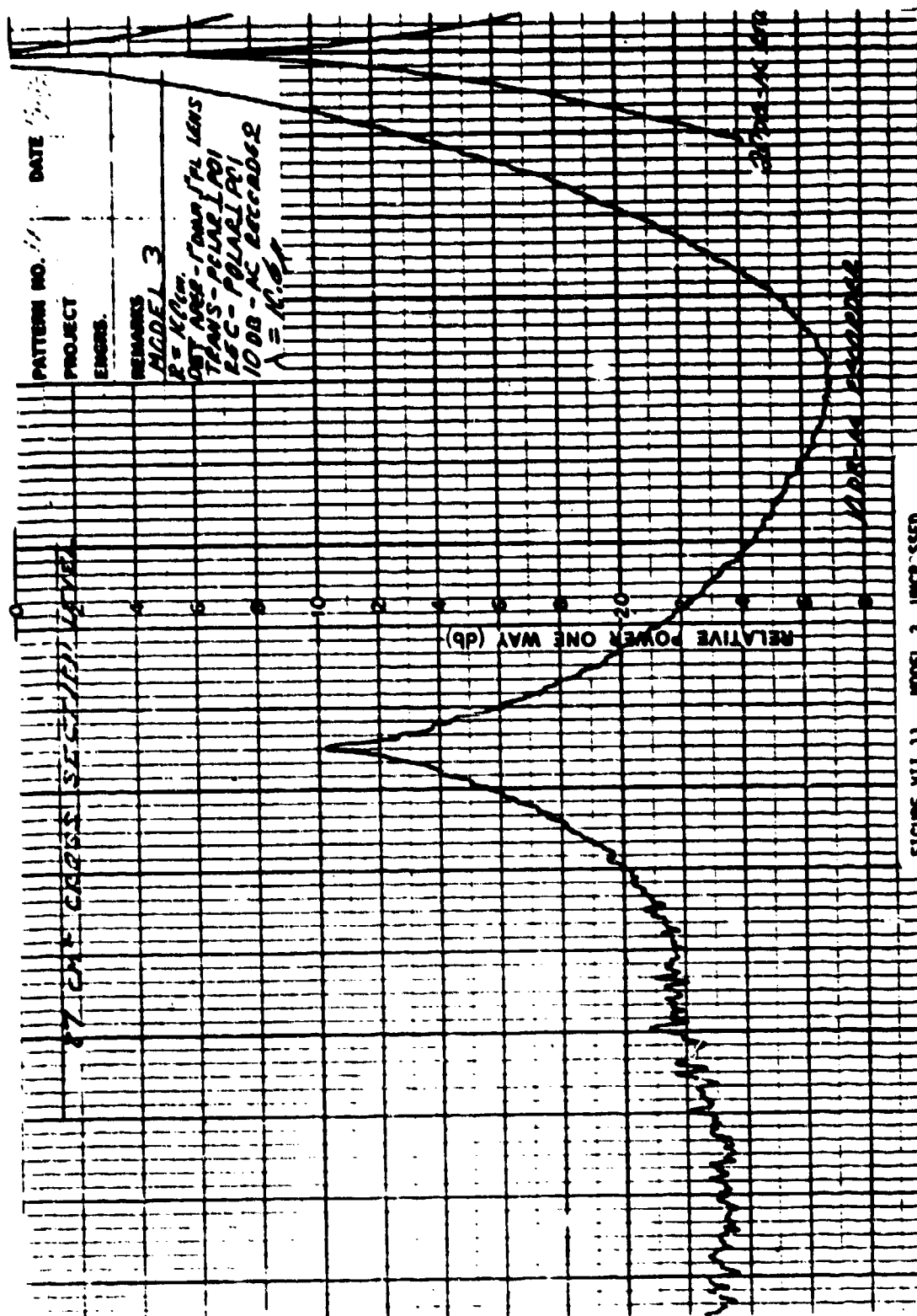


FIGURE VII-11 MODEL 3, UNCROSSSED POLARIZATION (WITH LENS)

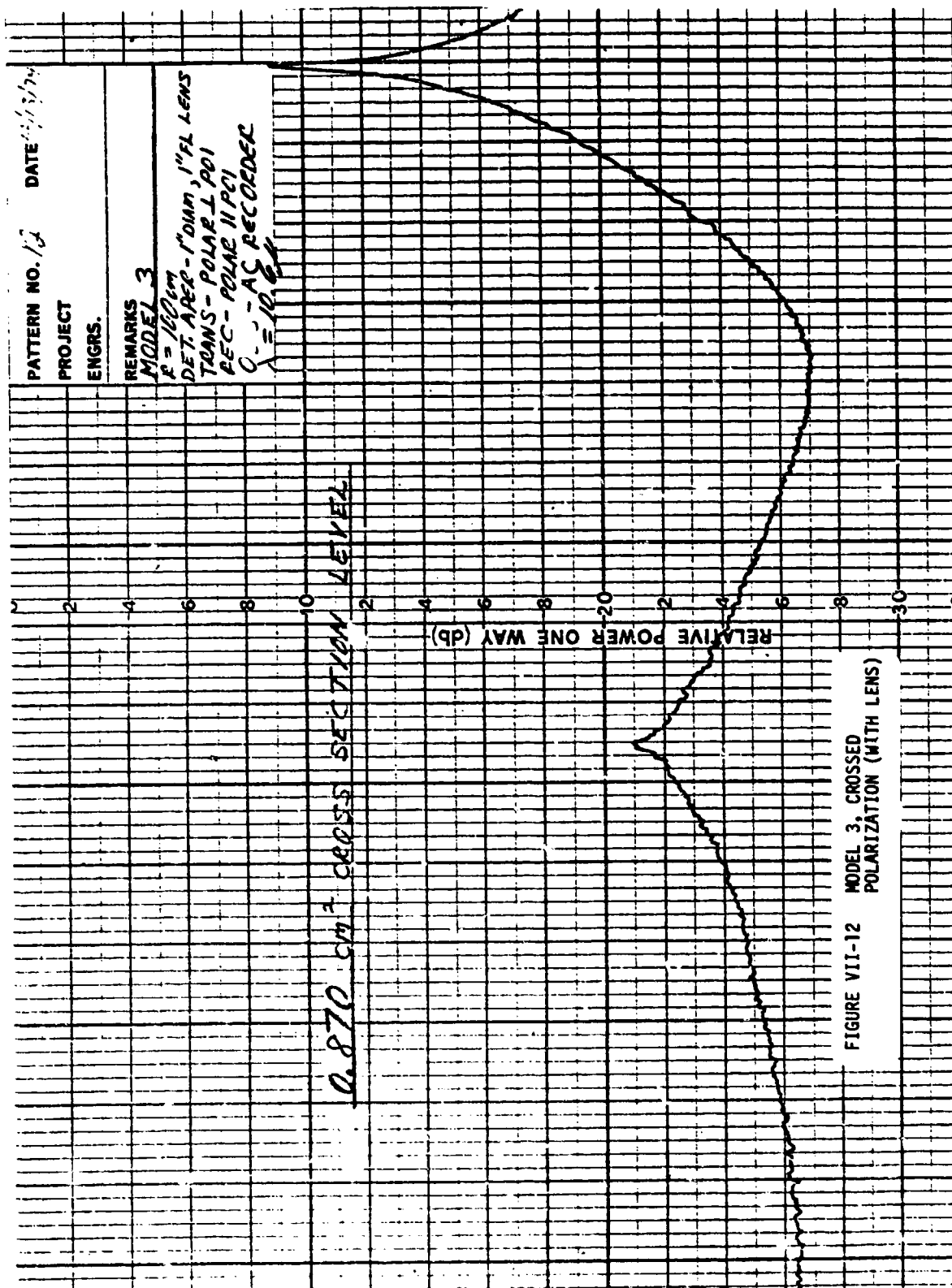


FIGURE VII-12 MODEL 3, CROSSED POLARIZATION (WITH LENS)

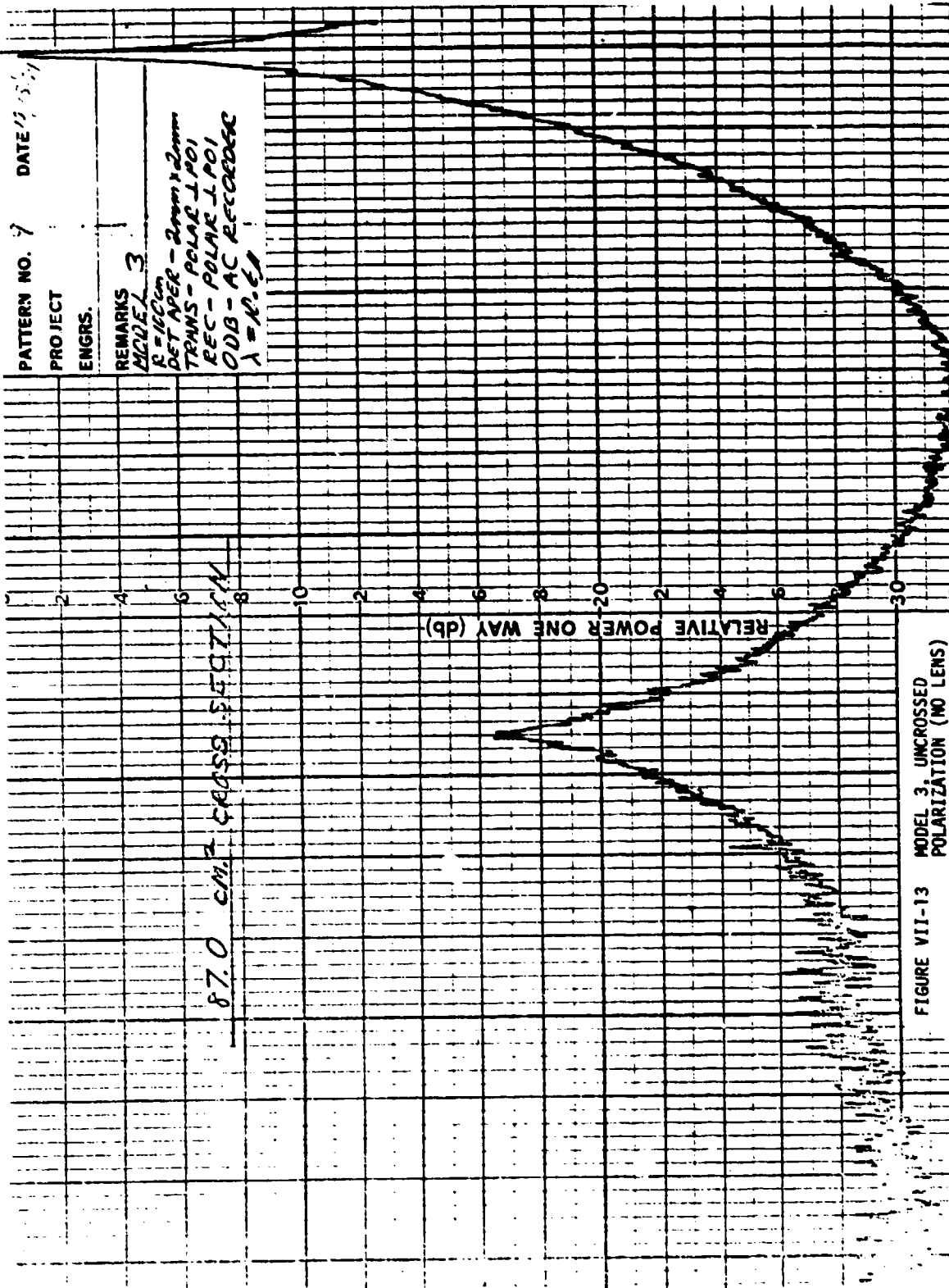
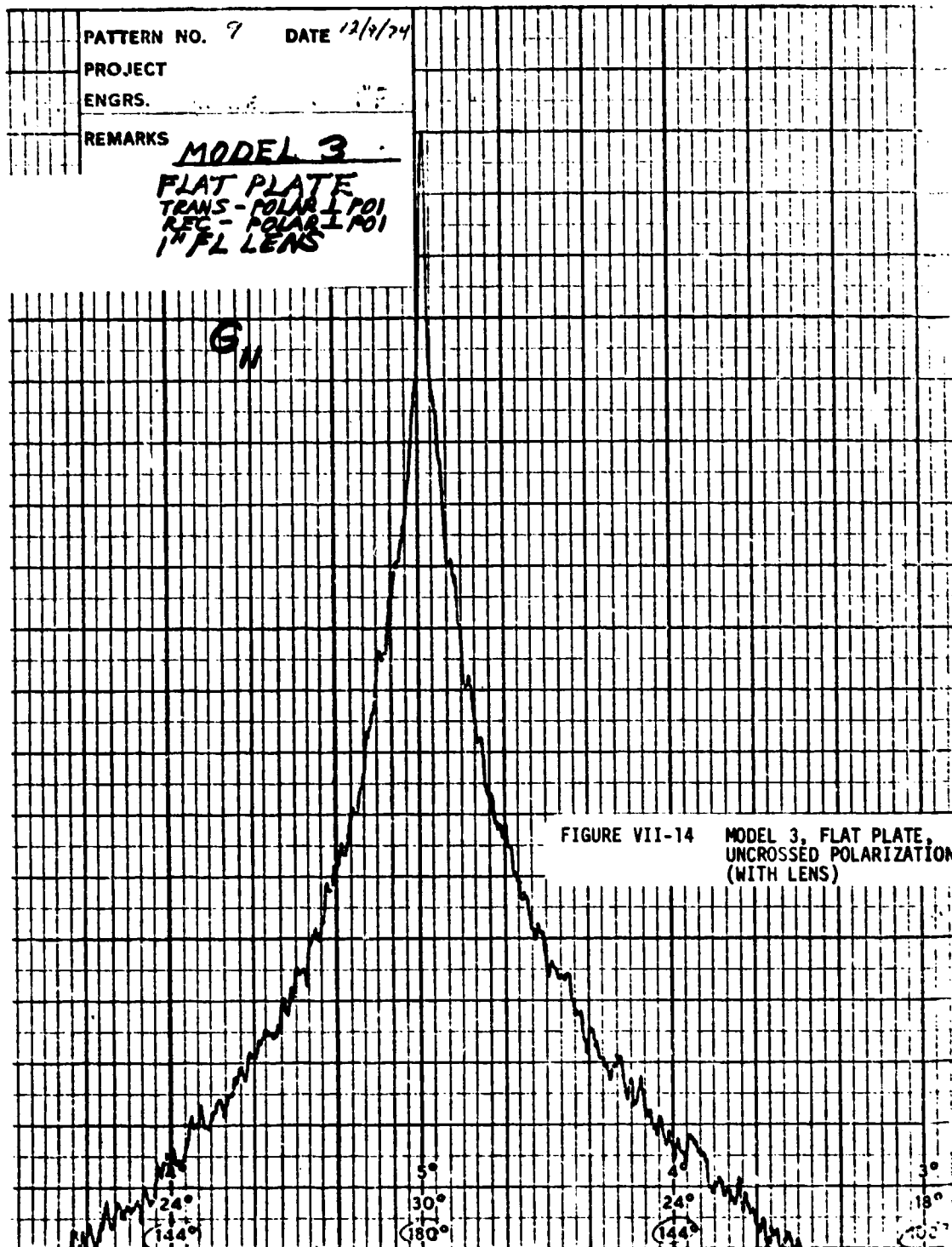


FIGURE VII-13 MODEL 3, UNCROSSED POLARIZATION (NO LENS)



PATTERN NO. 8 DATE 12/9/74

PROJECT

ENGRS.

REMARKS

MODEL 3
FLAT PLATE
TRANS - POLAR 1 POI
REC - POLAR 11 POI
1" FL LENS

G₁₂

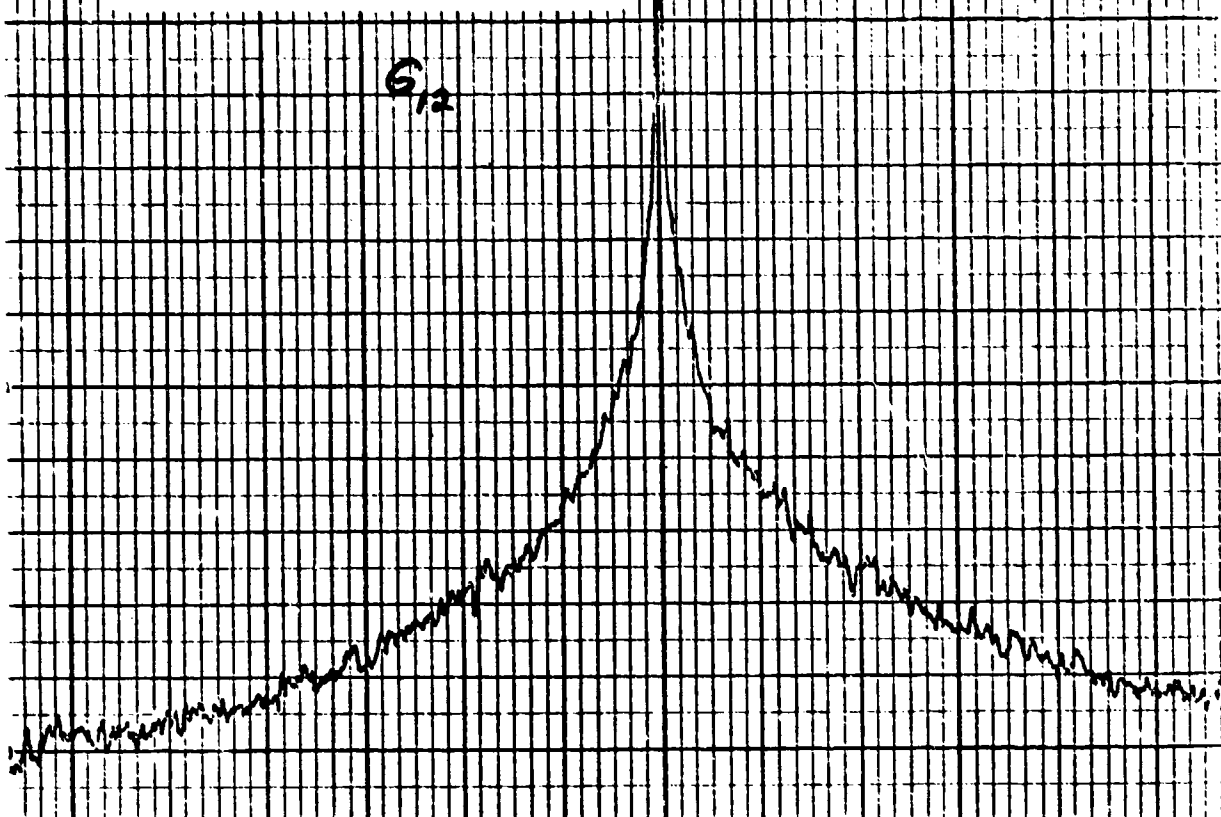


FIGURE VII-15 MODEL 3. FLAT PLATE
CROSSED POLARIZATION
(WITH LENS)

3°
18°
108°

4°
24°
144°

5°
30°
180°

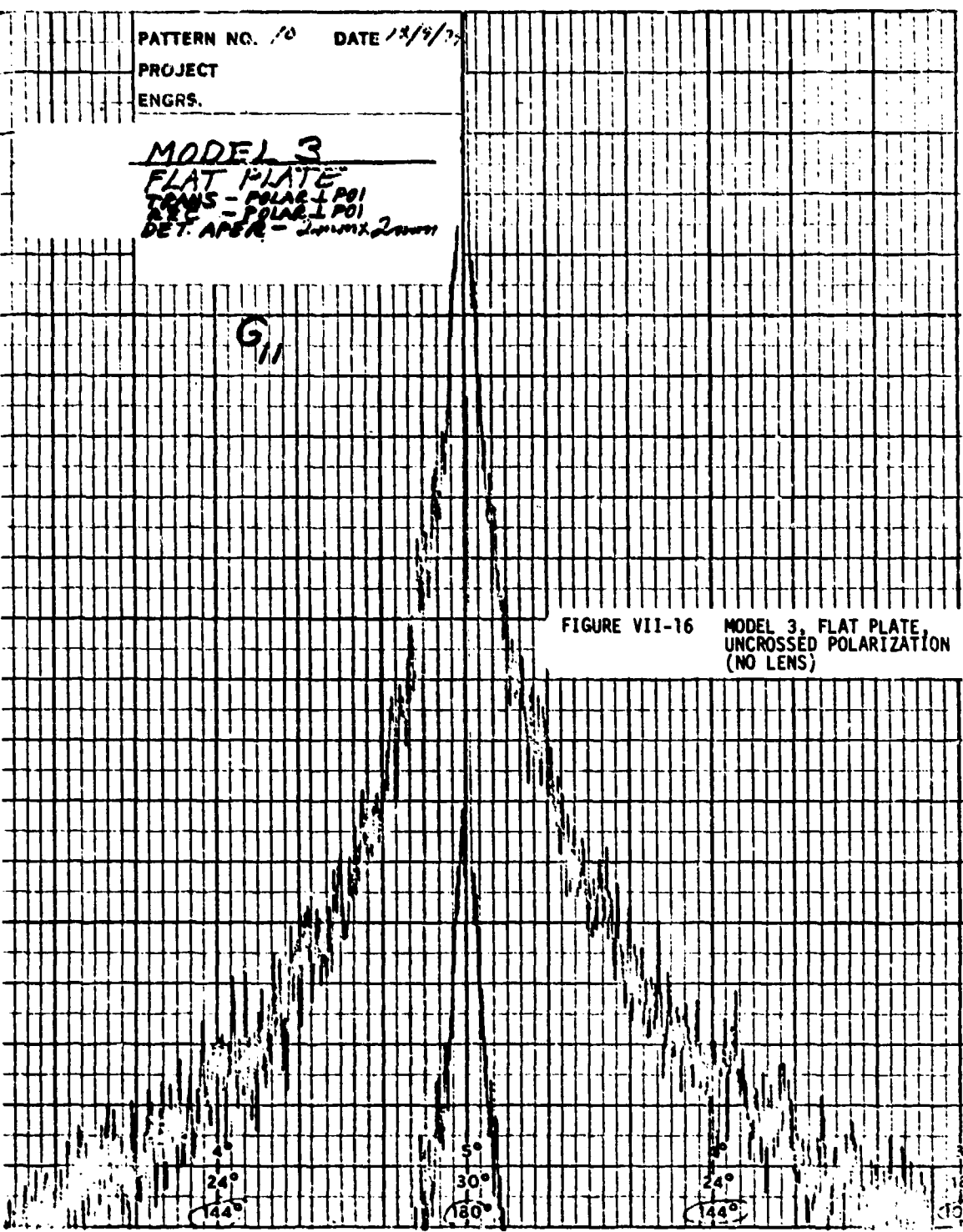
4°
24°
144°

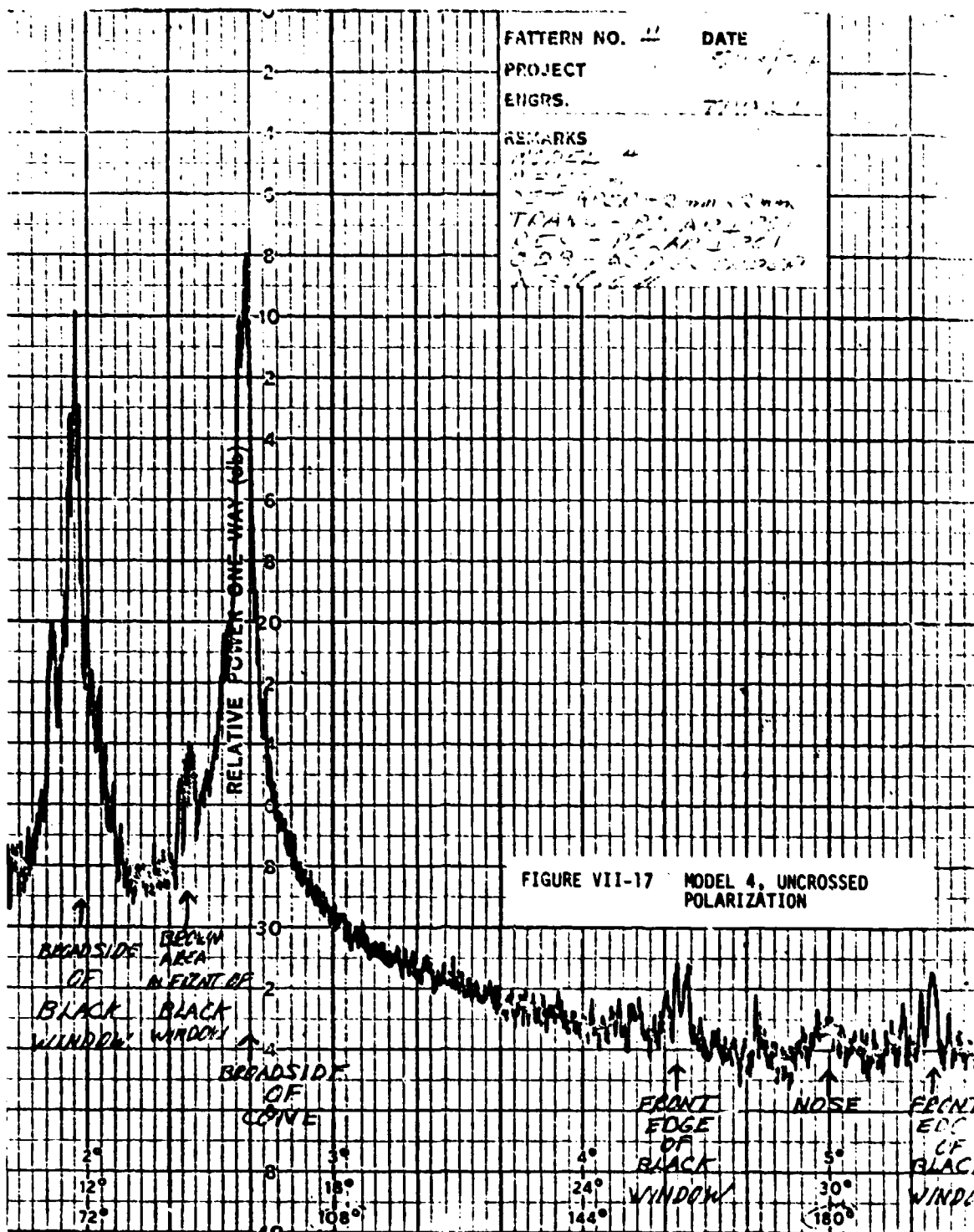
PATTERN NO. 10 DATE 12/9/77
PROJECT
ENGRS.

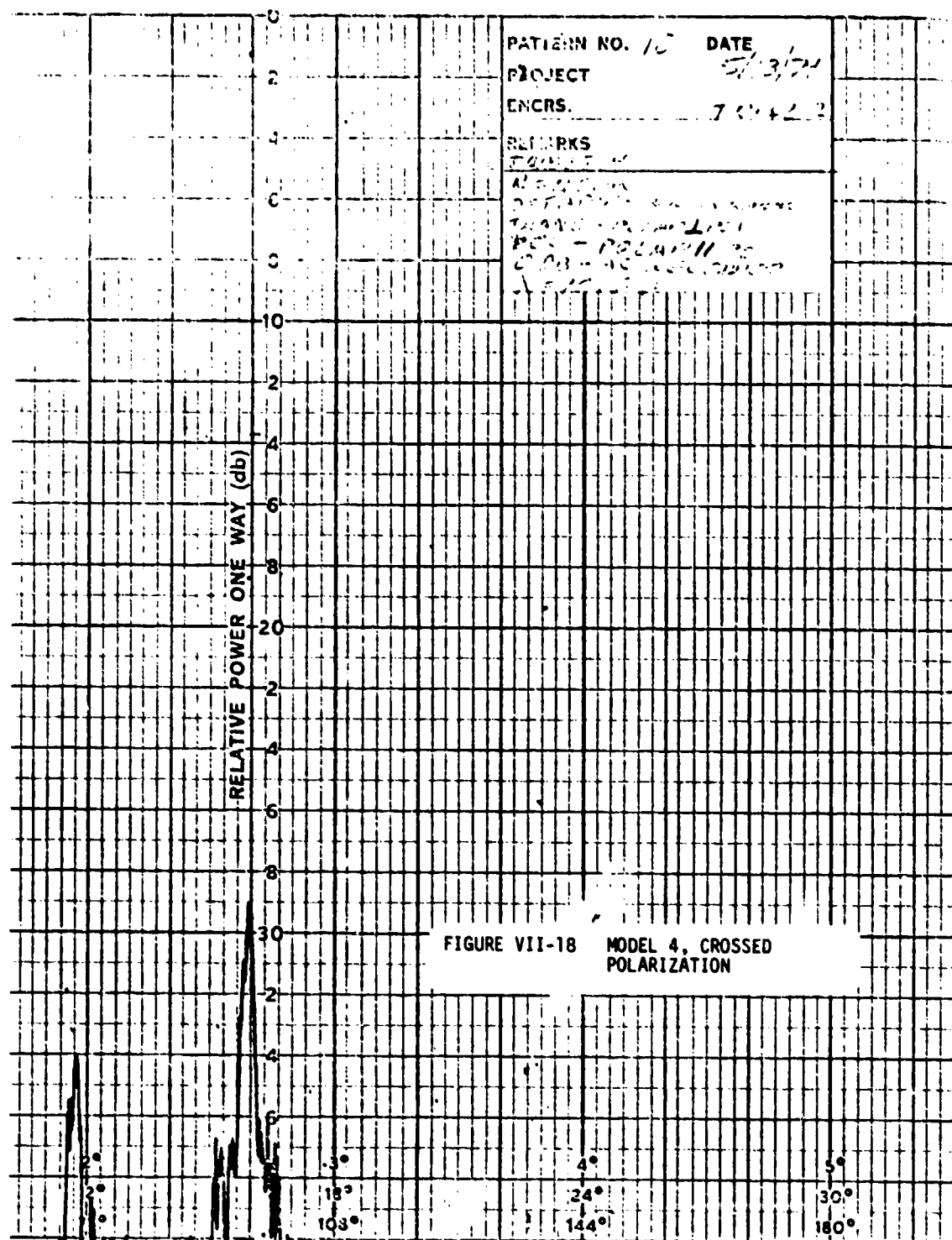
MODEL 3
FLAT PLATE
TRANS - POLAR. I POI
REF - POLAR. I POI
DET. APERT - 2mm x 2mm

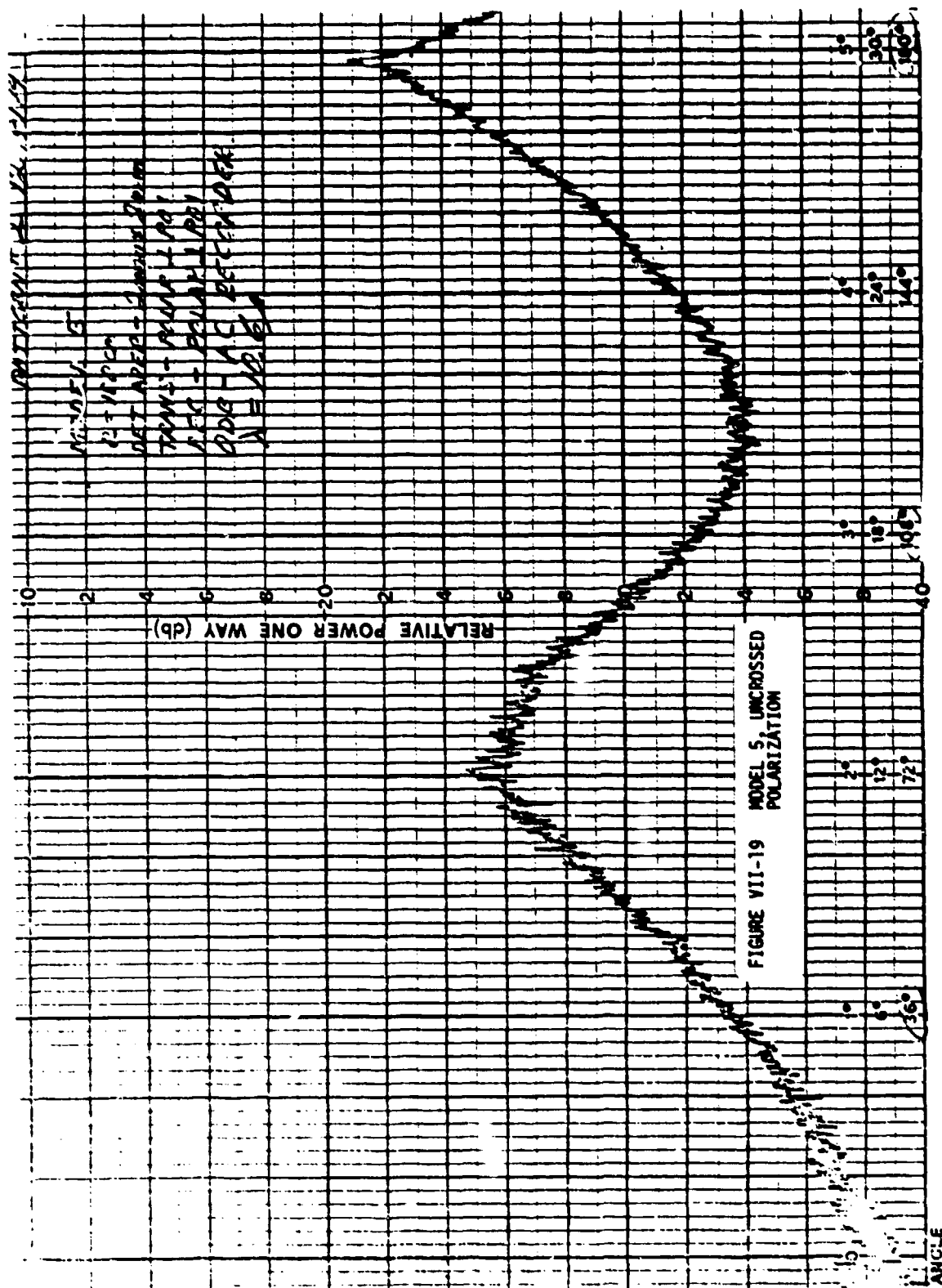
G
11

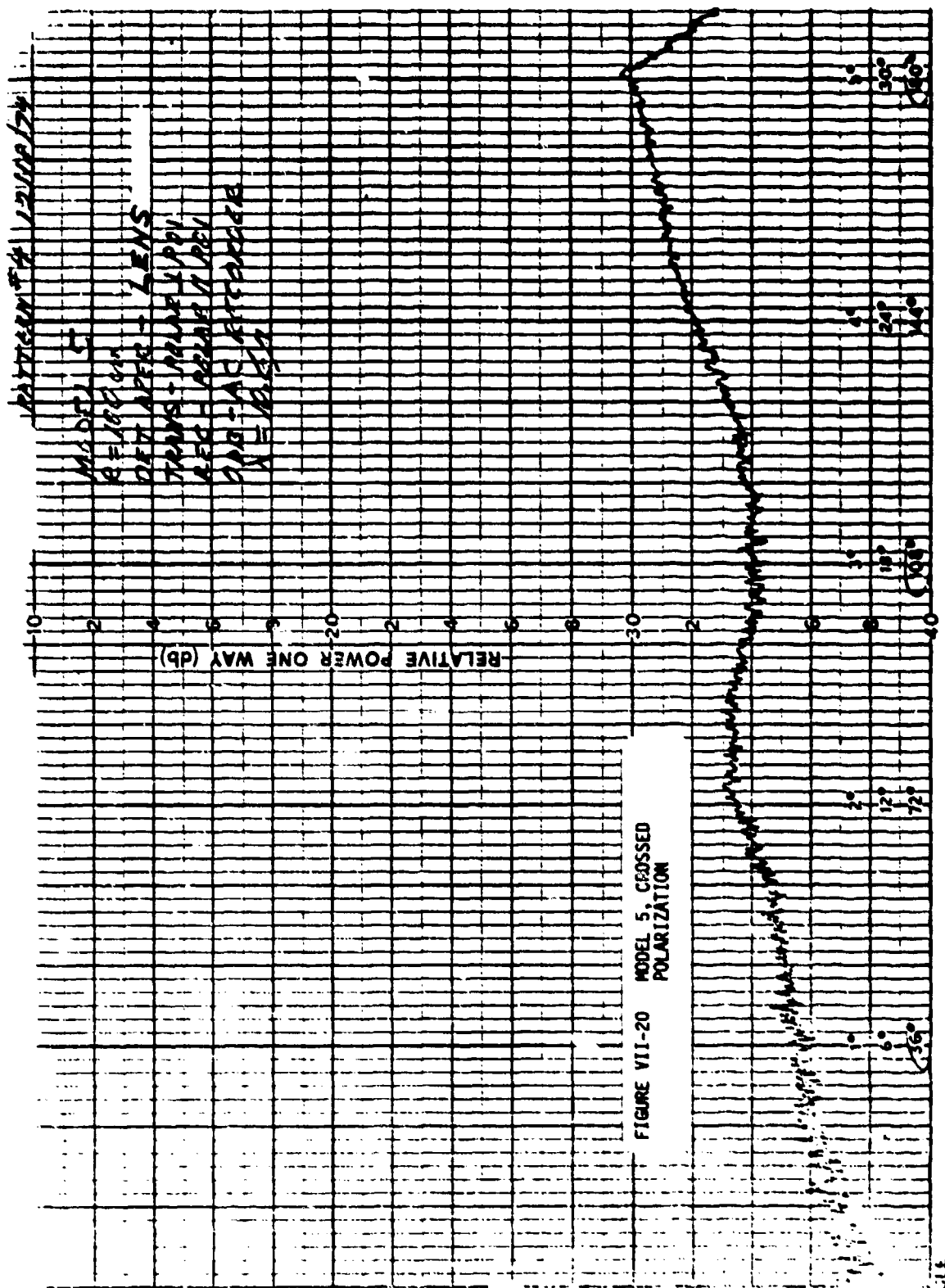
FIGURE VII-16 MODEL 3, FLAT PLATE,
UNCROSSED POLARIZATION
(NO LENS)

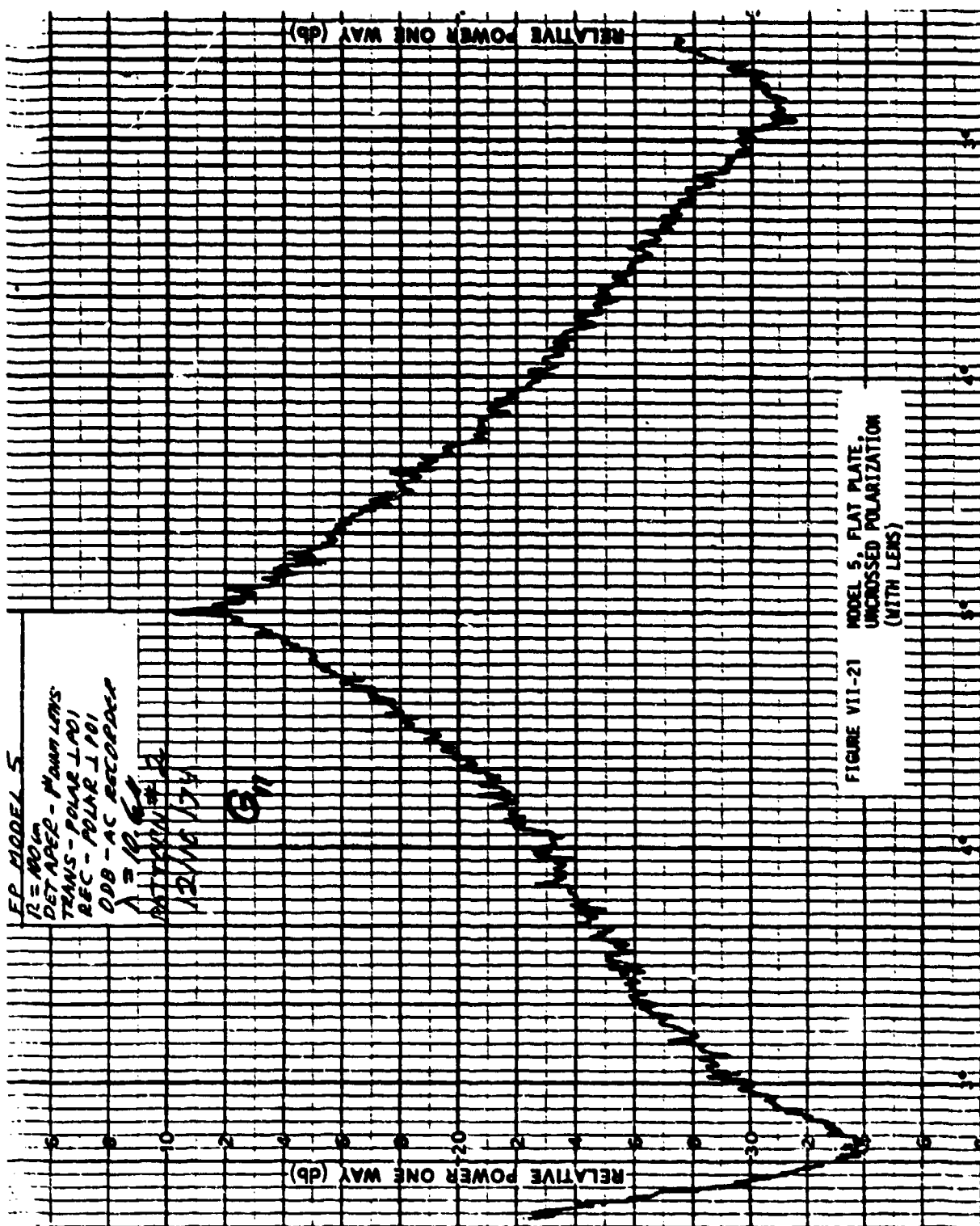


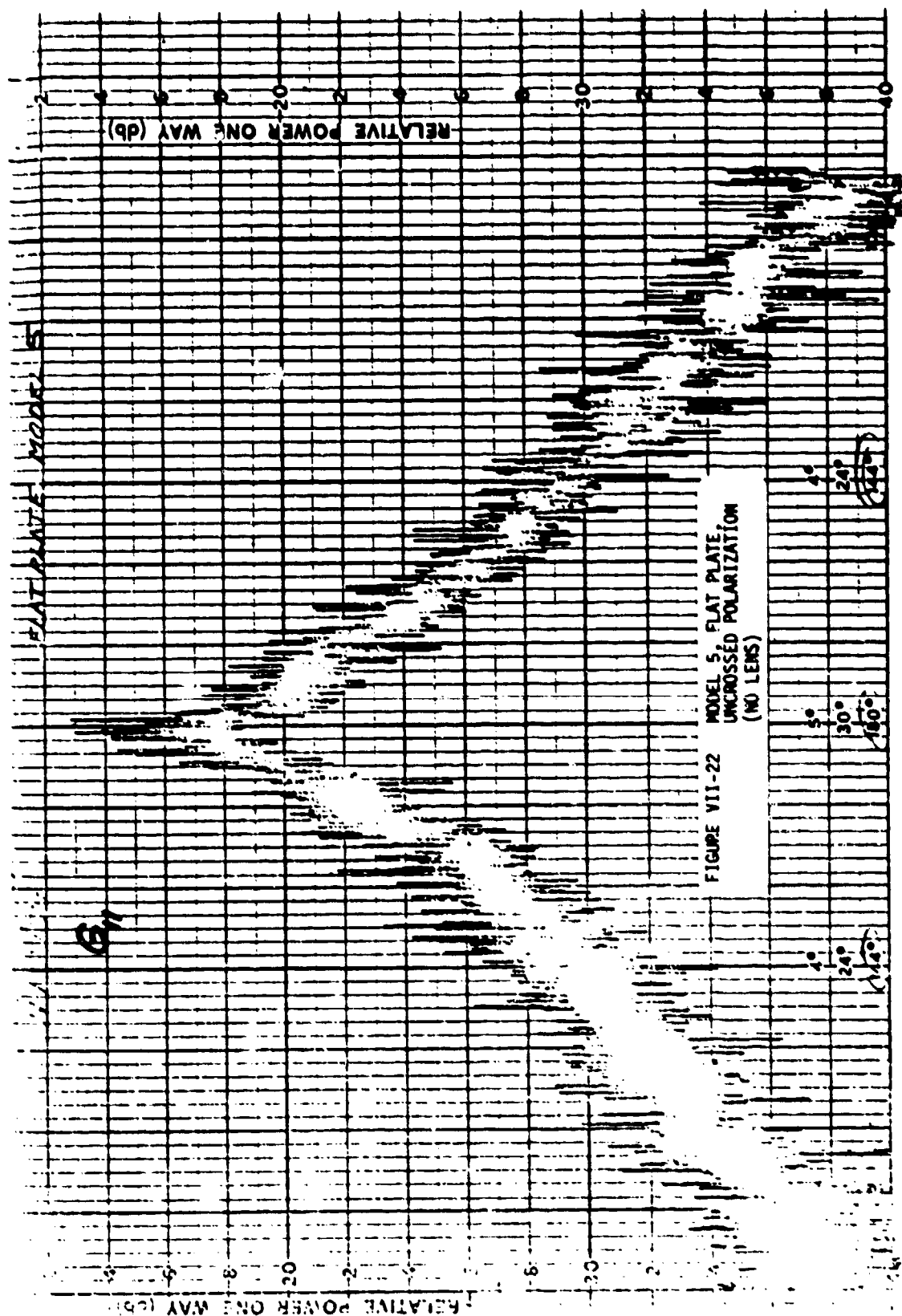












PATTERN NO. DATE 12/10/74

PROJECT

ENGRE.

REMARKS

EE - MODEL 5

R - 10.6

DETAILS - 1" DIA LENS

TRANS - POLAR LPOI

ACC - POLAR HPOI

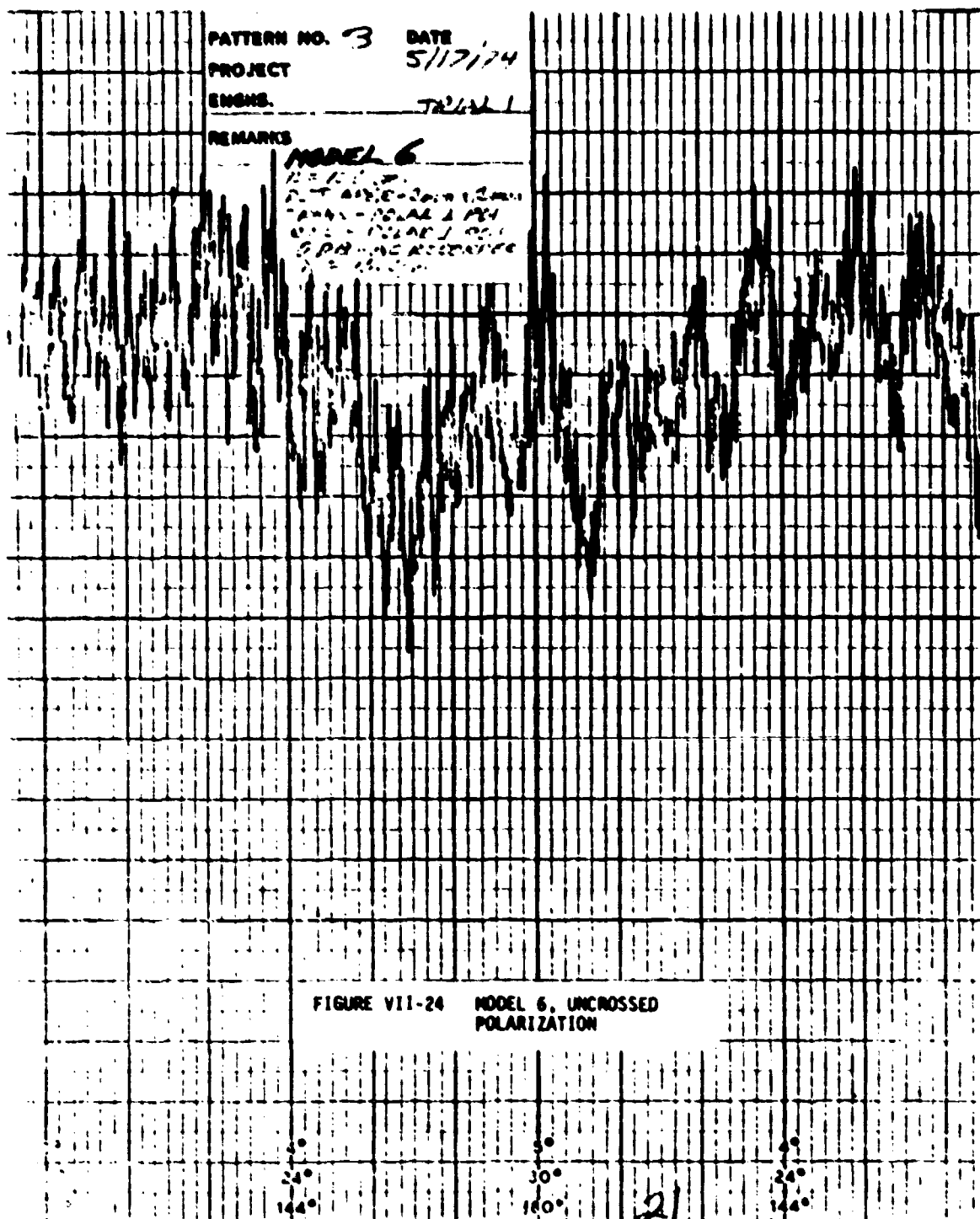
ODS - AC RECORDER

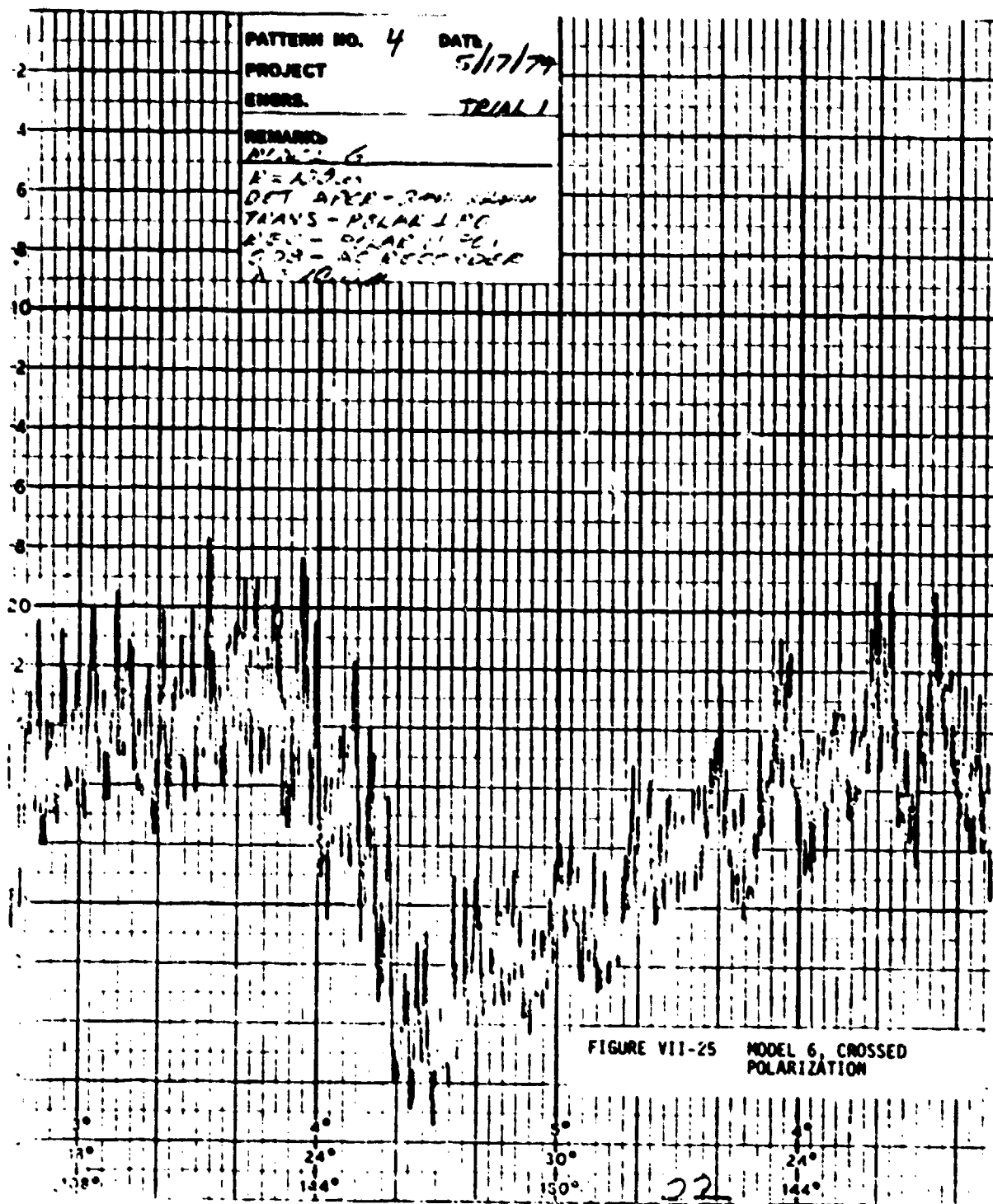
$\lambda = 10.6$

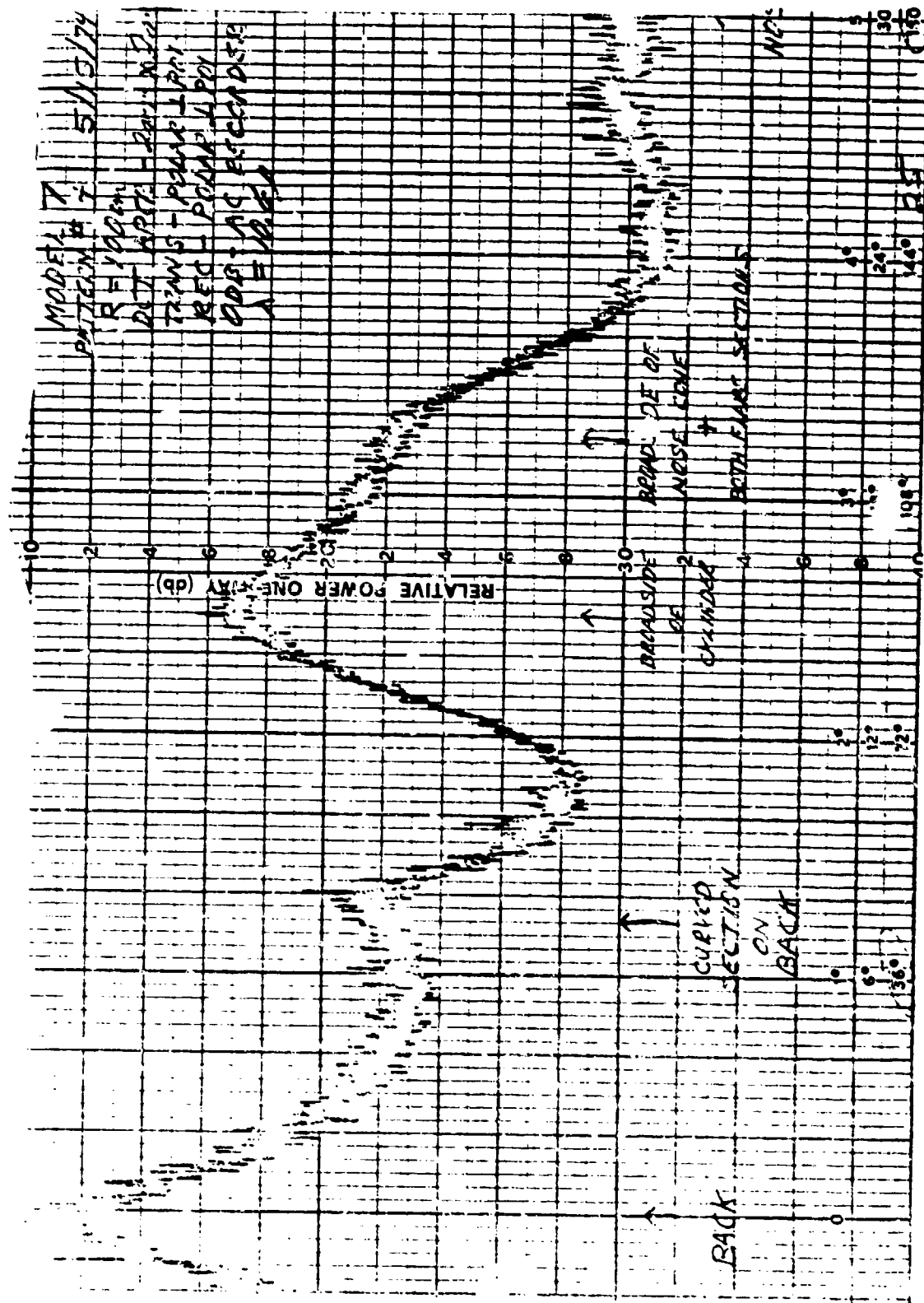
6

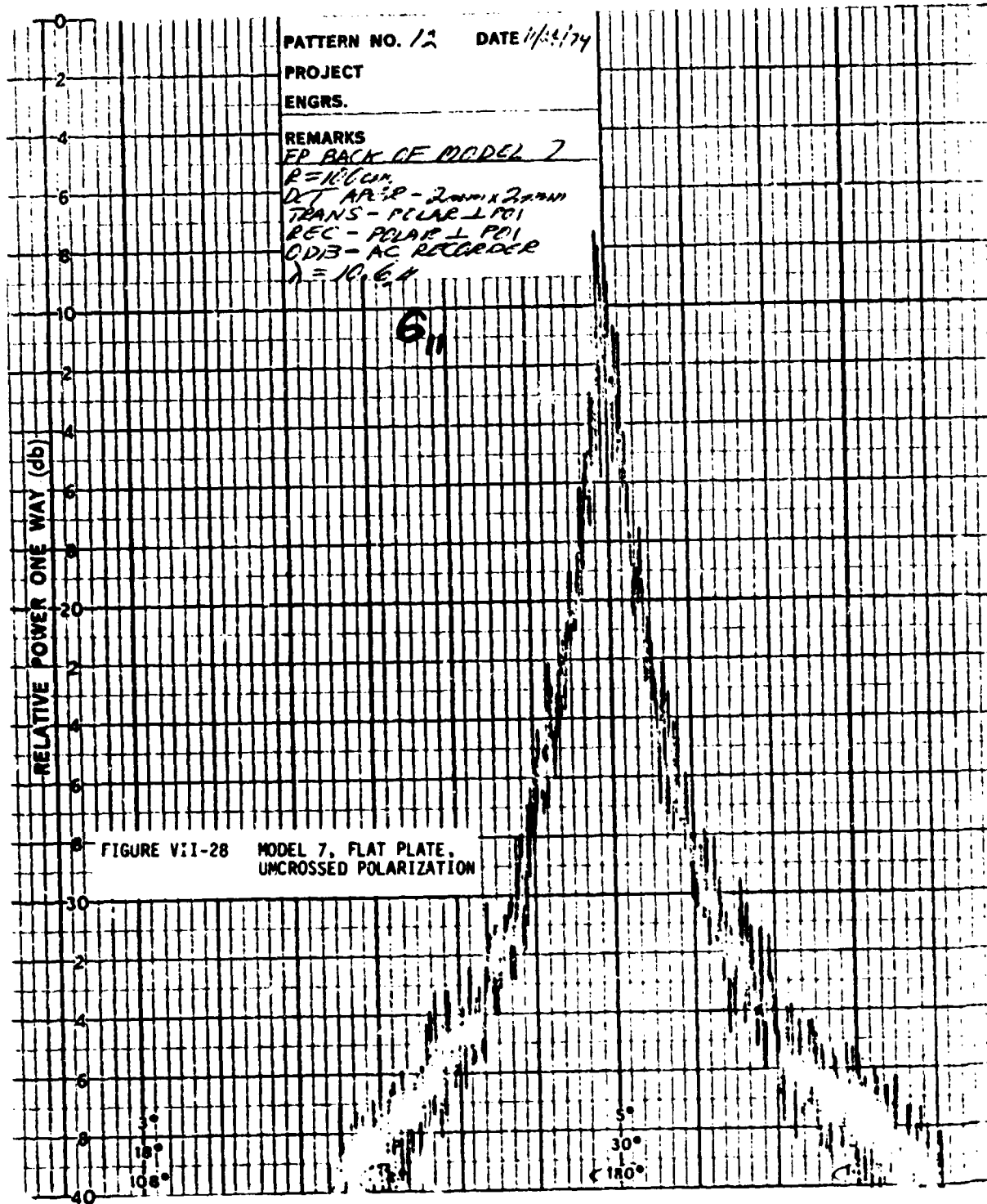
FIGURE VII-23 MODEL 5, FLAT PLATE,
CROSSED POLARIZATION
(WITH LENS)

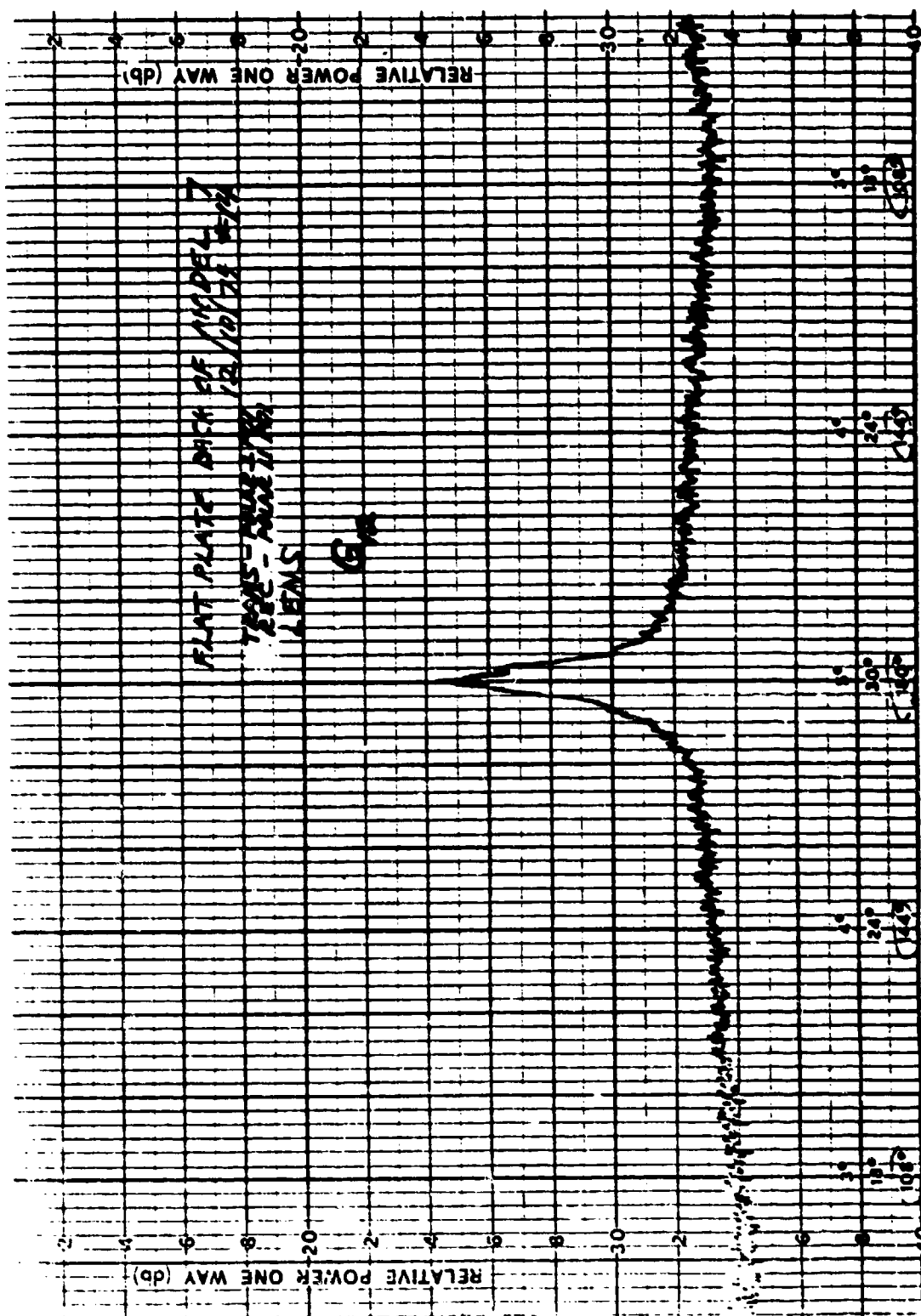












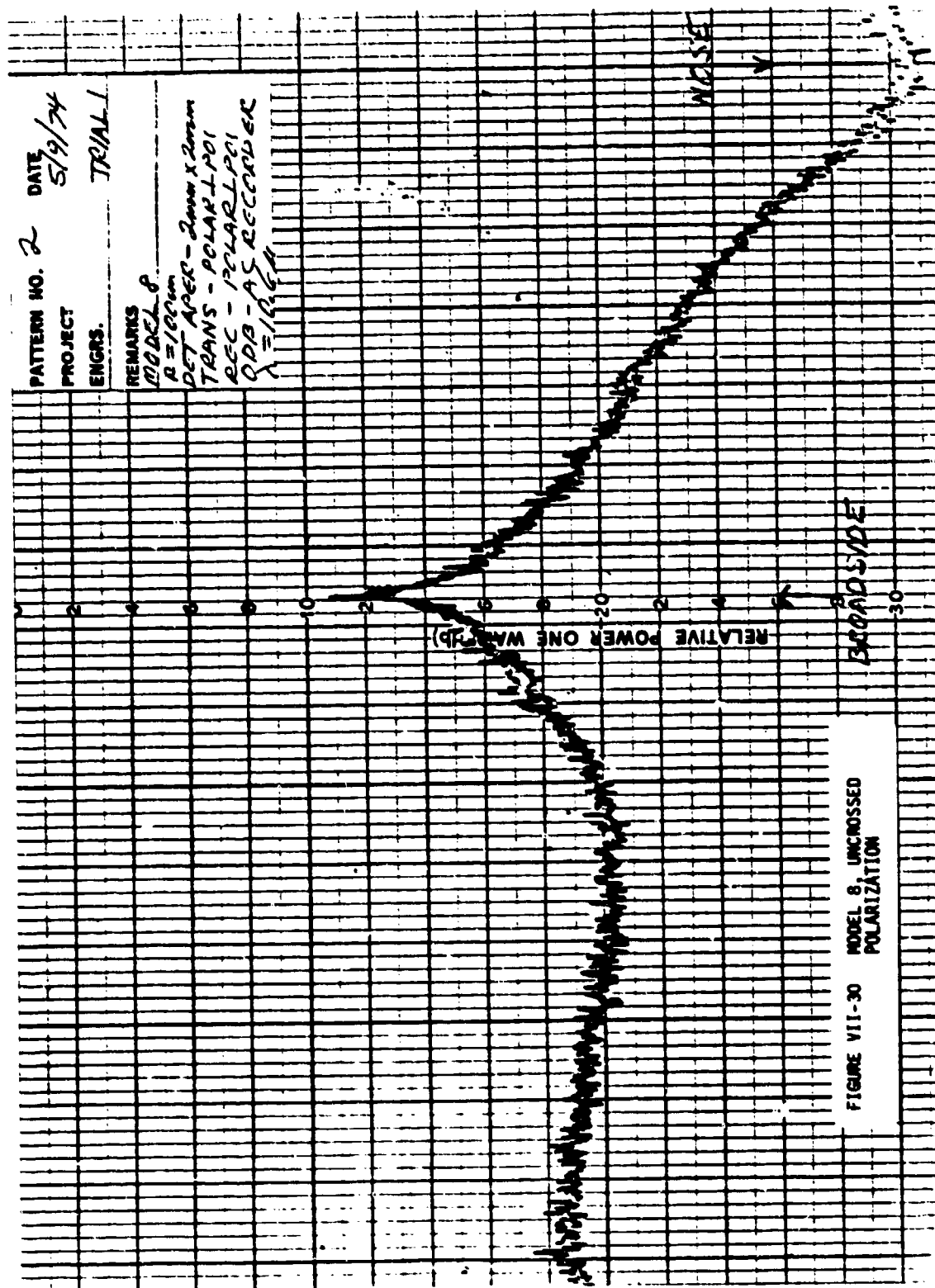
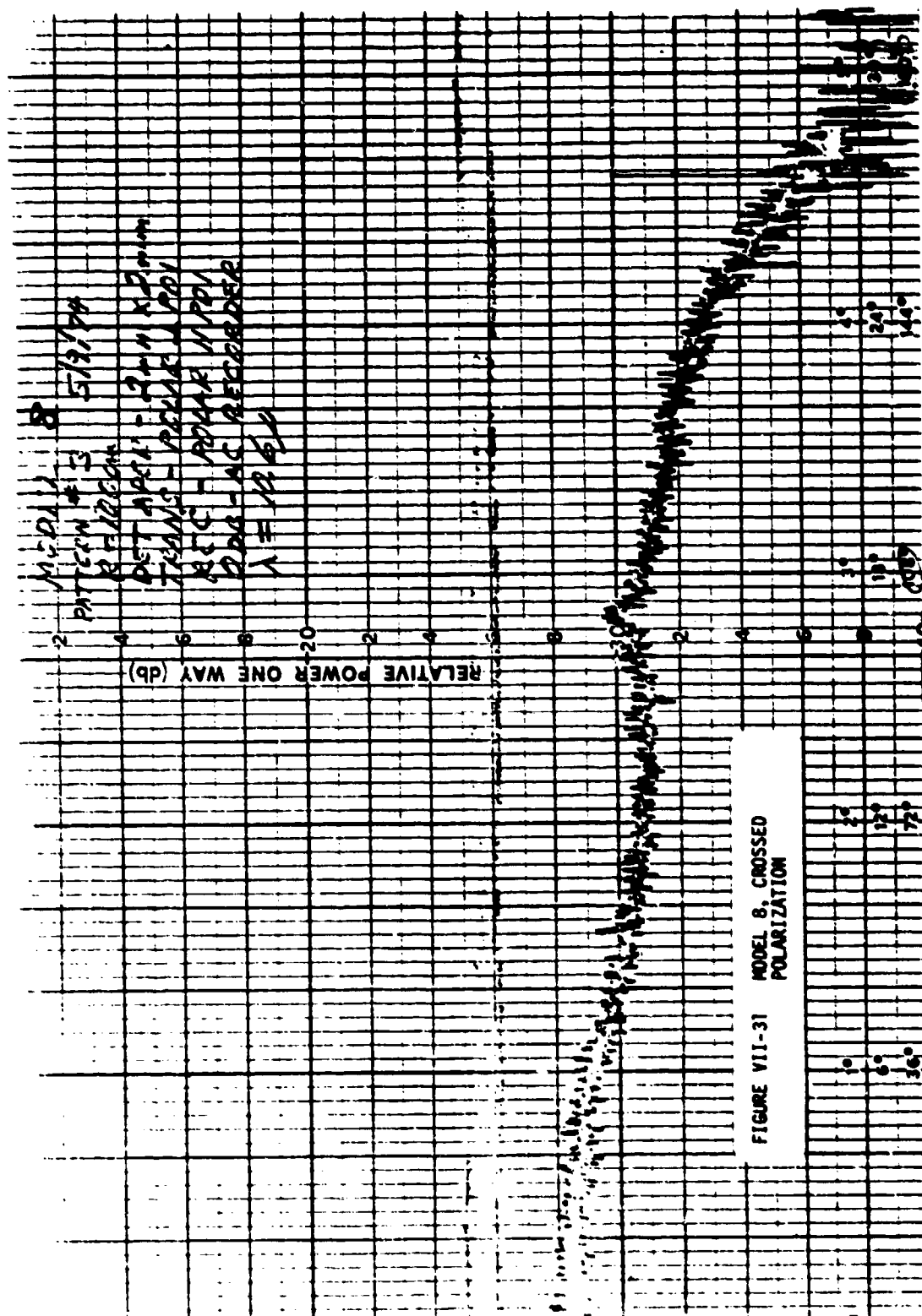
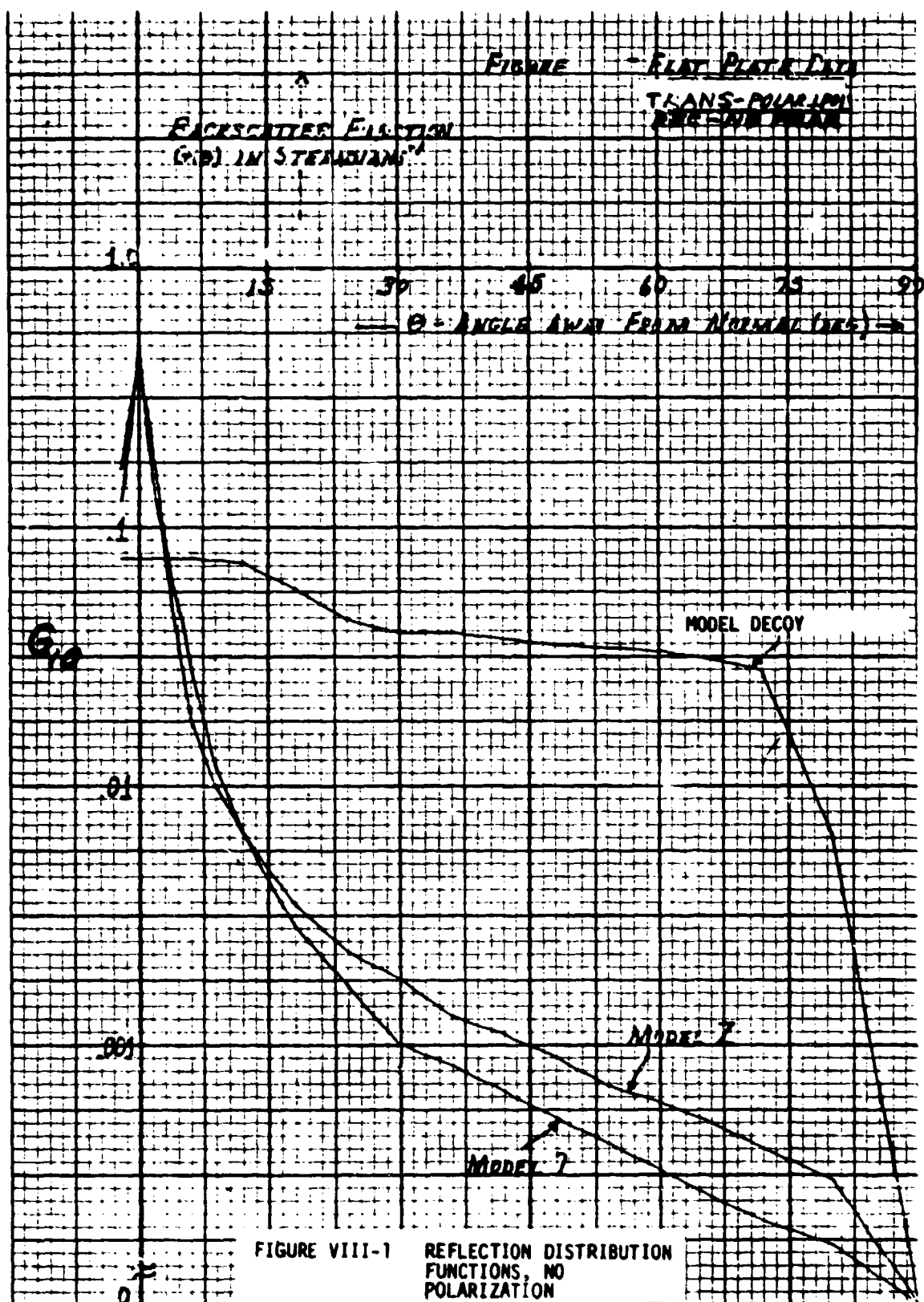
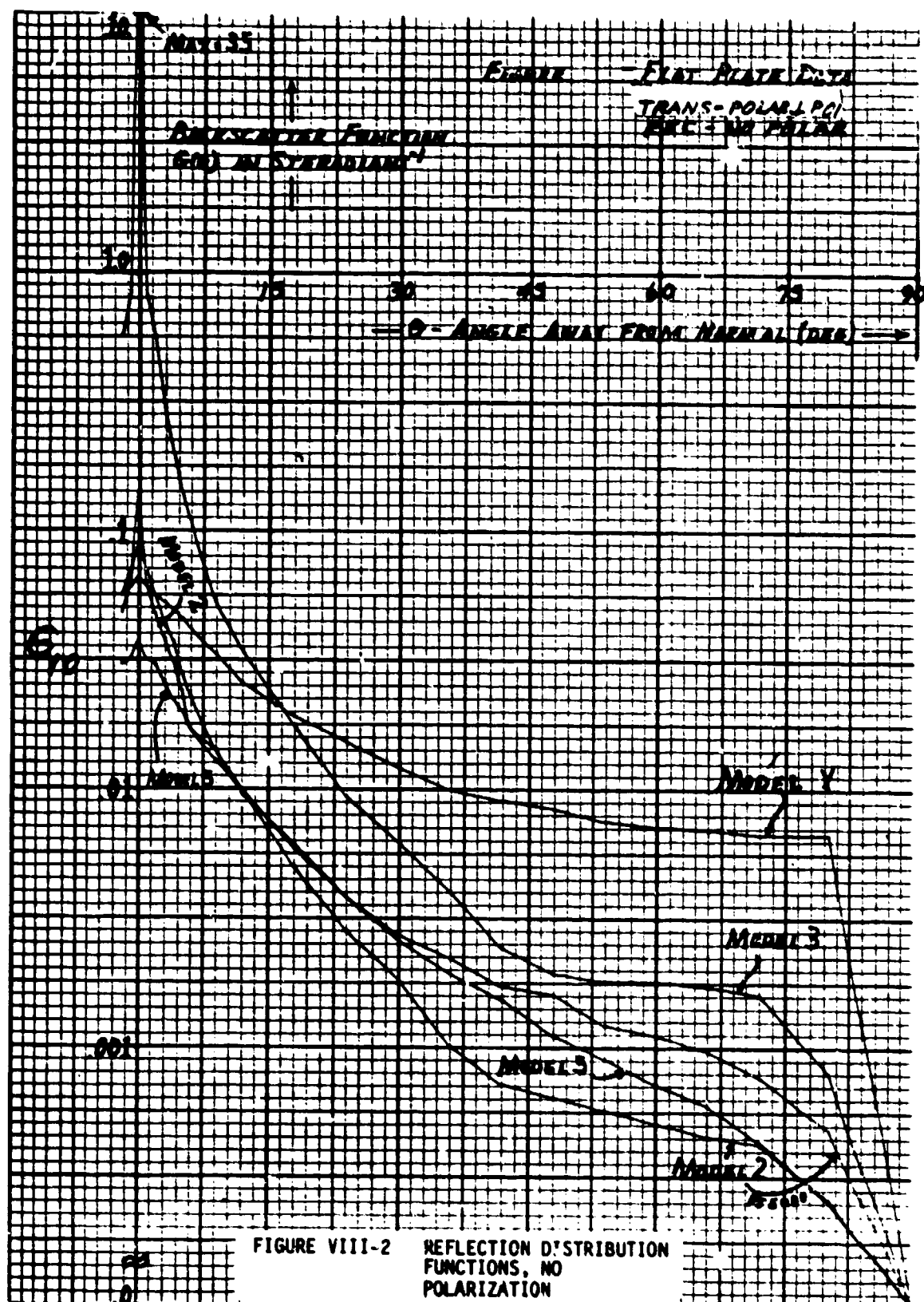
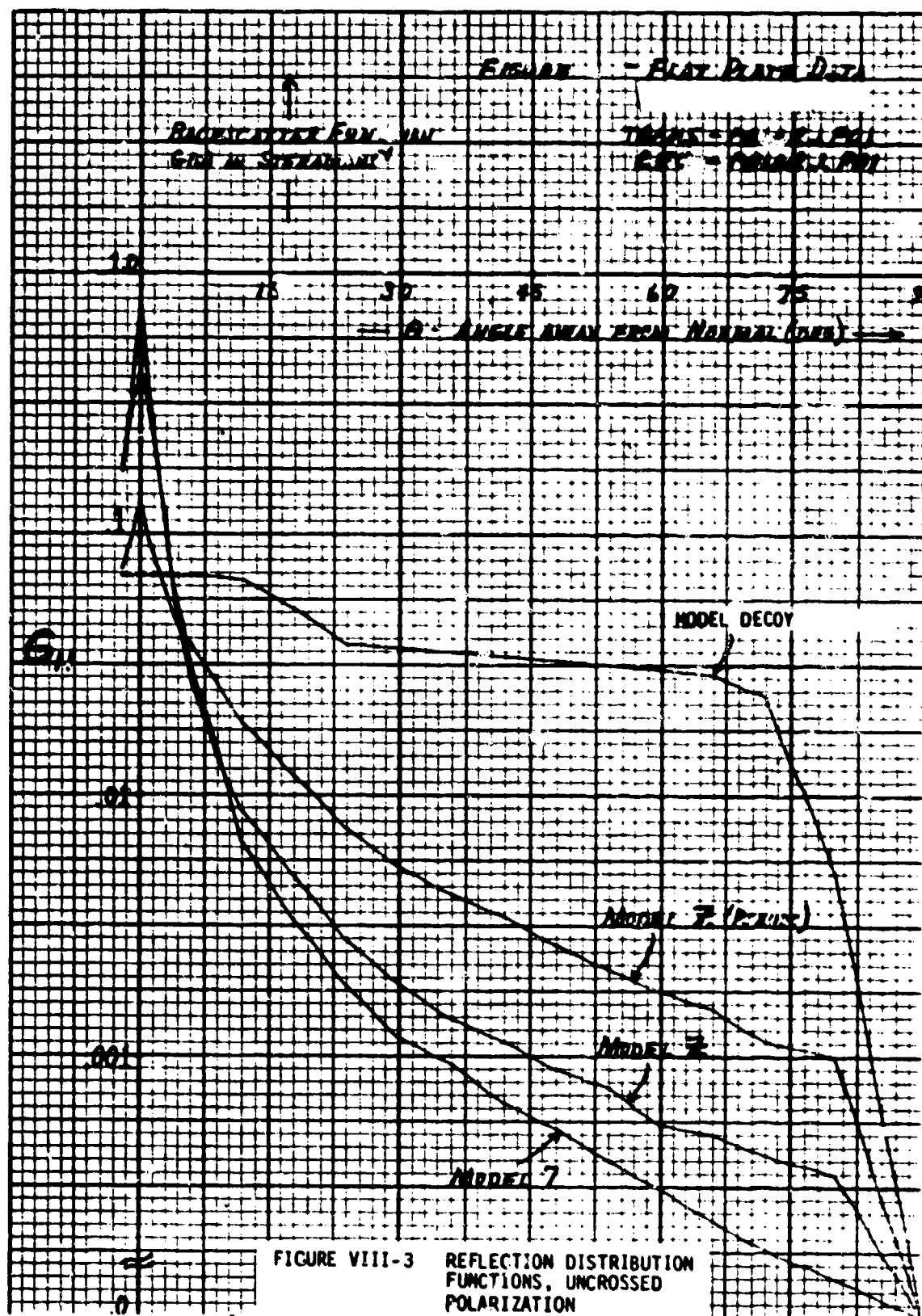


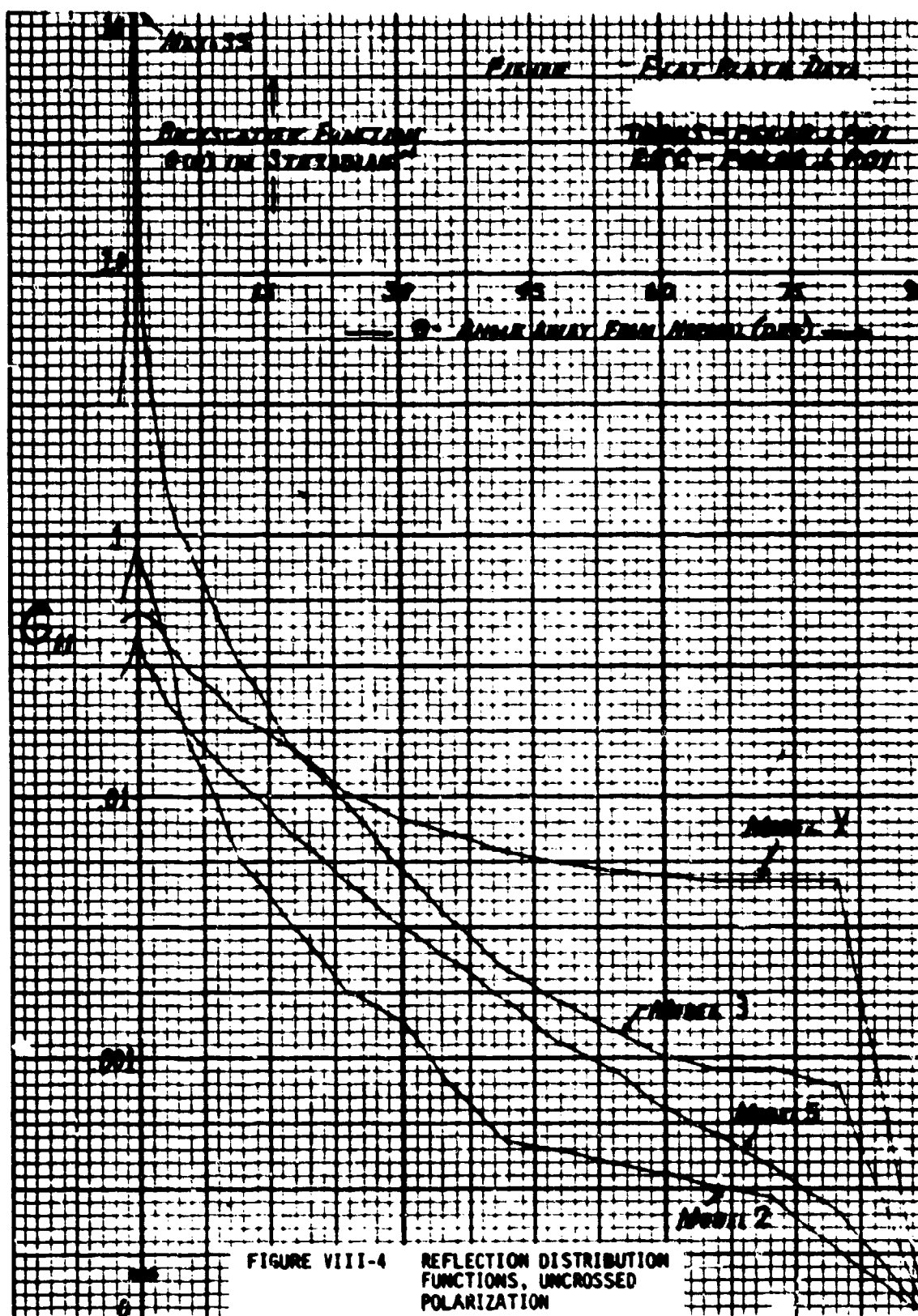
FIGURE VII-30 MODEL 8, UNCROSSED POLARIZATION

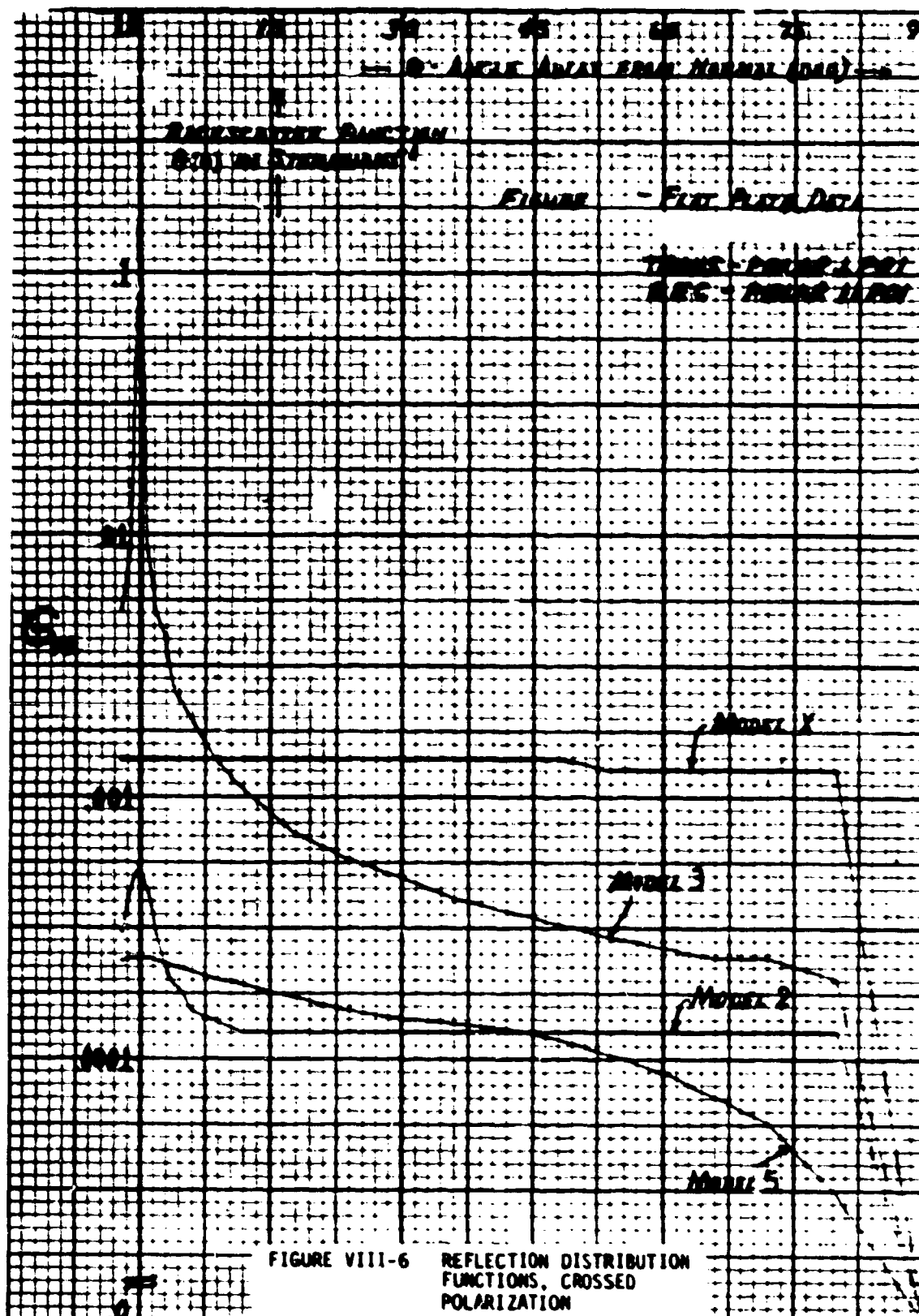












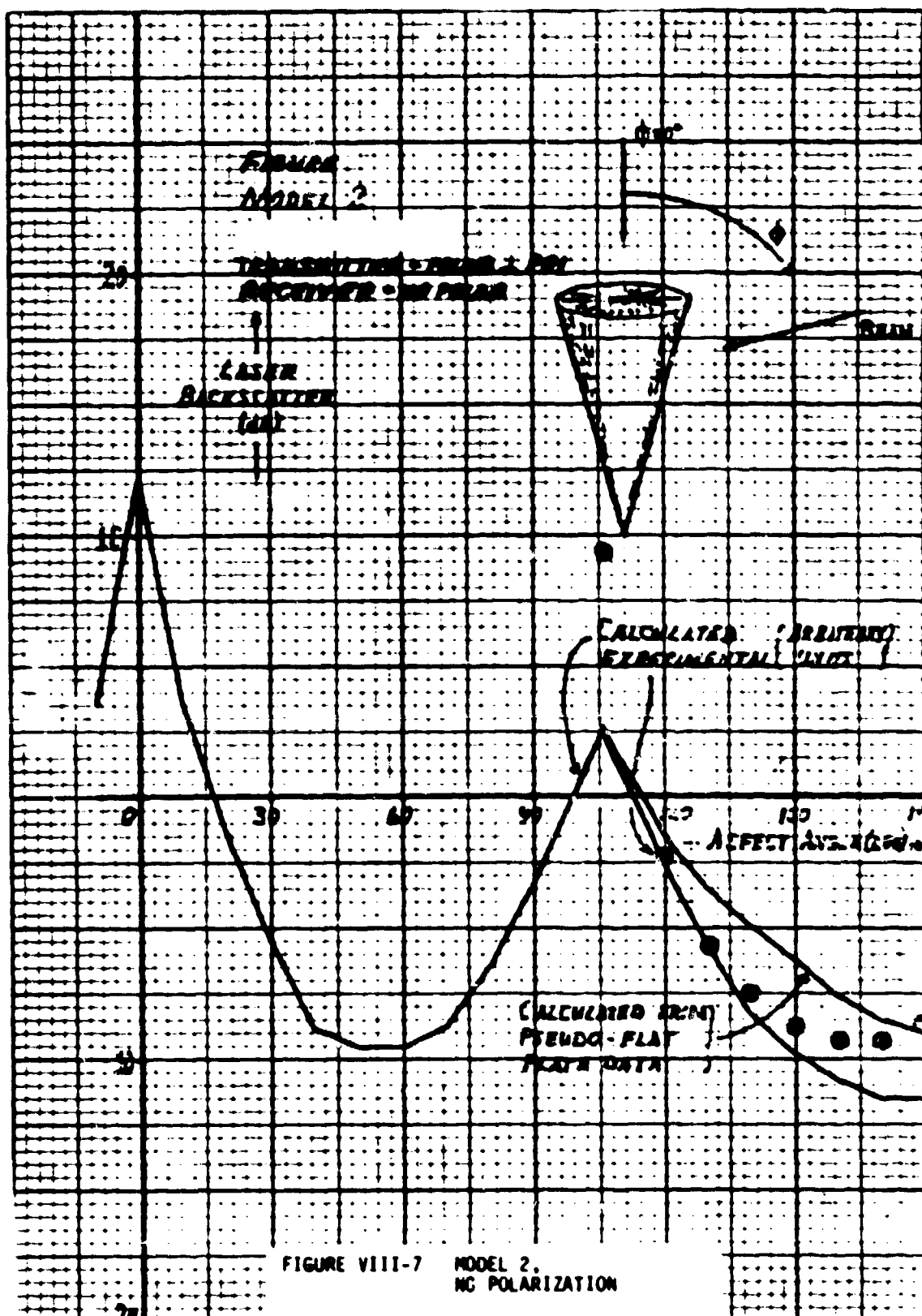


FIGURE VIII-7 MODEL 2.
NO POLARIZATION

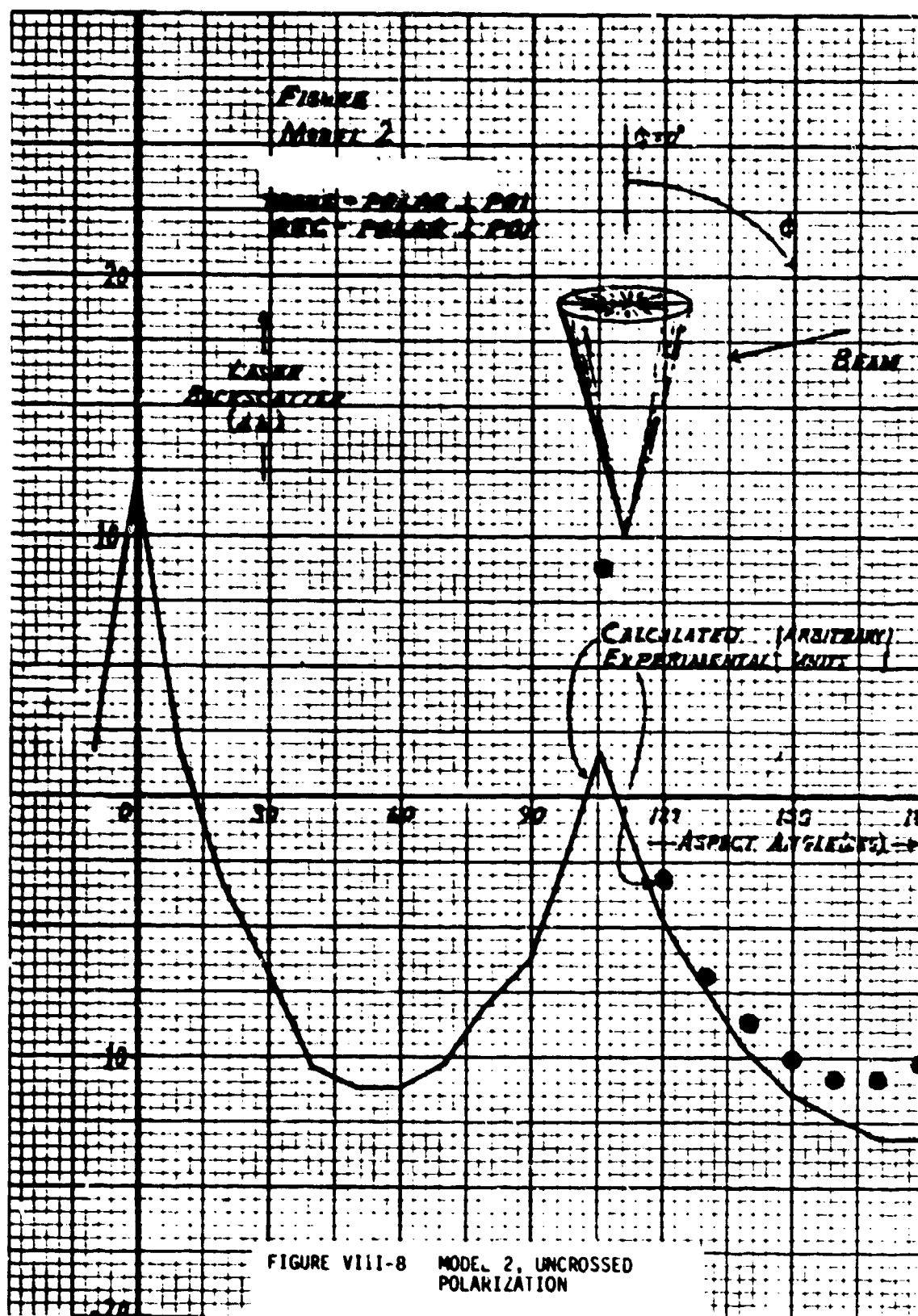
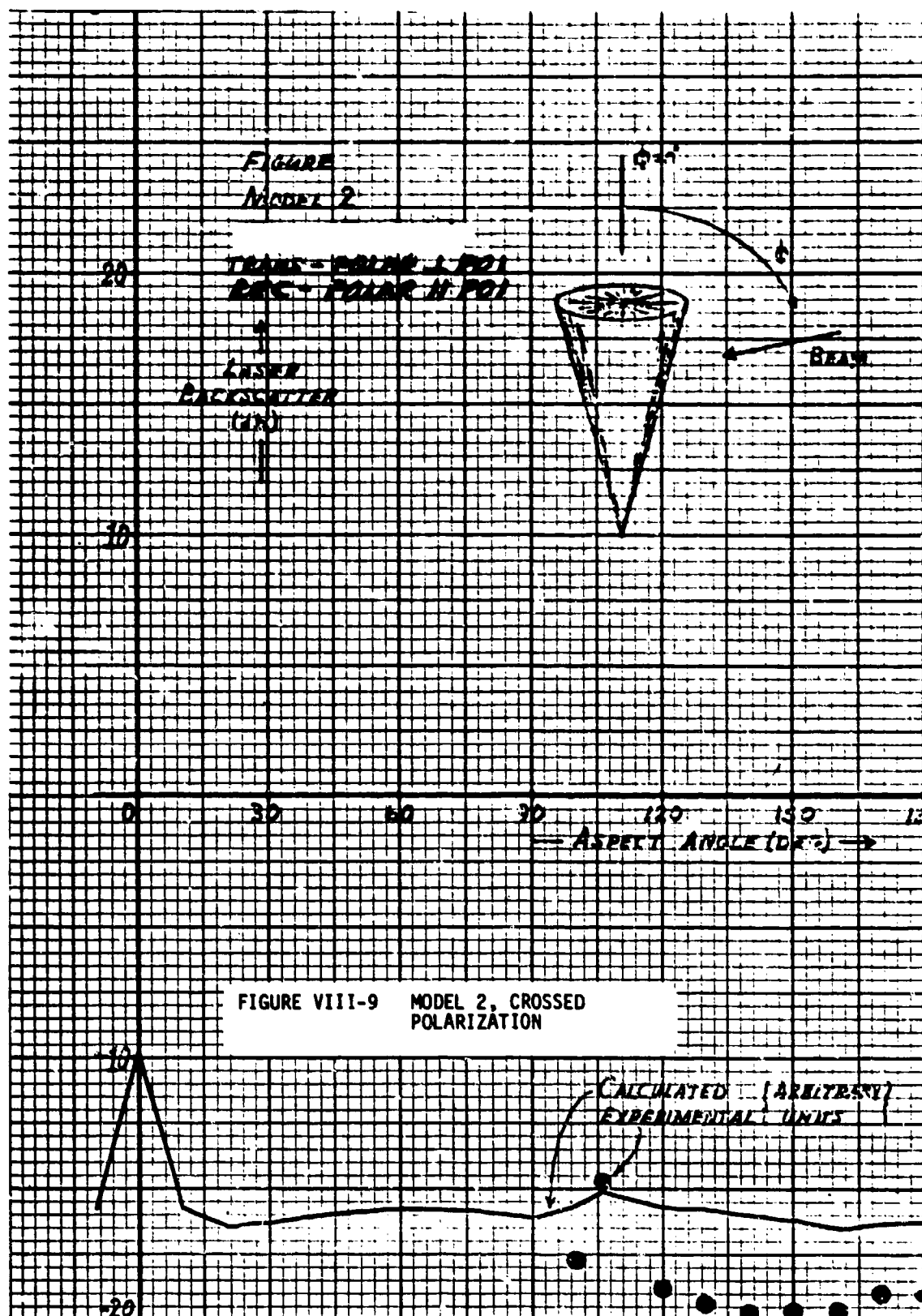


FIGURE VIII-8 MODEL 2, UNCROSSED POLARIZATION



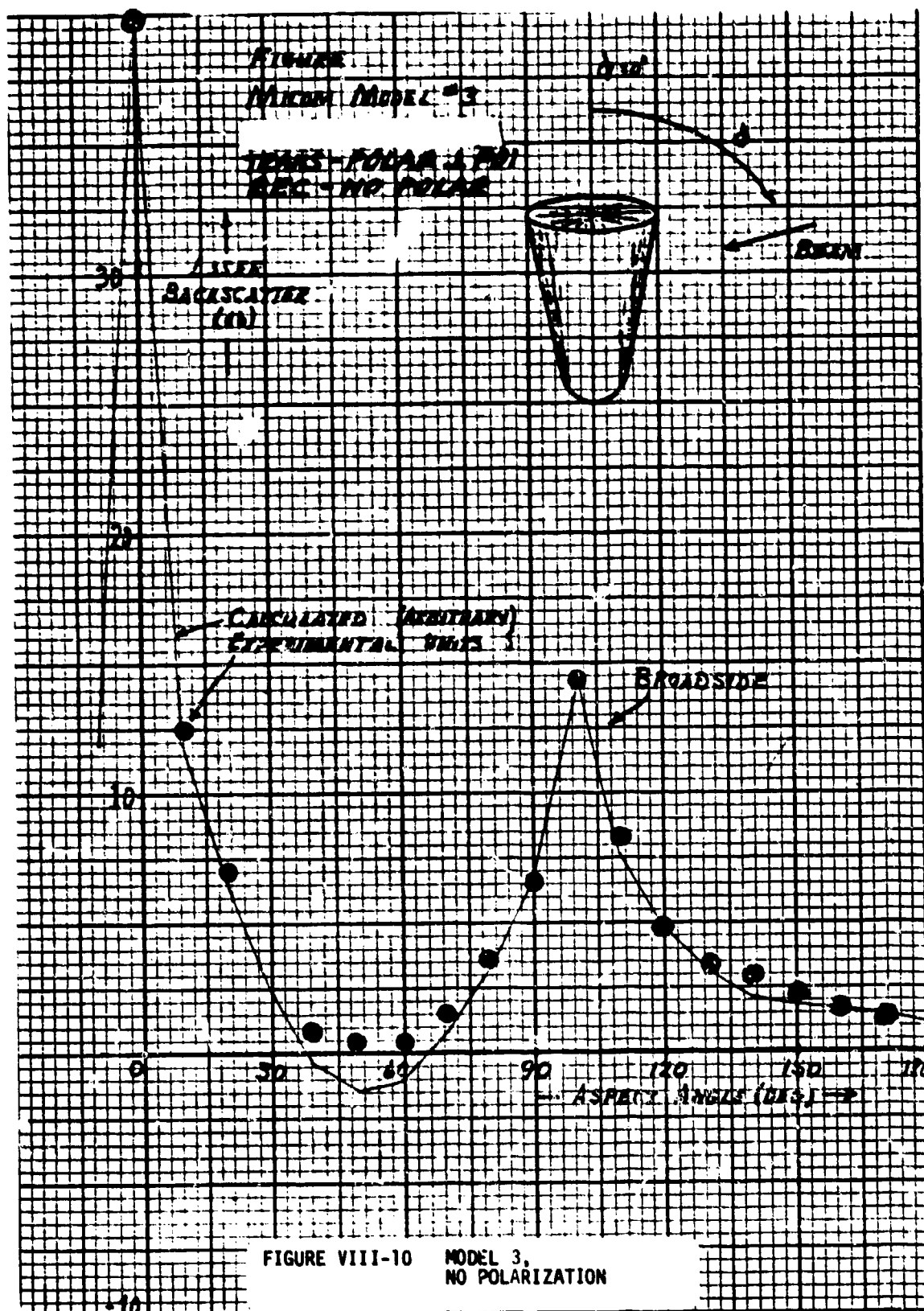


FIGURE VIII-10 MODEL 3,
NO POLARIZATION

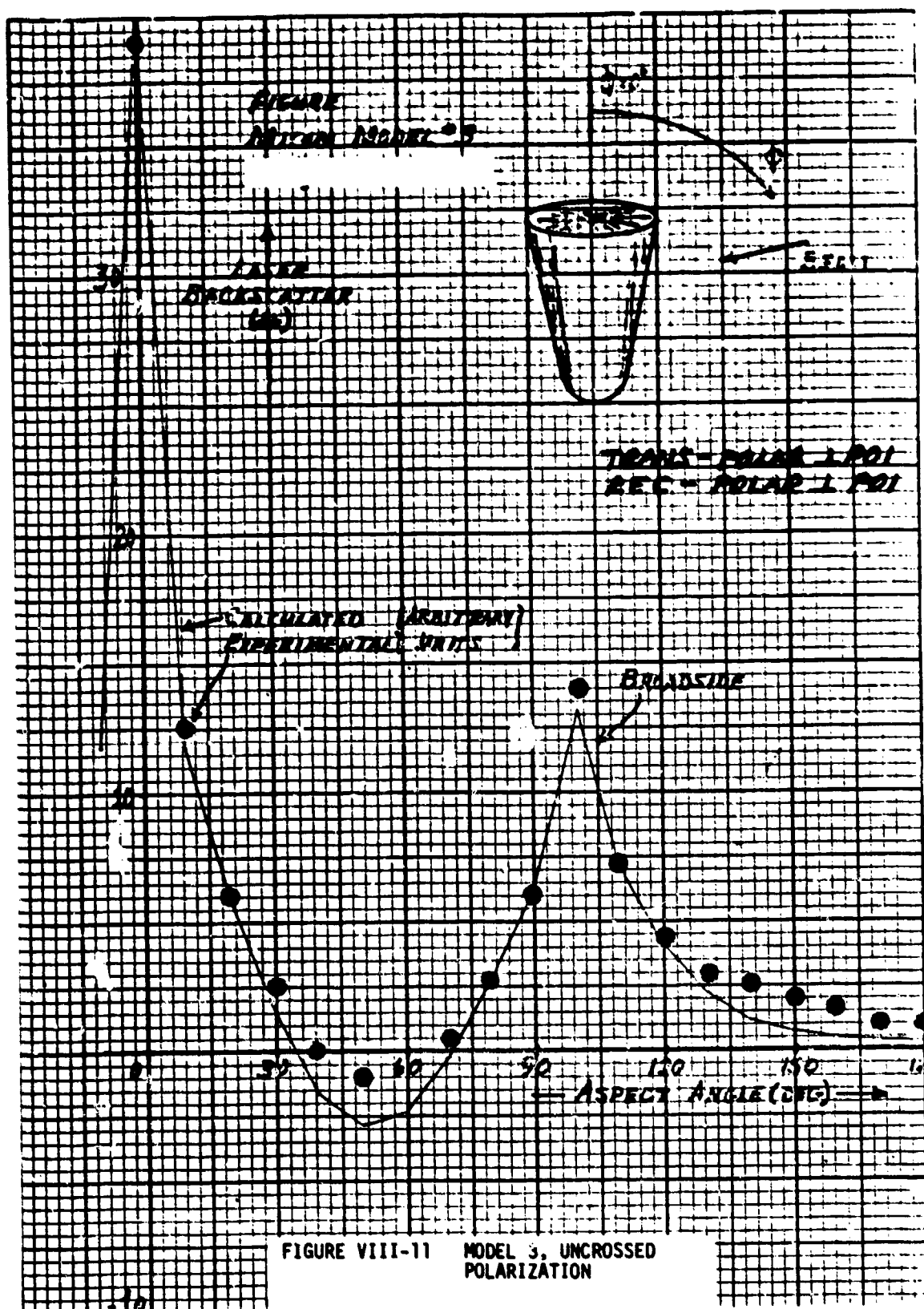
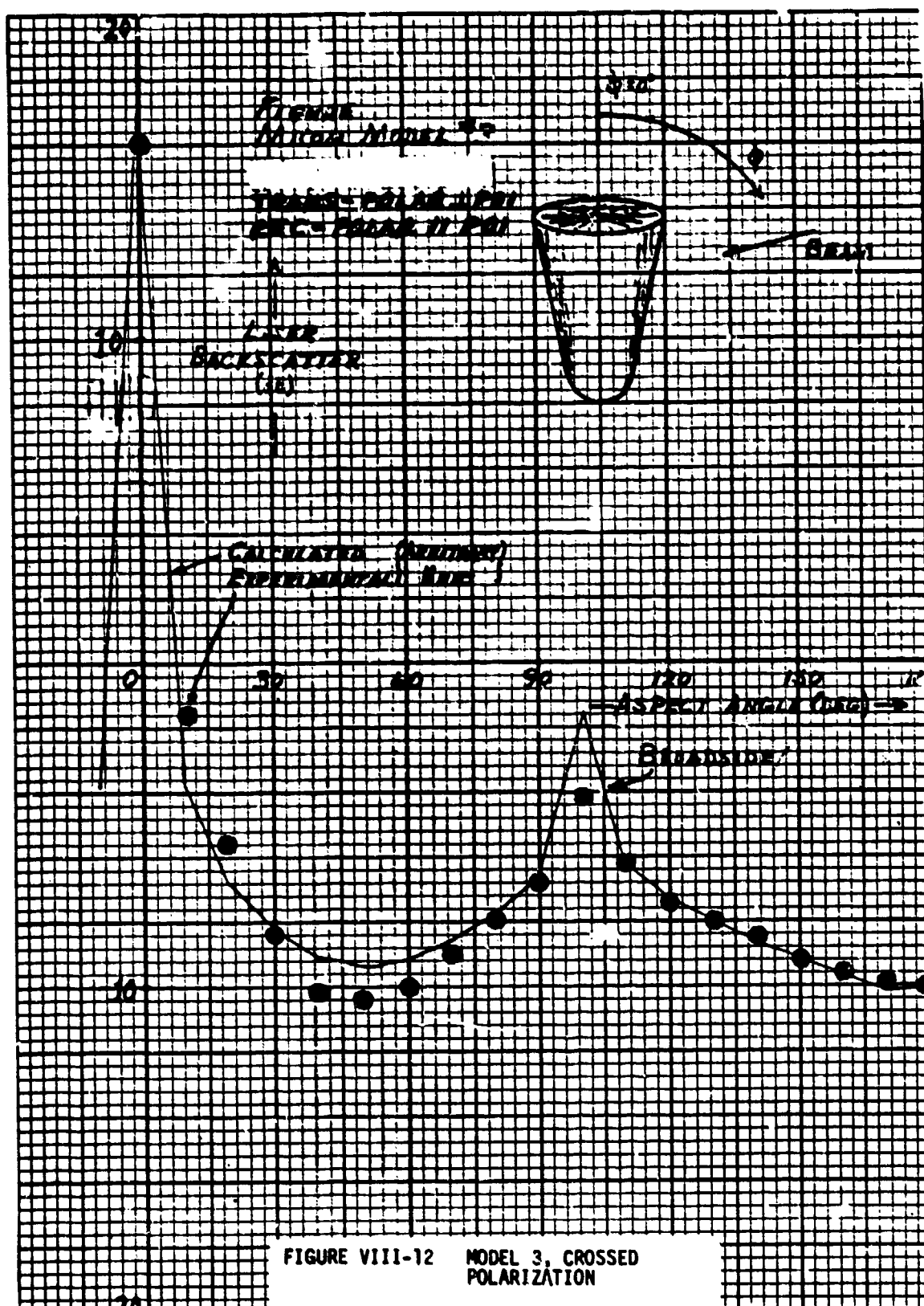
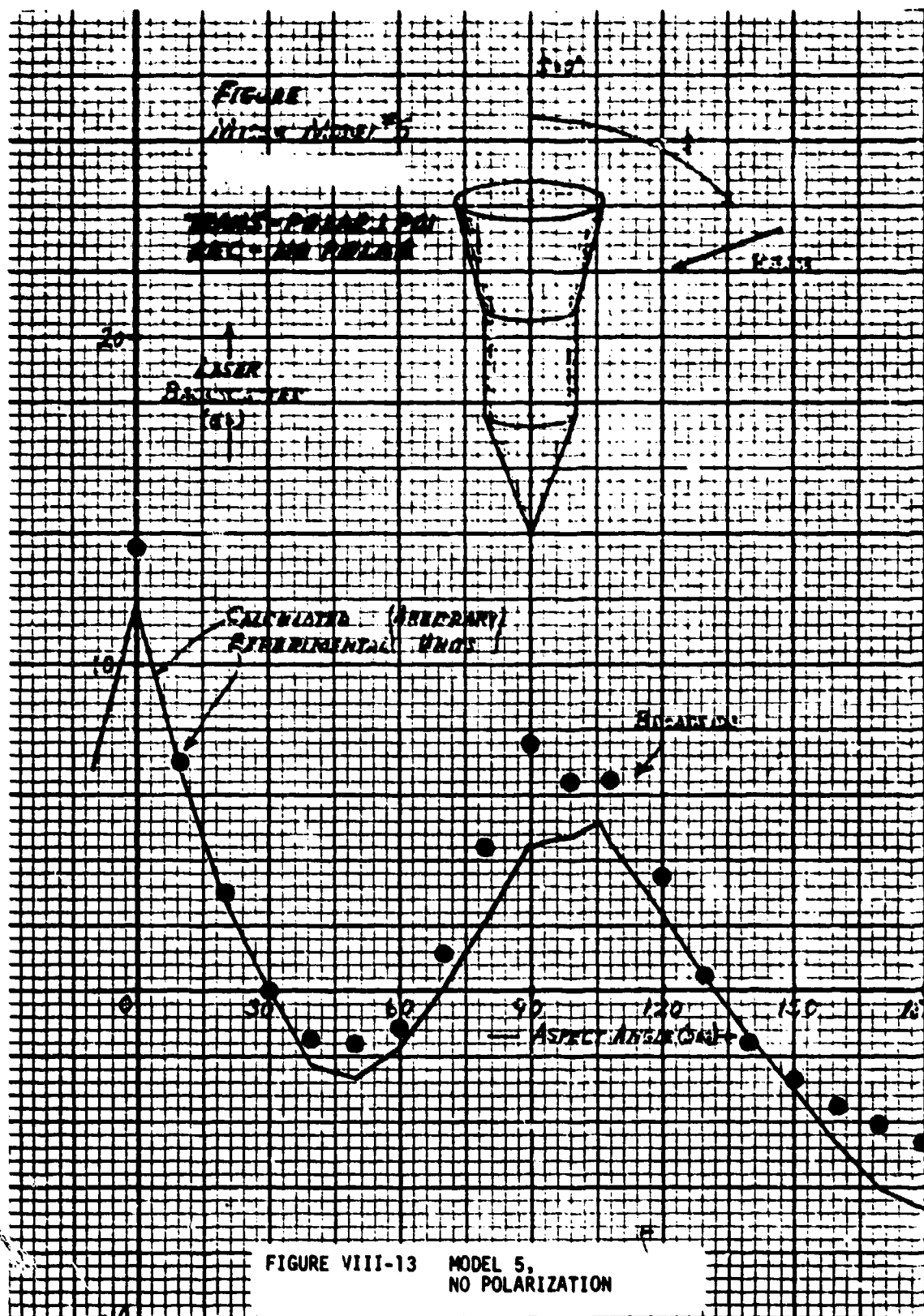
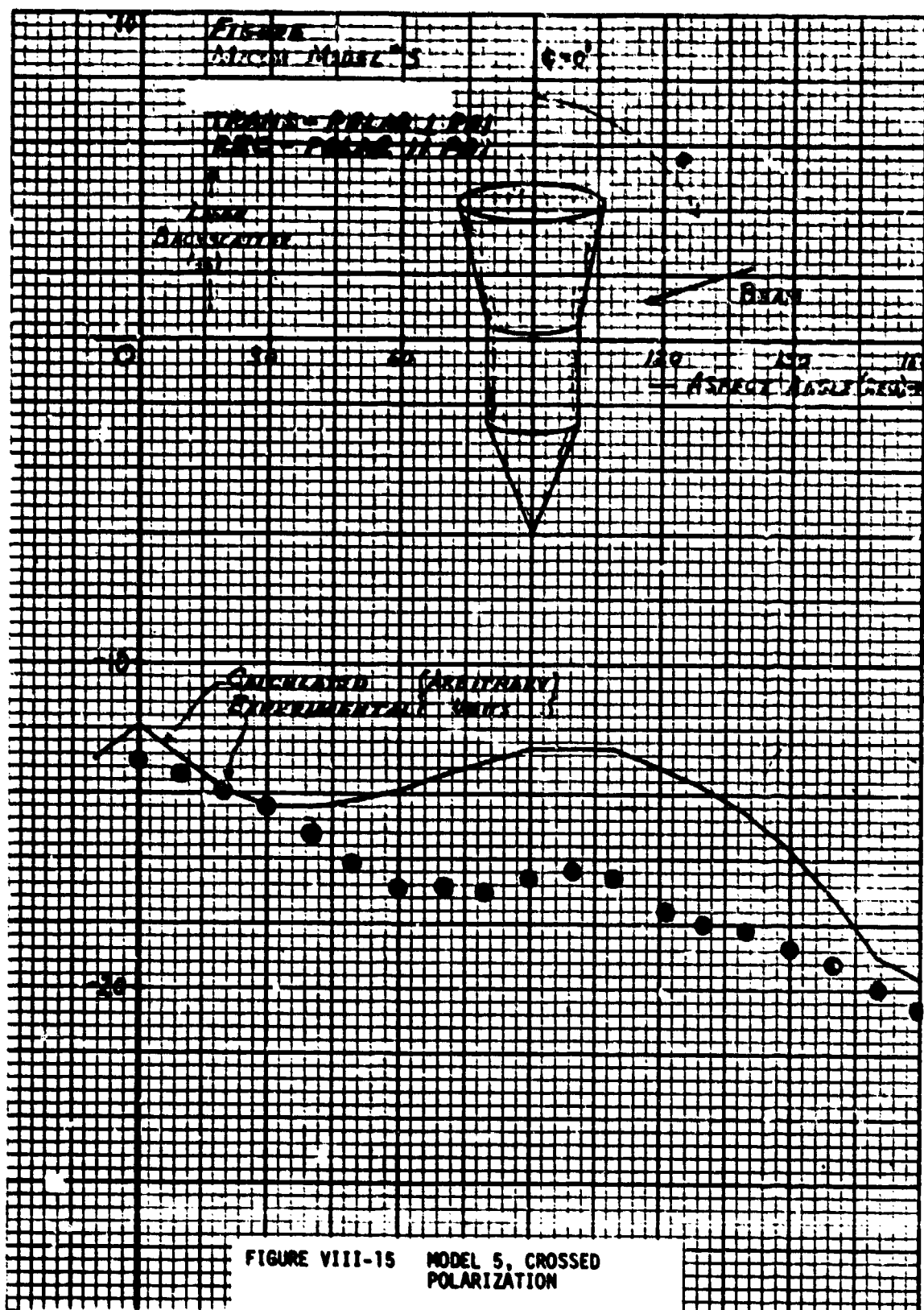


FIGURE VIII-11 MODEL 3, UNCROSSED POLARIZATION







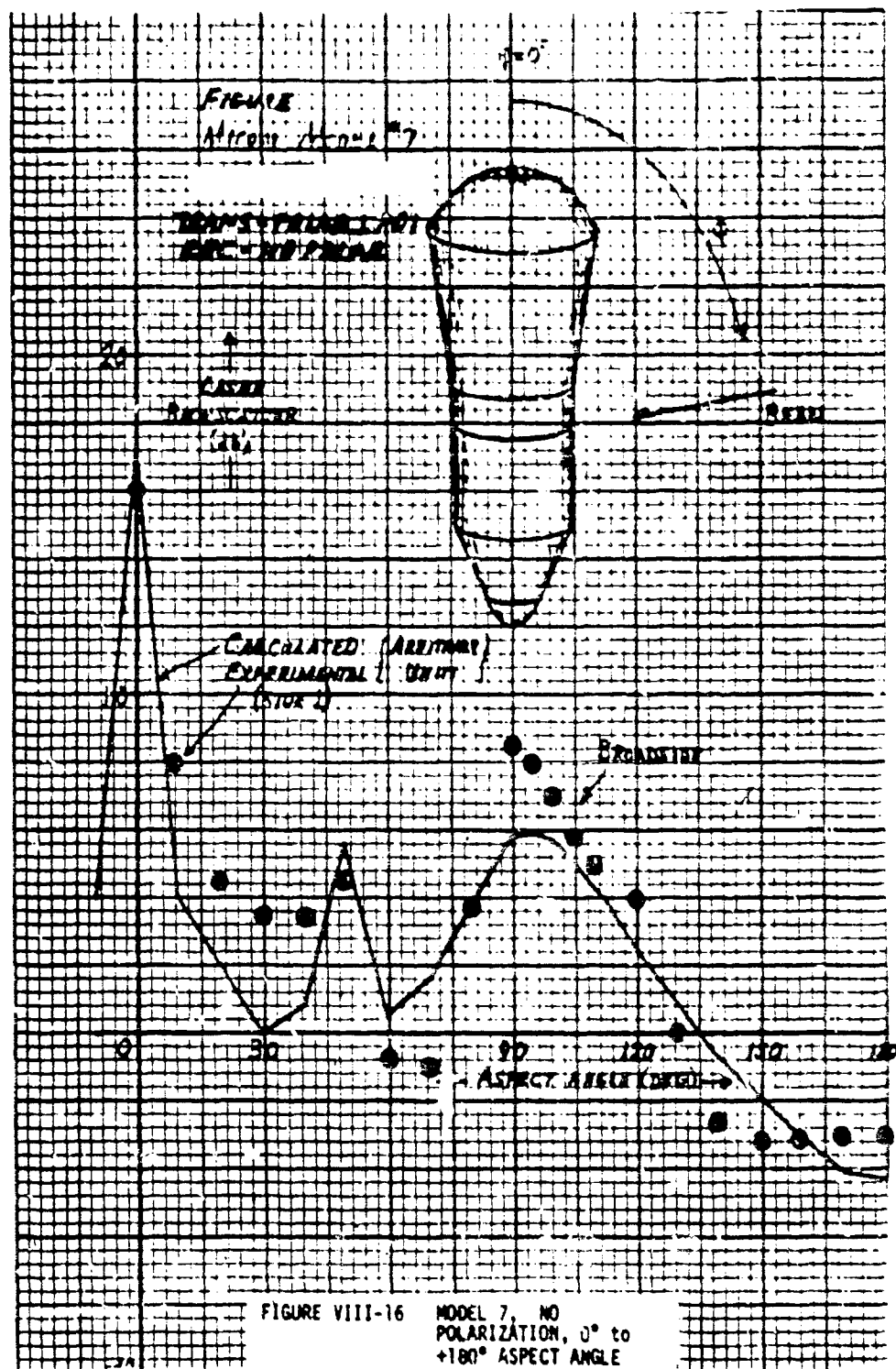
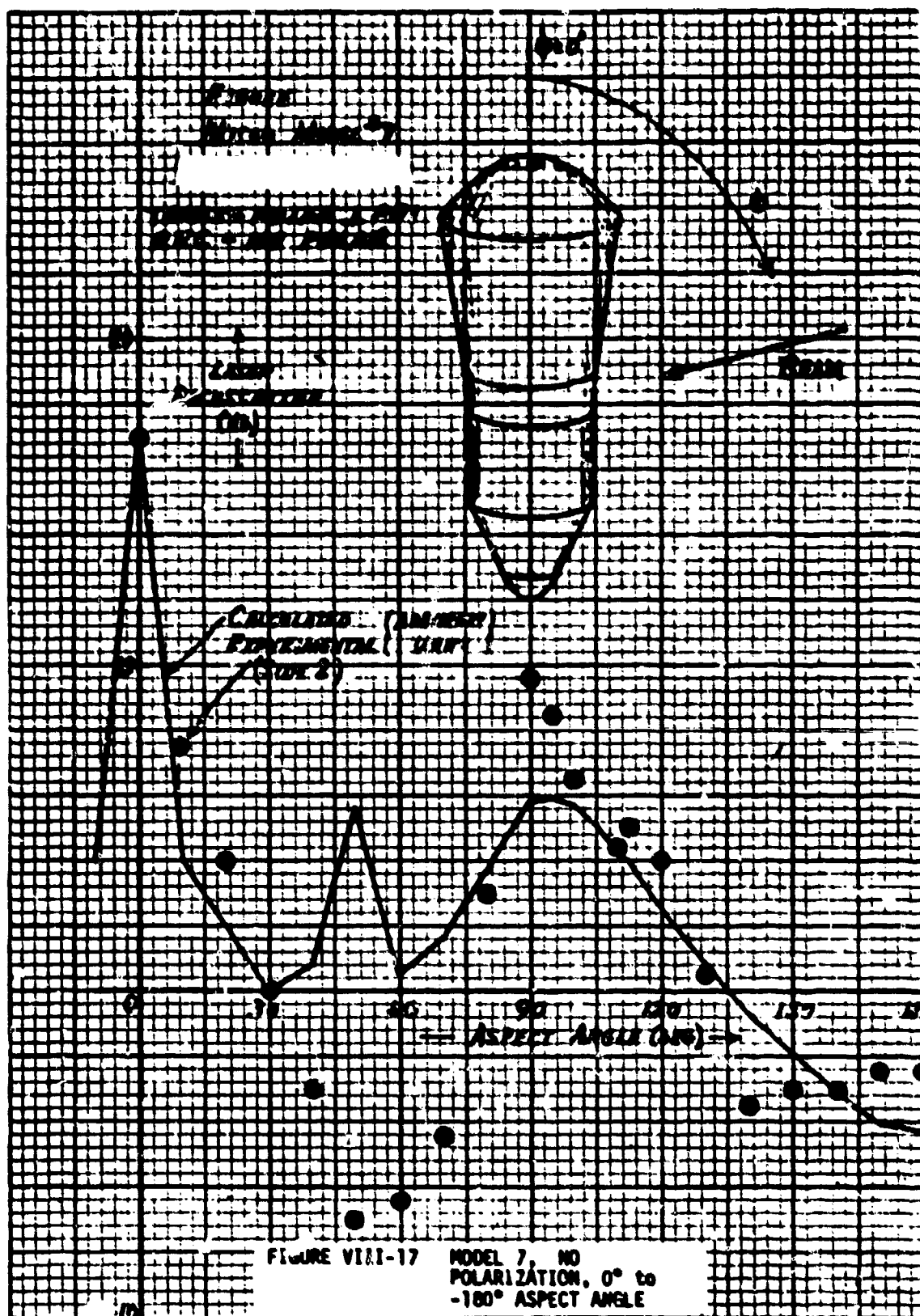


FIGURE VIII-16 MODEL 7, NO POLARIZATION, 0° to +180° ASPECT ANGLE



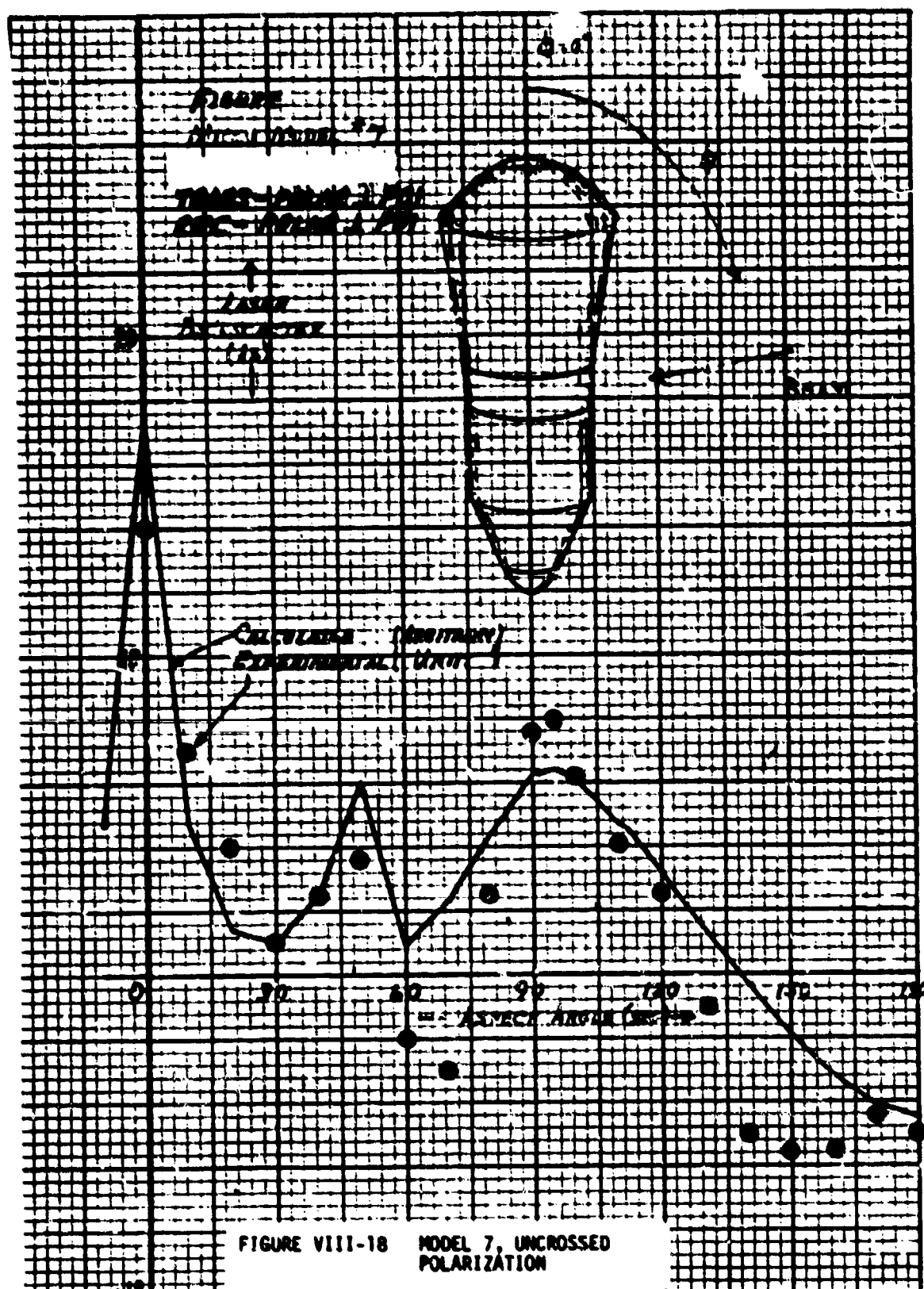
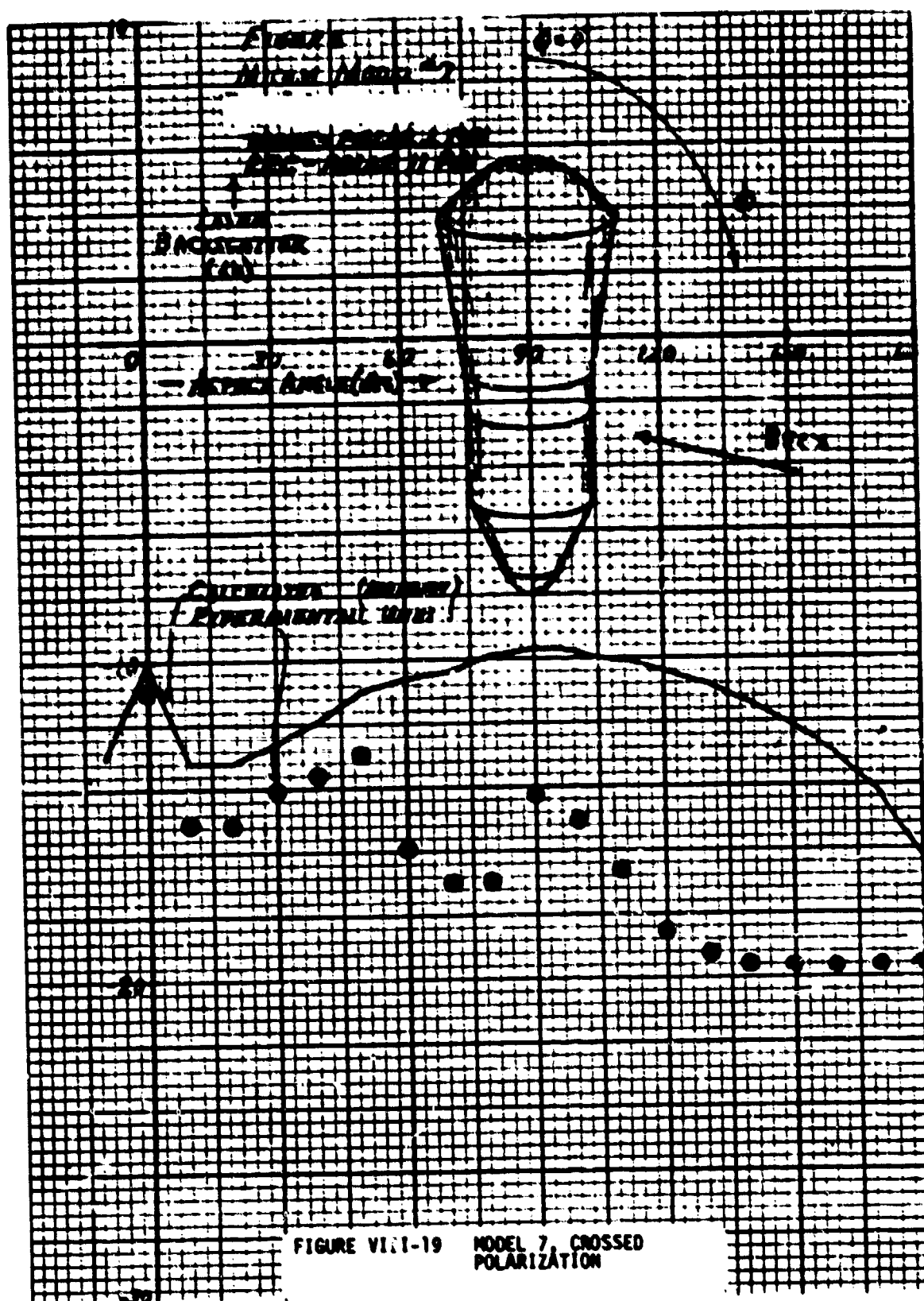
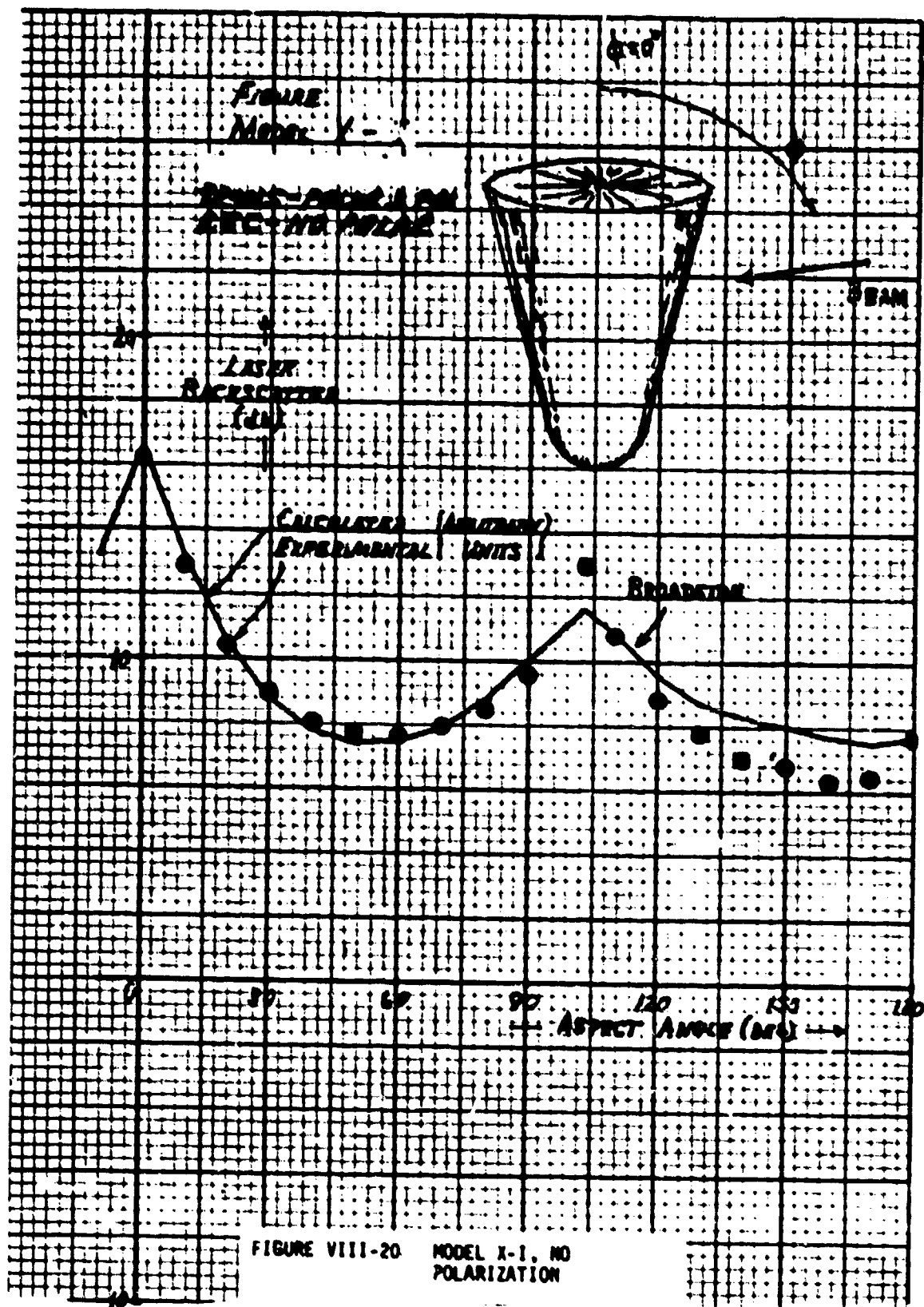


FIGURE VIII-18 MODEL 7, UNCROSSED POLARIZATION





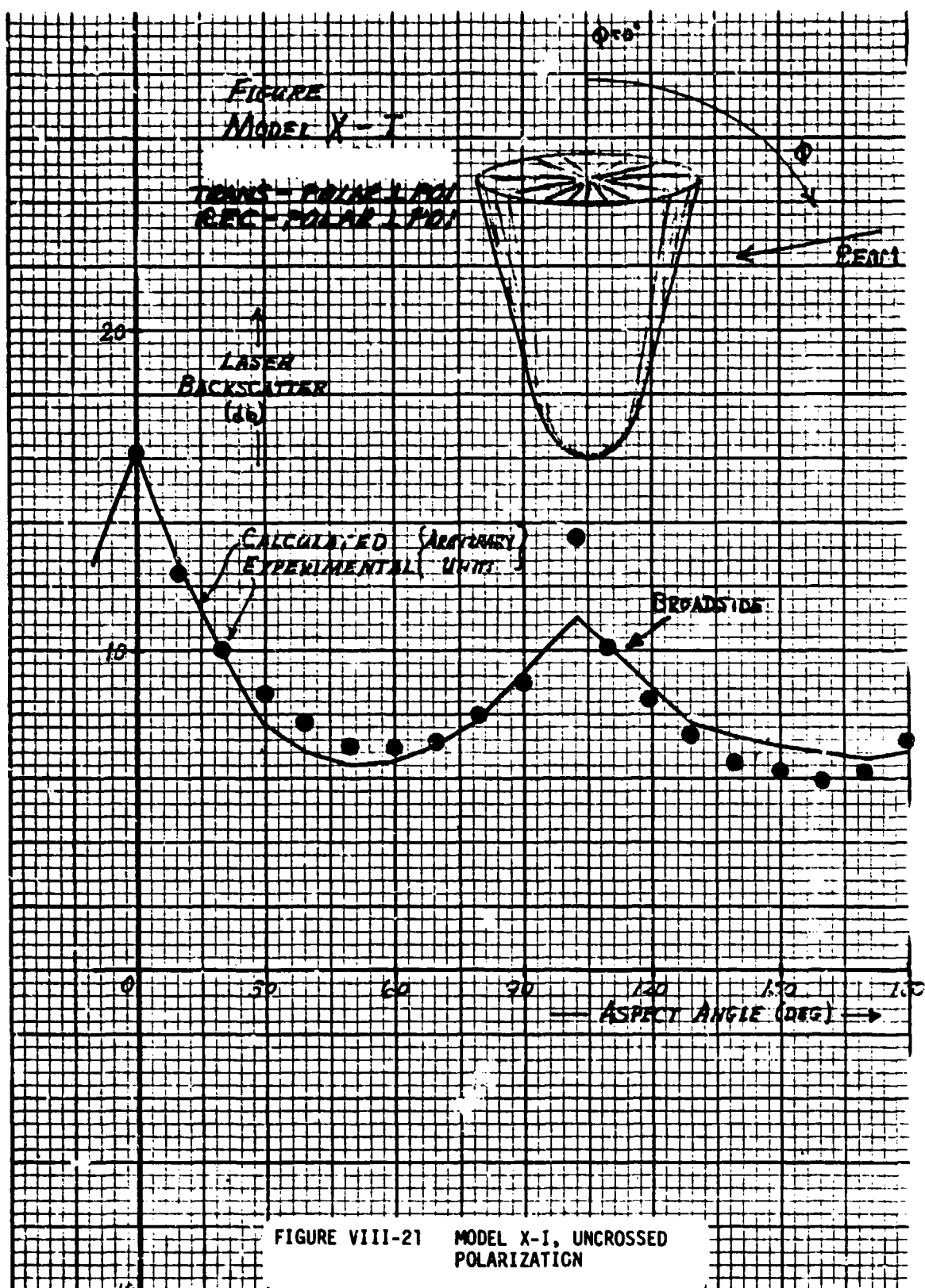
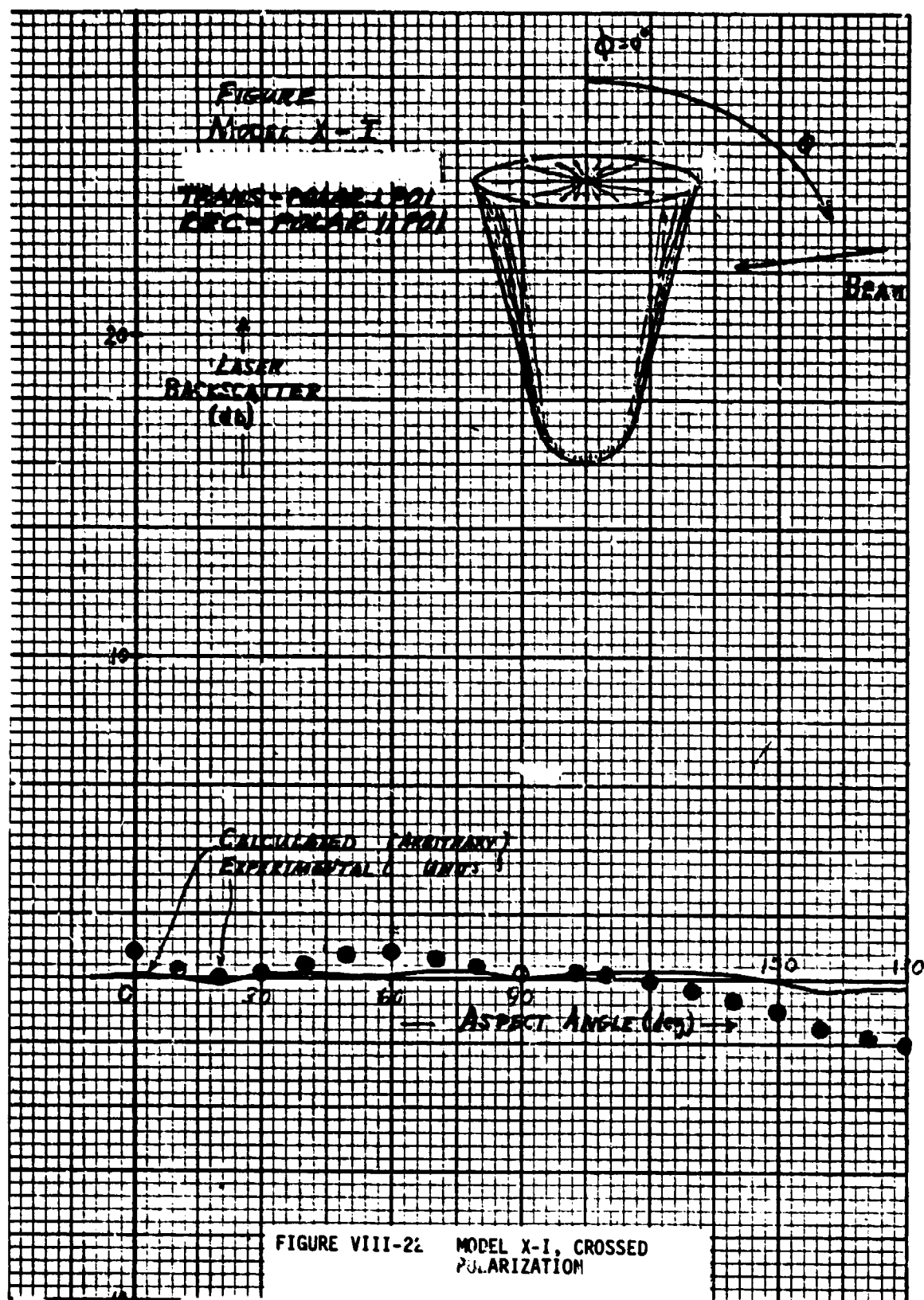


FIGURE VIII-21 MODEL X-I, UNCROSSED POLARIZATION



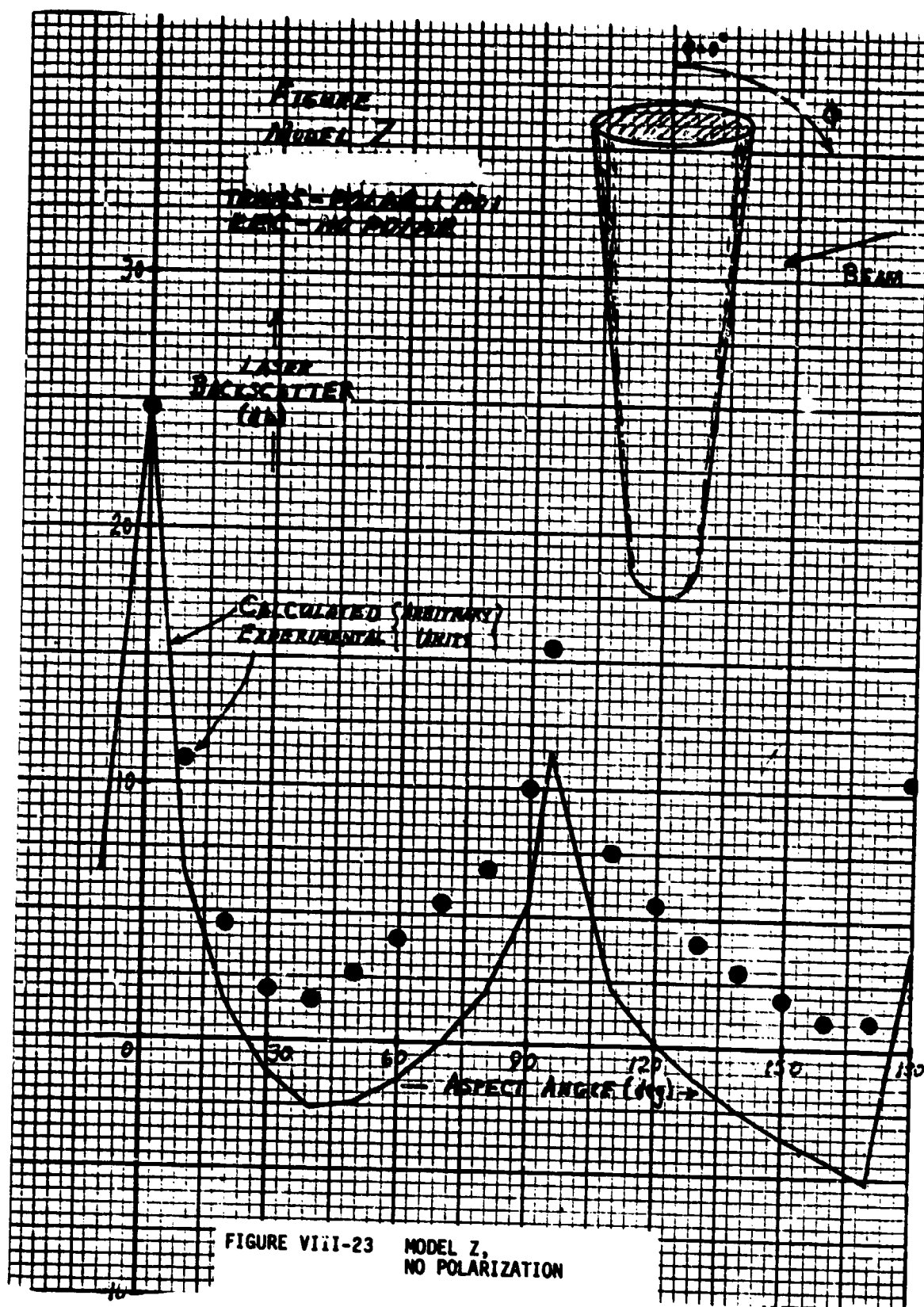


FIGURE VIII-23 MODEL Z,
NO POLARIZATION

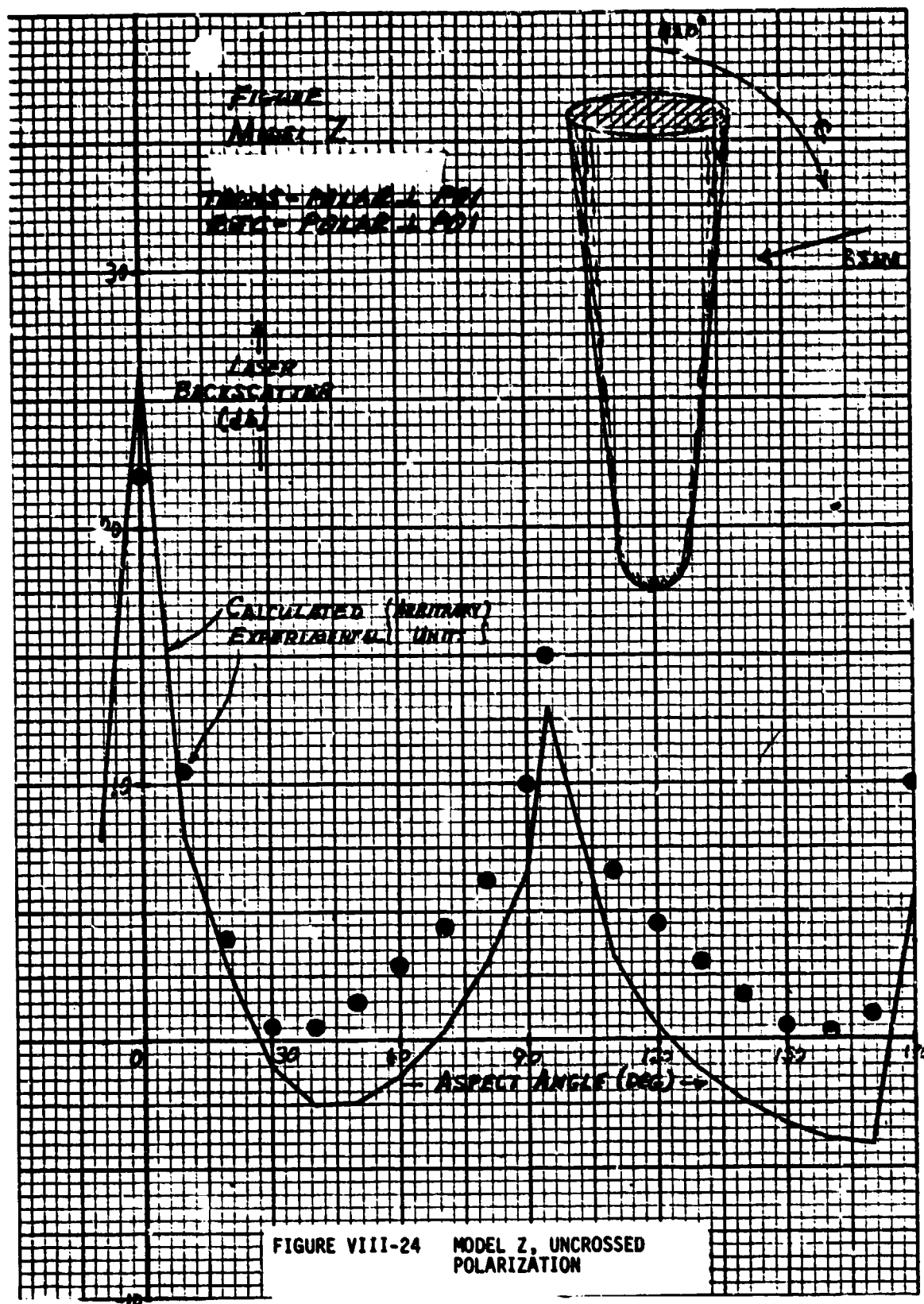


FIGURE VIII-24 **MODEL Z, UNCROSSED POLARIZATION**

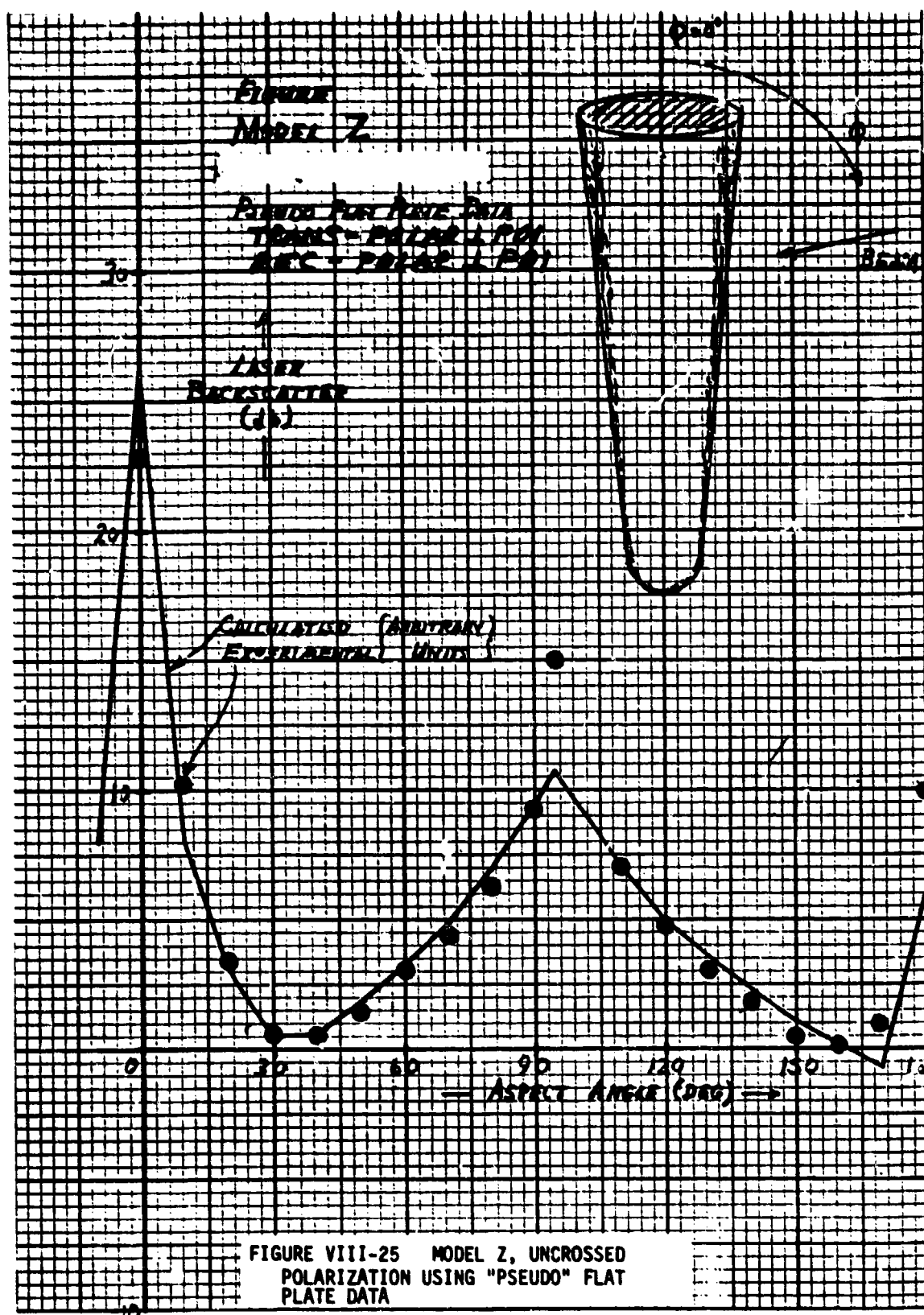
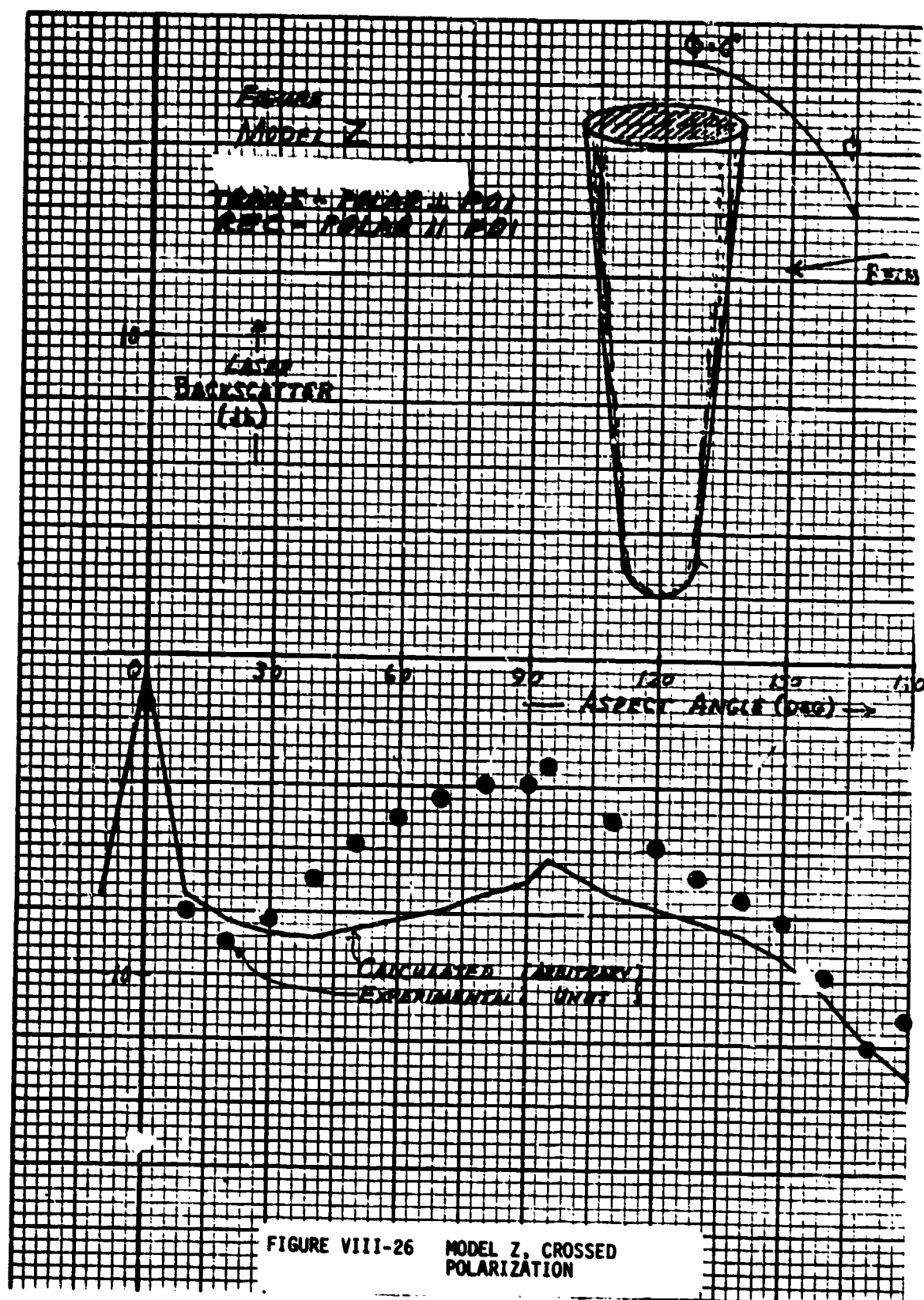
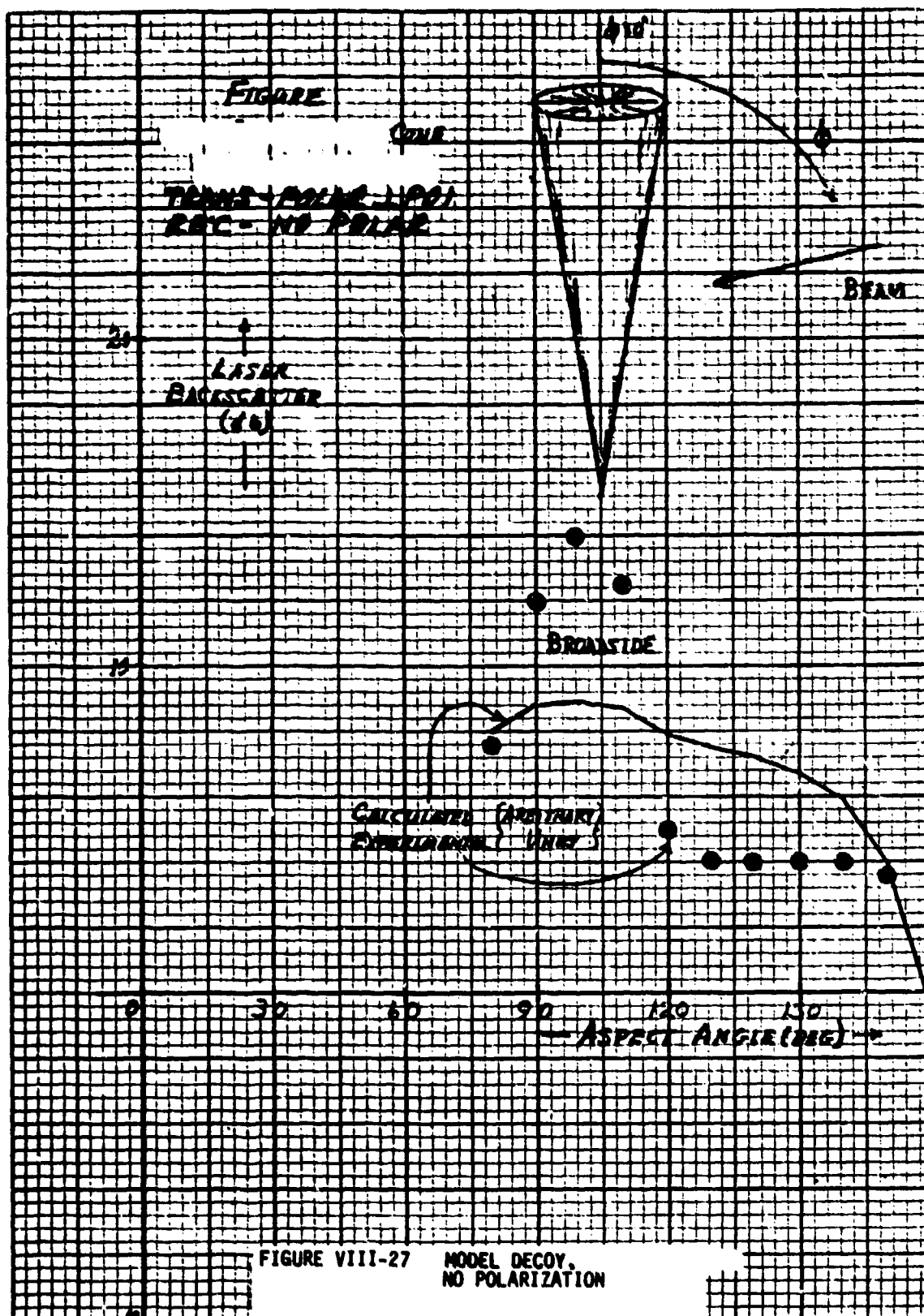
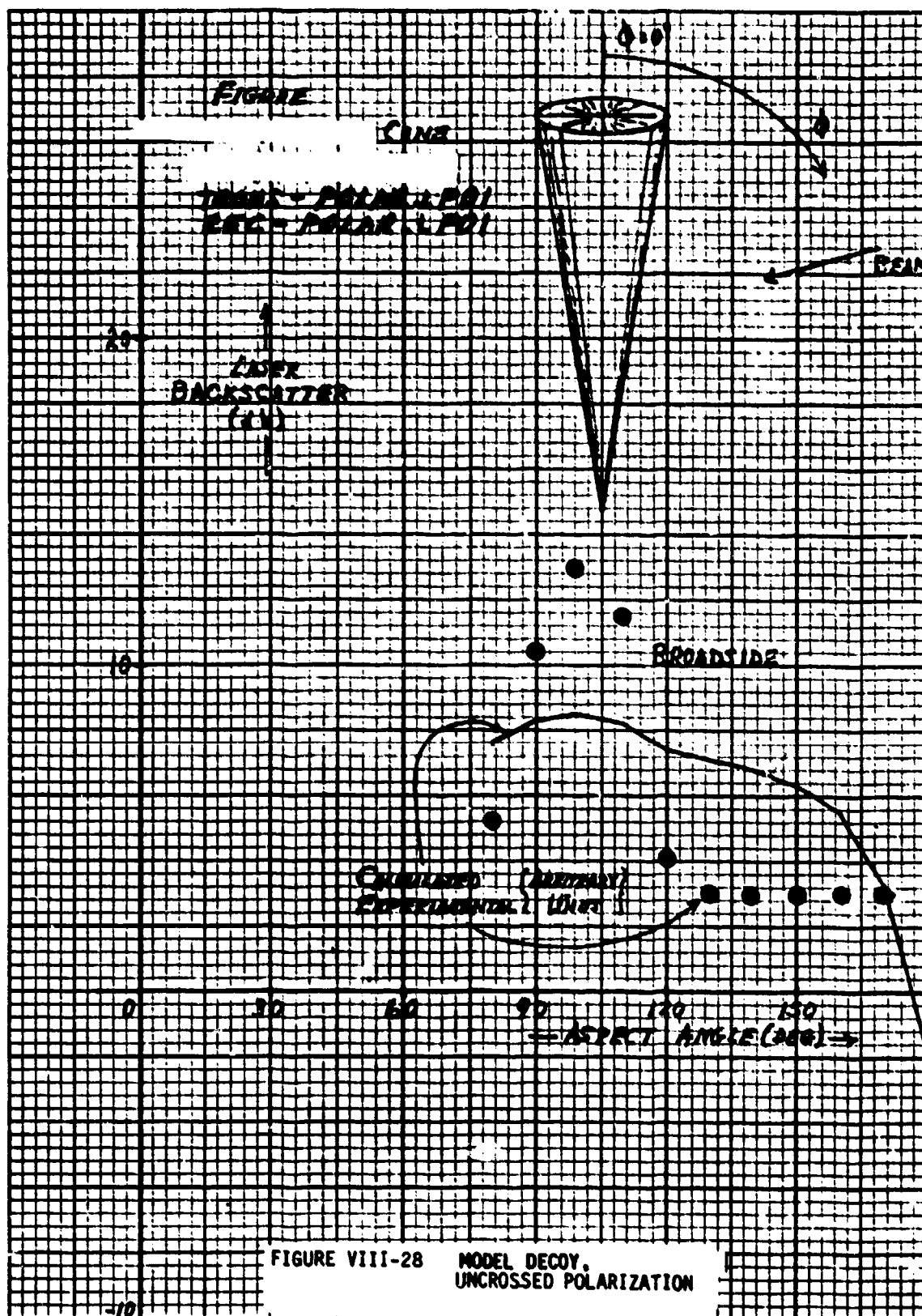
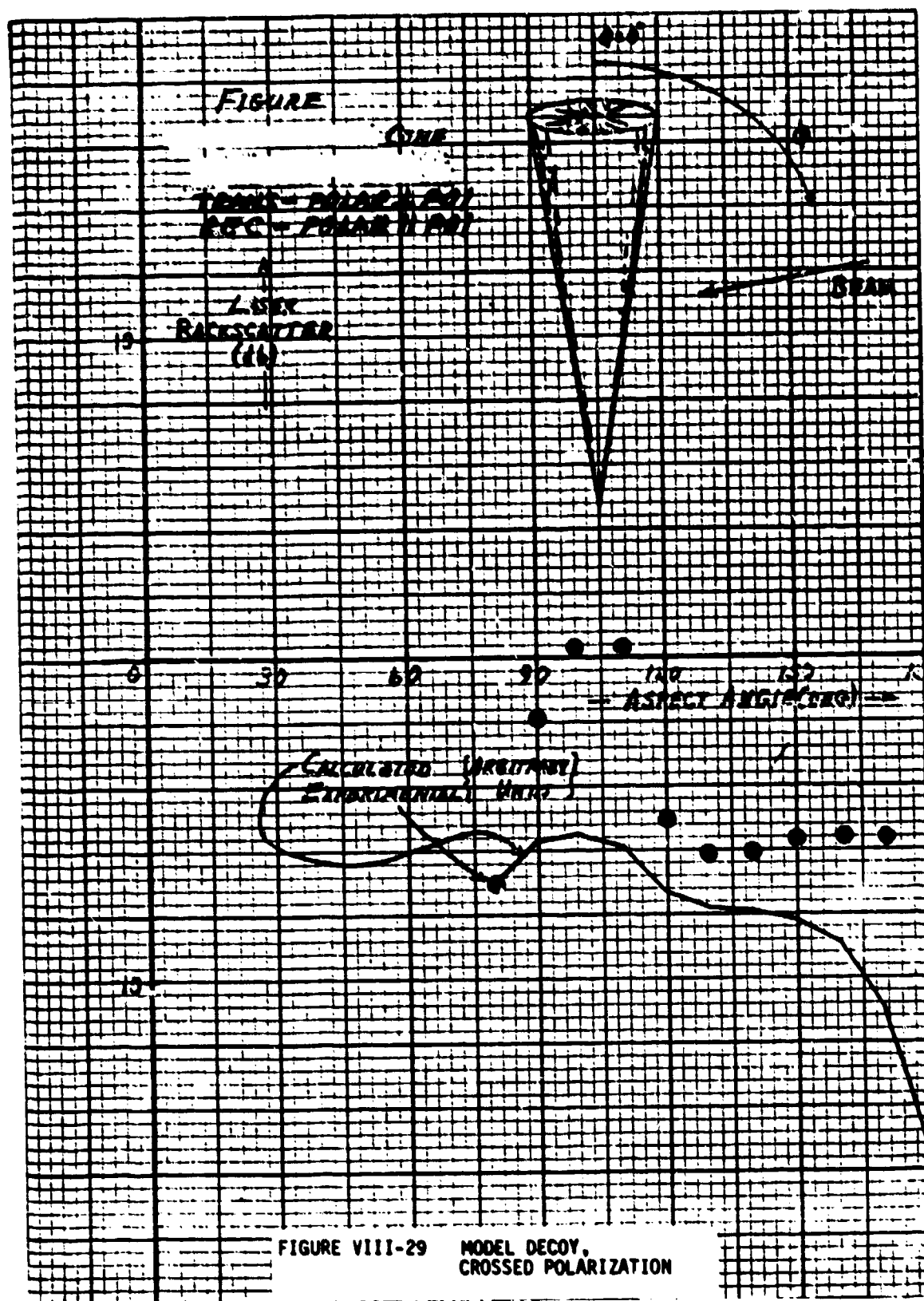


FIGURE VIII-25 MODEL Z, UNCROSSED
POLARIZATION USING "PSEUDO" FLAT
PLATE DATA









MISSION of Rome Air Development Center

RADC is the principal AFSC organization charged with planning and executing the USAF exploratory and advanced development programs for information sciences, intelligence, command, control and communications technology, products and services oriented to the needs of the USAF. Primary RADC mission areas are communications, electromagnetic guidance and control, surveillance of ground and aerospace objects, intelligence data collection and handling, information system technology, and electronic reliability, maintainability and compatibility. RADC has mission responsibility as assigned by AFSC for demonstration and acquisition of selected subsystems and systems in the intelligence, mapping, charting, command, control and communications areas.

